# Deflection of Electron Pulses by THz Fields

**Waldemar Schneider**


München 2015

# Deflection of Electron Pulses by THz Fields

**Waldemar Schneider**

Dissertation
an der Fakultät für Physik
der Ludwig–Maximilians–Universität
München

vorgelegt von
Waldemar Schneider
aus Duschanbe

München, den 08. Juni 2015

Erstgutachter: Prof. Dr. Ferenc Krausz
Zweitgutachter: Prof. Dr. Roland Kersting
Tag der mündlichen Prüfung: 21. September 2015

# Contents

# Zusammenfassung

Eine Vielzahl physikalischer und chemischer Phänomene wird durch die Dynamik von Atomen und Elektronen in Molekülen und Festkörpern bestimmt. Aus diesem Grund ist das Verständnis dieser Prozesse, folgend aus der Beobachtung der Atom- und Elektronenbewegung, ein Schlüsselelement auf dem Weg zu deren Manipulation und Kontrolle. Zeitaufgelöste ultraschnelle Elektronenbeugung bietet atomare räumliche Auflösung und ist besonders gut für diese Aufgabe geeignet. Um die relevanten, fundamentalen Bewegungen auch zeitlich aufzulösen, wird jedoch eine Elektronenpulsdauer in der Größenordnung von wenigen Femtosekunden und darunter benötigt.

Um solch kurze Pulse zu erzeugen, muss zunächst eine Methode gefunden werden, sie zu messen. Diese Dissertation berichtet über die Realisierung einer neuen Herangehensweise zu diesem Zweck. Sie basiert auf der Wechselwirkung von Elektronenpulsen und Terahertzfeldern mit einer Wechselwirkungsdauer von weniger als einer Schwingungsperiode an der Oberfläche von dünnen Metallfilmen.

Zur Erzeugung der benötigten intensiven Terahertzpulse wurde ein multi-kHz regenerativer Laserverstärker entwickelt. Das System nutzt die Scheibenlasertechnologie und nimmt damit Teil am kürzlich begonnenen Paradigmenwechsel von den oft verwendeten Titan-Saphir-Systemen hin zu Ytterbium-basierten Anlagen. Das System wurde für eine unkonventionelle Repetitionsrate zwischen 50 kHz und 300 kHz ausgelegt und bietet damit eine optimale Ausgewogenheit zwischen Pulsenergie und Durchschnittsleistung, wodurch es speziell für ultraschnelle Elektronenbeugung mit Elektronenpulsen und deren Charakterisierung zugeschnitten ist.

Intensive Terahertzpulse mit einer Dauer von einer einzigen Schwingung wurden durch optische Gleichrichtung in einem Lithium-Niobat-Kristall erzeugt. Das Verkippen der Pulsfront der generierenden Pulse ermöglicht eine optimale Konversionseffizienz. Im Vergleich zu anderen Experimenten wird sie in dieser Arbeit bei deutlich höherer Repetitionsrate ($\times 50$) erreicht.

Diese THz-Quelle wurde zum Nachweis eines Impulsaustausches zwischen dem elektromagnetischen Feld und dem Elektronenpuls an dünnen Metallfil-

men genutzt, indem die transversale Elektronenablenkung beobachtet wurde. Dieser Effekt ermöglicht die Charakterisierung der vorhandenen ($\approx 800\,\mathrm{fs}$) und der zukünftig bereitgestellten (wenige Femtosekunden) Elektronenpulse unter Verwendung des Streaking-Prinzips, welches ohne Abtasten der Zeitverzögerung funktioniert. Die Auswertung der erhaltenen Resultate und deren Vergleich mit Modellen und Simulationen offenbart die zugrundeliegenden physikalischen Phänomene.

Zum Ersten bestätigt die lineare Beziehung zwischen der Terahertz-Feldamplitude und der beobachteten Ablenkung eine direkte Elektronen-Feld-Wechselwirkung, die nicht auf ponderomotorischer Kraft basiert. Zweitens wird die relevante elektromagnetische Wechselwirkung am Metallfilm von einer propagierenden Interferenzwelle dominiert, die durch Superposition des einfallenden und des reflektierten Teils des Terahertzpulses erzeugt wird. Drittens ließ sich zeigen, dass die magnetische Feldkomponente einen bedeutenden Beitrag zum Wechselwirkungsprozess leistet, welcher abhängig von der entsprechenden Geometrie ist. Viertens resultiert die Relativbewegung zwischen der Interferenzwelle und den Elektronen in einer Wechselwirkung innerhalb der Dauer einer Schwingungsperiode. Diese Wechselwirkung stellt die physikalische Grundlage für die beobachtete feldabhängige, seitwärts gerichtete Ablenkung dar.

Nach unserem Wissen ist dieses Experiment die erste Realisierung einer von Terahertzfeldern getriebenen Streak-Kamera für frei propagierende Elektronenpulse. Die aufgrund der optischen Synchronisation fast vernachlässigbare zeitliche Fluktuation und die vollständig vernachlässigbare Ablenkungsdispersion stellen zwei bedeutende Vorteile des innovativen THz-Konzepts gegenüber der konventionellen, bei GHz-Frequenzen operierenden Technik dar. Das Streaken mit elektromagnetischen Terahertzpulsen ermöglicht die Überwindung der durch Vakuum-Durchschlagsspannung gesetzten Begrenzungen und birgt damit ein hohes Skalierungspotential.

Elektronenablenkung durch THz-Felder bietet nun die benötigte Methode zur Charakterisierung von Femtosekunden-Elektronenpulsen. Sie wird damit zur Grundlage für den Nachweis und die Erzeugung dieser Pulse und damit zu einem wichtigen Baustein für die Beobachtung von fundamentalen atomaren und elektronischen Bewegungen in Licht-Materie-Wechselwirkungen.

# Abstract

Electron dynamics in atoms, molecules and solids determine a vast range of physical and chemical phenomena. The observation and understanding of electron motion on the atomic scale is therefore a key element towards manipulation and control of these processes. Time-resolved ultrafast electron diffraction provides atomic-scale spatial resolution and is therefore an excellent method for this task. However, electron pulse durations on the order of few femtoseconds or below are required to resolve the relevant fundamental motions in time.

Before such pulses can be generated, a method has to be found for their temporal characterization. This thesis reports a novel approach and its realization. The method is based on sub-cycle interaction of electron pulses with THz electric fields in vicinity of a thin metal-film. For generating the necessary intense THz pulses, a regenerative multi-kHz laser amplifier system has been devised and implemented. The system uses the thin-disk technology and thus participates towards the recently initiated paradigm change from widely used titanium-sapphire setups towards ytterbium based devices. Design for an unconventional repetition rate between 50 kHz and 300 kHz provides an optimal balance between pulse energy and average power, making the system especially suitable for ultrafast electron diffraction with single-electron pulses and their characterization.

Intense, single-cycle THz pulses were generated by optical rectification in a lithium niobate crystal. Tilting the front of the driving pulse was used to achieve state-of-the-art conversion efficiency, but at significantly higher ($\times 50$) repetition rates.

This THz source was used to demonstrate the momentum exchange between the electromagnetic field and the electron pulse at a thin metal-film by observing the transversal electron deflection. The effect allows for the streaking characterization of currently available ($\approx 800$ fs) and future (few-femtosecond) electron pulses without scanning a time delay. The analysis of the obtained results and comparison to models and simulations reveal the underlying physical mechanisms: Firstly, the linear relation between the THz

field amplitude and the observed deflection confirms a direct electron-field interaction, not of ponderomotive type. Secondly, the relevant electromagnetic interaction at the film is found to be dominated by a propagating interference wave which originates from the superposition of incident and reflected parts of the single-cycle THz pulse. Proper choice of the involved angles provides velocity matching for extended laser and electron beams. Thirdly, the magnetic field components were discovered to have significant contributions in the interaction process, depending on the geometry angles. Fourthly, the relative motion between the interference wave and the electron results in a sub-cycle interaction, providing the physical basis for the observed field-dependent sideways deflection.

To our knowledge, this experiment represents the first realization of a THz-driven streak camera for freely propagating electron pulses. The almost negligible timing jitter due to the all-optical synchronization and the fully negligible deflection dispersion constitute two significant advantages of the innovative THz concept over conventional devices operated at GHz frequencies. Streaking with electromagnetic THz pulses allows to overcome the electrical breakthrough limit and thus offers high scalability potential.

In summary, electron deflection by THz fields provides the required method for characterization of few-femtosecond electron pulses and will enable their realization, in order to observe the fundamental atomic and electronic motions in light-matter interaction.

# List of Figures

# List of Publications


[1] A. Ozawa, A. Vernaleken, W. Schneider, I. Gotlibovych, Th. Udem, and Th. W. Hänsch. "Non-collinear high harmonic generation: a promising outcoupling method for cavity-assisted XUV generation." *Optics express*, vol. 16 (9), pp. 6233–6239, 2008.

[2] A. Ozawa, W. Schneider, Th. W. Hänsch, Th. Udem, and P. Hommelhoff. "Phase-stable single-pass cryogenic amplifier for high repetition rate few-cycle laser pulses." *New Journal of Physics*, vol. 11 (8), p. 083029, Aug. 2009.

[3] A. Ozawa, W. Schneider, F. Najafi, Th. W. Hänsch, Th. Udem, and P. Hommelhoff. "A Peltier cooled single pass amplifier for Titanium:Sapphire laser pulses." *Laser Physics*, vol. 20 (5), pp. 967–970, 2010.

[4] A. Vernaleken et al. "Single-pass high-harmonic generation at 20.8 MHz repetition rate." *Optics Letters*, vol. 36 (17), pp. 3428–3430, 2011.

[5] W. Schneider, A. Ryabov, Cs. Lombosi, T. Metzger, Zs. Major, J. A. Fülöp, and P. Baum. "800-fs, 330-µJ pulses from a 100-W regenerative Yb:YAG thin-disk amplifier at 300 kHz and THz generation in $LiNbO_3$." *Optics Letters*, vol. 39 (23), p. 6604, Dec. 2014.

[6] F. Habel, W. Schneider, F. Krausz, and V. Pervak. "Broadband thin-film polarizer for ultrafast lasers." *to be published*, vol.,

[7] W. Schneider, C. Kealhofer, A. Ryabov, D. Ehberger, F. Krausz, and P. Baum. "THz control of electron pulses." *to be published*, vol.,

# Chapter 1

# Introduction

At the first emergence of cathode rays [1], discovered by J. W. Hittorf in 1869, no one was imagining their extraordinary impact in science and technology up to day. In 1897, J. J. Thomson showed the particle-like character of the cathode rays and estimated the mass of the constituents to be three orders of magnitude lighter than that of a hydrogen atom [2], thereby having discovered the first subatomic particle, the electron.

Invented by K. F. Braun in 1897, the cathode-ray tube [3] became the core component in oscilloscopes and screen technologies for about a century. Closely connected to cathode-ray tubes are the triode and the X-ray tube. The triode was invented by Lee De Forest in 1906 [4]. Enabling the amplification of electronic signals for the first time, it created the foundation of electronics until its replacement by the transistor in the 1960s. The X-ray tubes [5, 6] opened up the field of radiography, where they are used up to the present days.

Free electron beams are also routinely employed in material science, e.g. in electron diffraction, electron microscopes, electron lithography, electron beam melting and electron-beam induced deposition. They are used at linacs and synchrotrons, directly and in combination with free electron lasers, to generate electromagnetic radiation spanning from the THz range up to x-ray radiation [7–9].

## 1.1 Overview

Owing to the picometer-scale de Broglie wavelength, electron microscopy and diffraction methods offer subatomic spatial resolutions, which have enabled an ever deeper insight into the atomic structure of crystals, molecules and even proteins [10–14]. However the methods provide only static information

about the final state of a studied sample. Motivated by the envisioned control of chemical reactions with laser light, observing the atomic motion as it evolves during molecular rearrangements and condensed matter transitions became of central interest [15–17]. Resolving atomic motion requires not only sub-atomic spatial but also femtosecond temporal resolution [18, 19].

These time resolutions are readily achievable in all-optical pump-probe setups, since the advent of femtosecond laser sources [20–22]. In this approach, the dynamic process of interest is excited by a pump-pulse, which is significantly shorter than the investigated dynamics, and subsequently sampled with the probe pulse, which must be short enough to capture an instant of motion. Recording the signal at different delays results in the characterization of the entire dynamic process. With the creation of isolated attosecond pulses, the temporal resolution was extended even into the regime of electronic motion [23]. This milestone in the field of time-resolved spectroscopy greatly expanded the knowledge of ultrafast electronic processes in atoms, molecules and condensed matter [24–34].

Concepts like ultrafast electron microscopy and ultrafast electron diffraction [35, 36] combine atomic-scale imaging with the pump-probe approach. Provided an electron pulse duration on the order of tens femtoseconds or below, these methods offer sub-atomic spatial and femtosecond temporal resolution at the same time.

However, achieving the required electron pulse durations is not trivial. The electron charge causes repelling Coulomb forces between the particles, which broaden a multi-electron pulse [37]. Furthermore, the electron rest mass is responsible for an energy-dependent propagation velocity of the particles in vacuum, which causes pulse broadening as it travels to the sample. While space charge forces can be avoided in single-electron pulses [18], the dispersion compensation demands elaborate measures. Typically, pulse compression is achieved in actively controlled microwave cavities by accelerating slower and decelerating faster electrons with electric fields [38–40]. An alternative or complimentary approach could result from recently observed THz-assisted spectral narrowing of electron pulses generated by nanotip photoemission [41].

Compression of electron pulses requires a reliable method of their characterization. A standard approach is implemented in the conventional streak camera, where an electron pulse enters and transverses a volume with controlled, time-dependent electric field oriented transversally or longitudinally to the electron propagation direction. The transient electric field causes a time-dependent transversal or longitudinal momentum transfer to the propagating electrons and thus maps temporal information into spatial or energy domain. Streak cameras utilizing synchronized microwave-cavities or based

on laser-triggered deflection have been realized, still their temporal resolution is limited by achievable magnitude of the field gradient as well as by the pulse-to-pulse jitter and do not achieve values below 150 fs. A recently suggested THz-driven split ring resonator [42] constitutes a promising approach to overcome this limit.

In another approach, electron pulses are spatially as well as temporally overlapped with intense laser pulses, such that the ponderomotive force can be used to deflect the electrons towards regions of lower optical intensity [43, 44]. By implementing a standing wave configuration of this method, the required laser pulse energy has been reduced from mJ to µJ levels [45, 46]. The signal obtained in both cases can be interpreted as a cross-correlation between the electron pulse and laser's intensity envelope, so that the ultimate temporal resolution of this concept is limited by the duration of optical pulse and velocity mismatch in the overlap region.

Recently, a different approach was demonstrated in our group [47]. In this concept, 25 keV free electron pulses were longitudinally accelerated and decelerated within a near infra-red, optical field oscillating at a thin metal-foil. The method is employable with nJ optical pulse energies and allows to determine the duration of the electron pulses that are shorter than half the optical cycle or approximately as long as the optical pulse or longer. Measuring pulse durations in between is impossible. Furthermore the concept makes use of an energy analyzer that is not readily available for electron energies approaching the relativistic regime.

Related is photo-induced near-field electron microscopy (PINEM) [48, 49]. Here, evanescent near-fields at a nano-structure are excited by an optical pulse and mediate quantized energy transfer to the probing electron pulse. The electron-photon interaction can be imaged on the femtosecond timescale, which facilitates the retrieval of the electron's pulse duration. As in previous concept, this method requires an elaborated detection scheme (electron microscope).

## 1.2 Motivation and Scope of This Work

All available methods for fs electron pulse characterization are either limited in resolution (streak camera), restricted to high optical pulse intensities (ponderomotive force), are not applicable in an important range (optical streaking), or require an sophisticated detection method (optical streaking and PINEM). Therefore the goal of presented work is to investigate a novel pulse characterization concept, which allows to overcome these obstacles and thus offers the scalability for characterization of few-femtosecond electron

pulses.

The method is based on two central innovations (see figure 1.1). Firstly, the concept utilizes a thin metal foil to transfer momentum from a laser-generated electromagnetic field to the traversing electron pulses, as it happens in optical streaking. But instead of detecting the longitudinal acceleration/deceleration of electrons with a time-of-flight spectrometer, their transversal deflection is recorded on a screen. This combination of optical streaking method with conventional streak camera allows to circumvent the need of a complicated detector, and simultaneously to exceed the streaking fields typically obtained in conventional streak cameras. Secondly, the streaking field's spectral range is shifted into the THz domain. The increase in wavelength by three orders of magnitude as compared to near-infrared wavelength [47] allows to streak femtosecond electron pulses within the sub-cycle regime.

This project, initiated in February 2012, started with the customization of the laboratory for high average-power laser applications. The essential experimental parts include the laser source, the vacuum setup, the electron generation setup, the THz generation setup and the electron deflection setup. Figure 1.1 gives a first overview of the experimental scheme for THz driven streaking of free electron pulses. A high-repetition-rate regenerative amplifier, described in chapter 2, provides near infrared, picosecond pulses. Most of the output power is used for generation of THz-pulses by optical rectification in a doped lithium niobate crystal ($LiNbO_3$), described in chapter 3. A small fraction of the power is split to generate second-harmonic pulses and subsequently the free electron pulses in a photoemission process. This task, as well as the control of electron pulses, is described in detail in the thesis of Daniel Kreier [50], appendix A of present thesis summarizes the most important results. Chapter 4 describes the concept of the electron deflection by THz-fields, whereas in chapter 5 the experimental implementation, the obtained results and their discussion is presented.

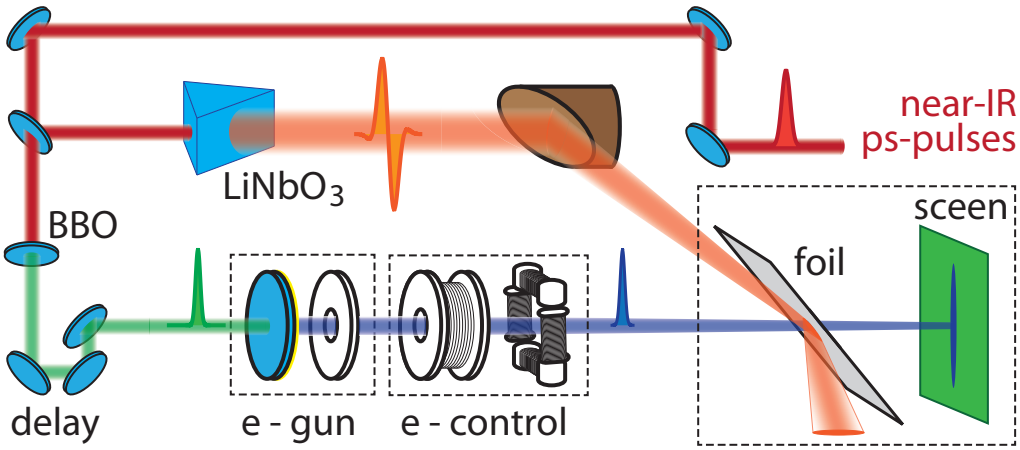


Figure 1.1: First overview of the THz-driven electron deflection setup. Near-infrared optical pulses are mainly used for the generation of THz-pulses by optical rectification. A small fraction is split to generate second harmonic pulses, which subsequently produce free electron pulses. A solenoid and coils focus and steer the electron beam onto the screen. The THz-pulses are tightly focused on a thin metal-foil. Spatial and temporal overlap of THz- and electron-pulses enables the deflection of the free electrons, which is registered on a screen.

# Chapter 2

# High-Repetition-Rate Femtosecond Laser Amplifier

Realizing an experiment on deflecting of few-electron pulses by THz fields implies two contrary specifications on the laser source. On the one hand, few-electron pulses generate low signal amplitudes and require relatively high repetition rates of at least tens to hundreds of kHz to restrict acquisition times to reasonable durations. On the other hand, efficient THz generation by optical rectification demands pump pulse energies on the scale of few hundred microjoules. To meet these conditions, a high repetition rate, high-power laser amplifier was build within this work [51]. The system was derived from a preliminary device [52].

## 2.1 Modifications on Laboratory Infrastructure

The combination of pulse repetition rates of hundreds of kHz with microjoule pulse energies implies average output powers on the order of hundred watts. Such uncommonly high average powers impose special requirements on the laboratory infrastructure. Modifications improving the cleanliness of ambient air, as well as concerning the laser safety were made in this work. Figure 2.1 shows the home-build clean-room cell equipped with four flow-boxes (ap-systems GmbH) to reach clean-room class ISO 5, according to the norm ISO 14644-1. High-power laser curtains (Kentek Corp., EVER-GUARD) were installed, to separate the laboratory into two subspaces, one for the laser and one for the electron beam line.

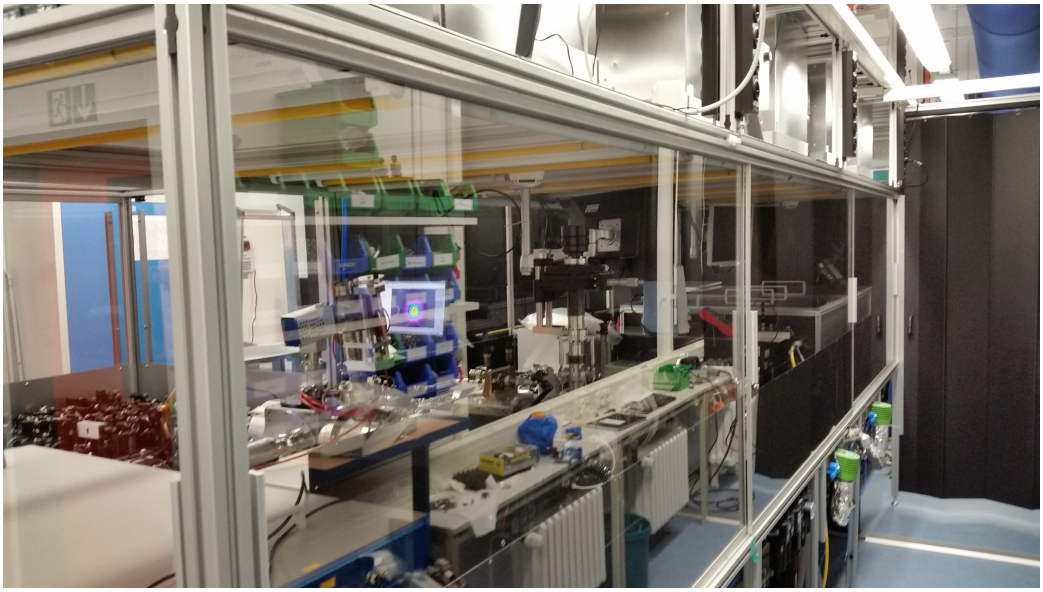

Figure 2.1: Additionally installed infrastructure for high power laser applications: clean-room cell, flow-boxes and metal laser protection curtains.

## 2.2 High-Repetition-Rate Yb:YAG Amplifier

*Here the laser system is described; this chapter is a reprint of my publication "800-fs, 330-µJ pulses from a 100-W regenerative Yb:YAG thin-disk amplifier at 300 kHz and THz generation in $LiNbO_3$" in Optics Letters, 2014 [51]. The original work is attached in appendix B.*

Yb:YAG thin-disk lasers offer extraordinary output power, but systems delivering femtosecond pulses at a repetition rate of hundreds of kHz are scarce, even though this regime is ideal for ultrafast electron diffraction, coincidence imaging, attosecond science and THz spectroscopy. Here we describe a regenerative Yb:YAG amplifier based on thin-disk technology, producing 800-fs pulses at a repetition rate adjustable between 50 and 400 kHz. The key design elements are a short regenerative cavity and fast-switching Pockels cell. The average output power is 130 W before the compressor and 100 W after compression, which at 300 kHz corresponds to pulse energies of 430 µJ and 330 µJ, respectively. This is sufficient for a wide range of nonlinear conversions and broadening/compression schemes. As a first application, we use optical rectification in $LiNbO_3$ to produce 30-nJ single-cycle THz pulses with 6 W pump power. The electric field exceeds 10 kV/cm at a central frequency of 0.3 THz, suitable for driving structural dynamics or controlling electron

beams.

Femtosecond lasers are indispensable in many fields of science and technology. While Ti:sapphire-based sources typically produce the shortest pulses, there is a recent paradigm shift to Yb:YAG technology [53], offering significantly higher output power and scalability, especially in geometries with thin-disks, slabs or fibers. Reported Yb:YAG-based lasers producing femtosecond pulses ($< 1$ ps) can be sorted into mode-locked oscillators [54, 55], fiber lasers [56, 57], long-cavity oscillators [58–60], slab amplifiers [61, 62], disk amplifiers [63, 64], or cascaded laser chains for pulses in the multi-mJ regime [65–70].

Many applications require repetition rates between 100 kHz and 1 MHz. This intermediate regime between oscillators and conventional amplifiers is unusual, but beneficial in pump-probe spectroscopy, material processing, attosecond science or coincidence imaging, for improving the signal-to-noise ratio, enhancing the total flux or reducing acquisition times. Our particular case is ultrafast electron diffraction with single-electron pulses [18, 36] for probing structural dynamics with atomic resolution in space and time [19]. An optimum repetition rate is 200-300 kHz [71]; yet the laser pulses should be powerful enough (hundreds of µJ) for effective nonlinear optical frequency conversions to the ultraviolet/visible/infrared [72, 73] and THz domains [74, 75], in order to initiate and control atomic-scale dynamics.

None of the Yb:YAG-based laser systems demonstrated so far (fiber, slab, crystal, disk) [53], provide sufficiently intense and stable femtosecond pulses at hundreds of kHz for these diffraction applications, which require maximum simplicity of the laser system. Hence, we describe here the design and operation of a regenerative Yb:YAG amplifier based on thin-disk technology, producing 800-fs pulses at an adjustable repetition rate between 50 and 400 kHz.

Figure 2.2 depicts the experiment, based on a preliminary attempt [52]. The seed (t-Pulse 50, Amplitude Systèmes) is a mode-locked Yb:YAG oscillator with a repetition rate of 50 MHz at a central wavelength of 1030 nm, delivering fs pulses with an energy of $\sim 40$ nJ and a spectral bandwidth of 2.7 nm. These pulses propagate through transmission gratings with 1400 lines per mm and f = 1 m lenses, producing a group-velocity dispersion of 27 ps$^2$ and $\sim$ 160-ps pulses for chirped-pulse amplification.

The desired high repetition rate in the multi-hundred-kHz regime together with the thin-disk's limited gain per reflection of $\sim 10\%$ puts some significant constraints on the regenerative cavity. Each amplified pulse must leave the cavity before the next seed pulse can enter. For a design at $\nu_{\mathrm{rep}} = 400$ kHz and 10% gain, we estimate that $N_{\mathrm{gain}} \approx 200$ round trips are required. Hence the maximum cavity length is $c/(2\nu_{\mathrm{rep}}N_{\mathrm{gain}}) \approx 1.9$ m and the switching time for

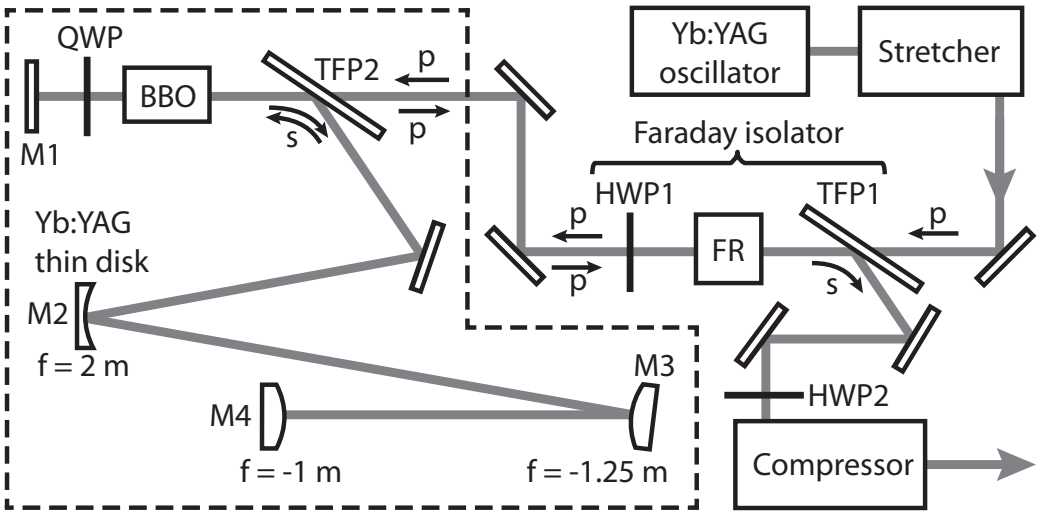


Figure 2.2: Experimental setup and optical layout of the regenerative amplifier. TFP, thin-film polarizer; FR, Faraday rotator; HWP, half-wave plate; BBO, Pockels cell; QWP, quarter-wave plate; M1-M4, dielectric mirrors. The regenerative amplifier cavity is marked with a dashed line. Arrows denote the polarization state.

coupling the pulses in and out must be shorter than $1/(\nu_{\mathrm{rep}} N_{\mathrm{gain}}) \approx 12\,\mathrm{ns}$. This necessitates a small Pockels cell crystal to minimize the high-voltage required for switching. In turn, the cavity mode must be designed small enough to avoid clipping and damage, but also large enough to minimize B-integral accumulation.

Our design is depicted in Fig. 2.2 within the dashed outline. The disk module (TRUMPF) employs a $\sim$ 1/10 mm thick, $\sim$ 10%-doped Yb:YAG thin-disk on a water-cooled heat sink, pumped by laser diodes at $\sim$ 940 nm (LDM 500, Laserline GmbH). The disk has a radius of curvature of $r \approx 2\,\mathrm{m}$ (M2). In order to comply with the considerations above, we use two convex mirrors (M3, M4) and a total cavity length of 1670 mm. The cavity's stability is calculated using ray transfer matrices (see Fig. 2.2). The beam diameter in the Pockels cell is $< 1.5\,\mathrm{mm}$ (full-width at half maximum) and the accumulated B-integral is $\sim 0.05$. The Pockels cell is an anti-reflection-coated BBO crystal with a size of $6 \times 6 \times 25\,\mathrm{mm}^3$, driven with a rise time of $\sim 6\,\mathrm{ns}$ by a pulsed high-voltage supply (Bergmann KG). Hence we conform to all considerations outlined above.

A mode-matching telescope is to couple in the seed pulses with a typical switching sequence [76]: A thin-film polarizer (TFP-1), Faraday rotator

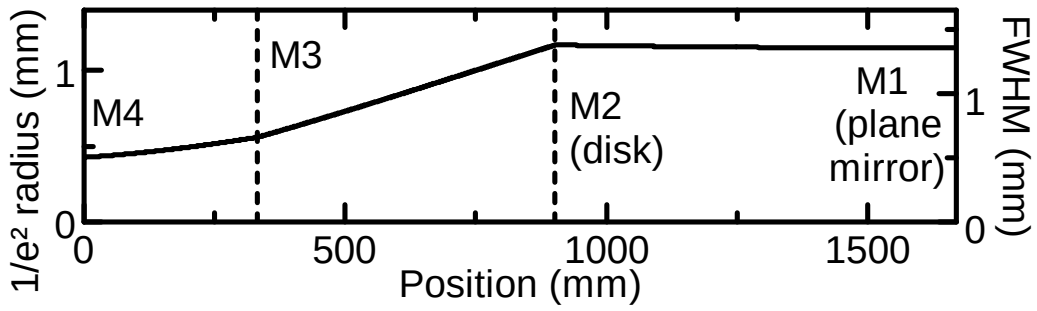


Figure 2.3: Design of the length-limited amplifier cavity (dashed area in figure 2.2) for operation at high repetition rates up to 400 kHz. Solid, beam diameter along the cavity mode; dashed, position of mirrors M2 and M3. FWHM, full width at half maximum.

(FR) and half-wave plate (HWP) form an isolator. P-polarized incoming pulses enter the amplifier cavity through a thin-film polarizer (TFP-2). The Pockels cell (BBO) is in its "off" switching state and a double-pass through a quarter-wave plate (QWP) produces back-propagating pulses with spolarization, which are reflected by TPF-2. Before their return from mirror M4, the Pockels cell is switched "on", rotating polarization by 45 deg and rendering the QWP ineffective. S-polarized pulses are therefore captured in the amplifier cavity until the Pockels cell is switched "off" again. The QWP produces p-polarization and the pulses leave the cavity through TFP-2. The Faraday isolator directs them towards compression and applications.

In the following, we applied 120 round trips at 300 kHz before coupling the final pulse out of the amplifier cavity. More round trips could destroy the Pockels cell, as described in more detail below. Figure 2.2(a) shows the increase of output power with increasing pump power. Ellipticity, observed after the end mirror M1, increases slightly from 0.95 at low power up to 0.8 at above 100 W of output. Nevertheless, the cavity is always stable. At 370 W of pump power, we achieve an output power of 130 W before the compressor. This corresponds to a pulse energy of 430 µJ. Figures 2.2(b-c) show the beam profiles at 130 W measured after the focus and in the focus of an $f = 450$ mm lens, respectively. The measured M2 value at an output of 130 W is 1.30 and 1.35 for the horizontal and the vertical directions, respectively.

Compression of the 130-W output pulses is achieved using two reflective gratings with 1400 lines per mm at a separation of 1.76 m; the angle of incidence is 47 deg. The throughput of this compressor amounts to 77%; $\sim$ 100 W are emitted for applications. Figure 2.2 shows the spectrum and

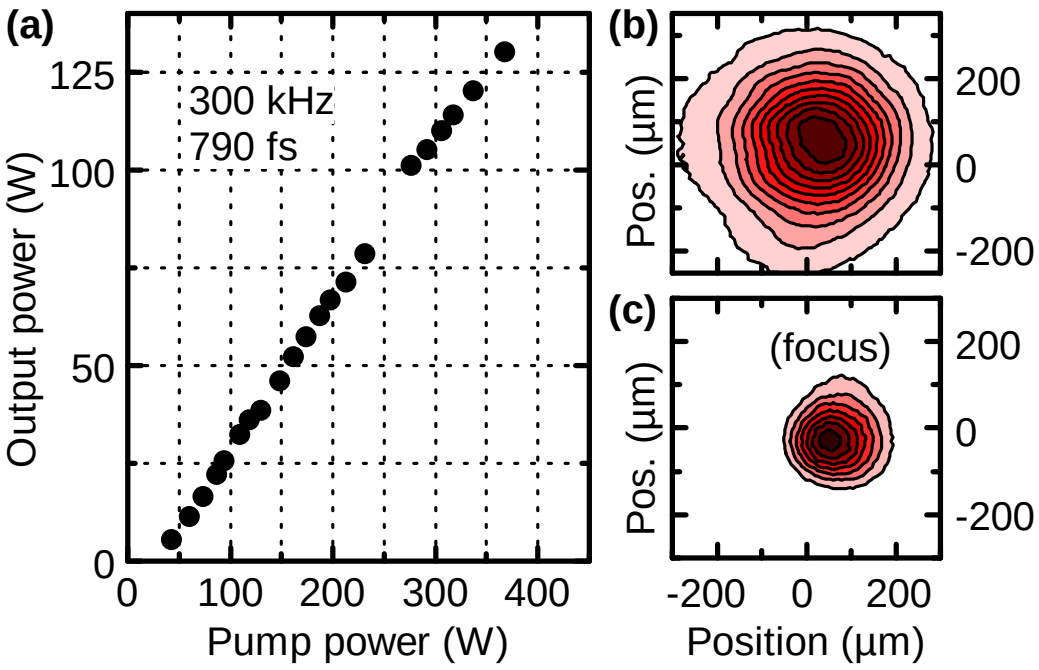


Figure 2.4: Output performance. (a) Output power in dependence of the pump power. (b) Beam profile after a focus. (c) Shape of a focused spot. Intensity of the beam profiles is normalized.

autocorrelation trace (pulseCheck, APE GmbH). With respect to the seed spectrum with a width of 2.7 nm, the amplified spectrum shows signs of gain narrowing and a width of 2.3 nm. Still, the Fourier limit calculated from the measured spectrum is 740 fs. There is no evidence for self-phase modulation or any other nonlinear processes; the slight wiggles are interferences at the spectrometer's fiber entrance. The autocorrelation trace indicates compressed pulses of 790 fs duration, assuming a $\mathrm{sech}^2$ shape. This is within 7% of the Fourier limit and indicates a good match between stretcher, intracavity dispersion and compressor in our system. Higher-order chirp, as can occur from self-phase modulation, is negligible.

The output power is stable to about 1% rms on the subminute time scale. On longer time scales, there are some systematic oscillations of $\pm 2\%$ (peak-to-peak) caused by the disk's chiller system, which is currently only stable to $\pm 1$ K. The laser reliably runs over several days without alignment; no significant drifts of output power are observable ($< 0.8\%$ over a day, $< 0.05\%$ per hour).

We note in Fig. 2.2(a) the almost linear relation; we do not reach satu-

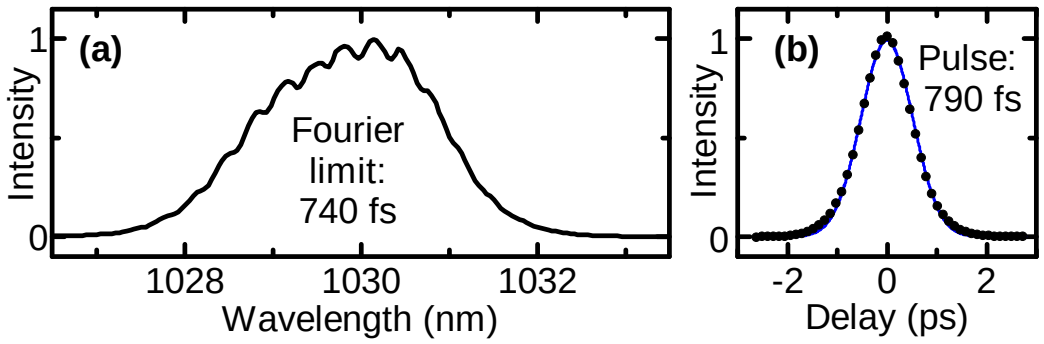


Figure 2.5: Regenerative amplifier performance in the time-bandwidth domain. (a) Output spectrum. (b) Autocorrelation trace (black dots), fitted assuming a $\mathrm{sech}^2$-shaped temporal pulse profile (blue line). The pulse duration (790 fs) is close to the measured spectrum's Fourier limit (740 fs).

ration. This suggests that we could further increase the pump power or the number of round trips and achieve even higher output and stability. In practice, however, this is limited by Pockels cell damage, occurring either at the front or back surface as an extended dark region around the center, where the beam passes through. We attribute this damage to the effects of average intracavity power in conjunction with coating imperfections. One solution would be to obtain better-coated crystals, which is technologically challenging. An alternative would be to redesign the cavity for a slightly larger mode at the Pockels cell crystal, accepting some minor clipping. There is also room for moderate lengthening of the cavity, especially if more intense seed pulses are applied at a reduced number of round trips. In view of these options, and potentially others, it might be possible to further scale our 300-kHz regenerative disk amplifier concept towards higher output powers, in case this should be desirable.

## 2.3 Beam Stabilization System

As explained in section 2.1, the laboratory's experimental area is separated from the laser source by a distance of approximately 10 m. When bridging this distance, the beam passes several, possibly drifting, optical components and is exposed to fluctuations of ambient air. The disturbances result in significant beam pointing fluctuations at the experimental area. To compensate these effects, an active beam stabilization system (Aligna 4d BeamLock, TEM Messtechnik GmbH) has been integrated into the optical setup. The

device monitors position and direction of the optical beam by two position-sensitive detectors and compensates the deviations from the set point with two motorized mirror mounts equipped with piezo actuators.

Figure 2.6 (a) depicts the performance of the beam pointing stabilization system, indicating an improvement in angular spread by a factor of 10 when the stabilization system is deployed. Figure 2.6 (b) shows the transversal beam mode at the experimental area, indicating a beam size of 2 mm (full width of half maximum) and a mode ellipticity of about 0.9. Both measurements were taken with a beam profiler (WinCamD, UCD12-1/2") located approximately 10 m from the amplifier's cavity thin-film polarizer.

As a concluding remark, one can state that this laser system meets the conditions for THz generation, generation of femtosecond electron pulses and other future applications.

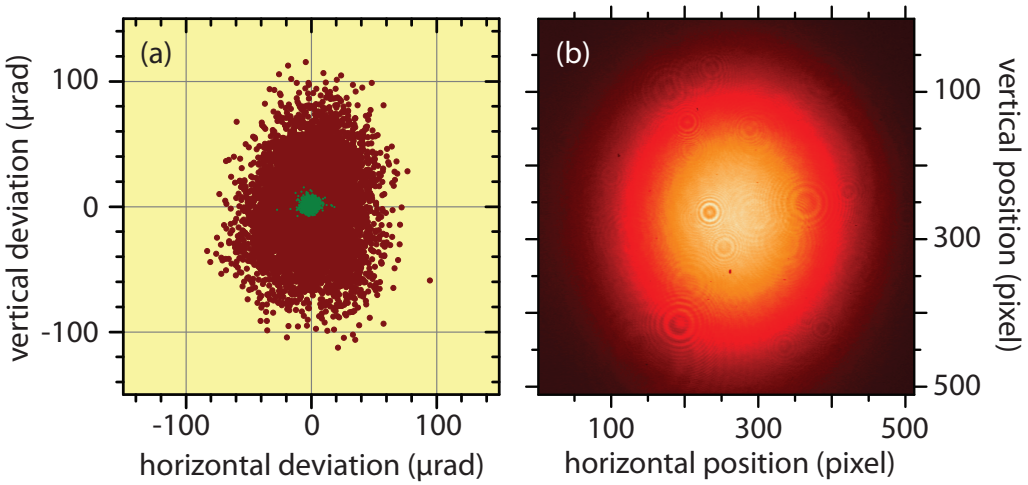


Figure 2.6: (a) Angular beam pointing with deactivated (red) and activated (green) beam stabilization system; (b) transversal mode of the regenerative amplifier (1 pixel = 4.65 µm); both at a distance of about 10 m from outcoupling thin-film polarizer.

# Chapter 3

# Generation of High-Energy THz Pulses

Efficient deflection of sub-relativistic free electron pulses by THz radiation requires high peak electric fields, which imply tight focussing and high pulse energy. From the variety of different THz generation methods [77–82], optical rectification in a nonlinear medium combines high output pulse energies [83, 84] and simplicity together with a table-top design.

Several materials are suitable for optical rectification, see e.g. [85–87] and table 3.1. The large bandgap of lithium niobate ($LiNbO_3$) excludes two- and three-photon-absorption of 1030-nm pump pulses [88] and makes this crystal especially useful for high power applications when doped with magnesium.[1] It has also one of the highest effective nonlinear coefficients [86, 89] and its relatively high linear absorption coefficient reduces significantly at cryogenic temperatures [90], which gives this material potential for further scalability.

However, the efficiency of optical rectification significantly depends on velocity matching between the group velocity of the generating infrared pump pulse $v_{\mathrm{gr}}^{\mathrm{ir}}$ and the phase velocity of the generated THz field $v_{\mathrm{ph}}^{\mathrm{THz}}$. As indicated in table 3.1, the refractive index of lithium niobate is more than two times larger in the THz spectral range ($n_{\mathrm{ph}} = 4.96$) than the group index in the near infrared ($n_{\mathrm{gr}} \approx 2.2$) [80, 90], thus inside the crystal the pump pulse group velocity is more than two times larger than the THz phase velocity. Therefore additional effort has to be spend on velocity matching, whereby tilting the front of the pump pulses proved to be an effective approach [87, 91].

[1] Free carriers created by multi-photon-absorption strongly absorb the generated THz radiation.

| Material | $d_{\text{eff}}$ (pm/V) | $E_{\text{g}}$ (eV) | $\alpha_{\text{THz}}$ ($\text{cm}^{-1}$) | $n_{\text{gr}}$ (800 nm) | $n_{\text{ph}}$ (1 THz) |
|---|---|---|---|---|---|
| CdTe | 81.8 | 1.43 | 4.8 | | 3.24 |
| GaAs | 65.6 | 1.43 | 0.5 | 4.18 | 3.59 |
| GaP | 24.8 | 2.27(i) | 0.2 | 3.67 | 3.34 |
| | | 2.48(d) | | | |
| ZnTe | 68.5 | 2.26 | 1.3 | 3.13 | 3.17 |
| GaSe | 28.0 | 2.02 | 0.5 | 3.13 | 3.27 |
| $LiNbO_3$ | 168 | 3.8 | 17 | 2.25 | 4.96 |

Table 3.1: Properties of typical materials used for THz generation by optical rectification [80, 85]. The absorption coefficient is given for 1 THz, the indicated effective nonlinear coefficients are given for 800 nm.

## 3.1 Pulse Front Tilting

Inside a nonlinear crystal, the infrared pump pulse excites the THz radiation in form of a phonon-polariton. In accordance with Huygens' principle, the phonon-polariton propagates perpendicular to the pump pulse front with the velocity $v_{\text{ph}}^{\text{THz}} = c/n_{\text{THz}}$. Is the pulse front tilted with respect to the phase front by an angle $\gamma$, so is this angle also enclosed between the propagation direction of the THz radiation and the propagation direction of the pump pulse. This allows to compensate the significant velocity mismatch by satisfying the equation:

$$\cos\gamma = \frac{v_{\text{ph}}^{\text{THz}}}{v_{\text{gr}}^{\text{ir}}} = \frac{n_{\text{gr}}^{\text{ir}}}{n_{\text{ph}}^{\text{THz}}} \tag{3.1}$$

In case of lithium niobate and a central wavelength of 1030 nm, the required tilt angle $\gamma$ amounts to 63° inside the crystal. This implies an even larger tilt angle $\bar{\gamma}$ of about 77° outside of the medium, since the intensity front tilt angle decreases due to refraction when the pulse enters the crystal according to:

$$\tan\gamma = \frac{1}{n_{\text{gr}}^{\text{ir}}}\tan\bar{\gamma} \tag{3.2}$$

Typically, such large tilt angles are achieved by introducing angular dispersion by means of a grating and subsequently imaging the grating into the crystal. Thereby, the tilted pulse front has to coincide with the grating image over the pump beam transversal mode. Fülöp et al. derived in [85] the

relations for setup optimization using paraxial ray optics, which are summarized below. More elaborated theoretical consideration can be found in [92, 93]. Figure 3.1, reproduced from [85], illustrates the corresponding scheme. The infrared beam falls at the incidence angle $\theta_\mathrm{i}$ onto the grating with the period length $p$ and is diffracted at the angle $\theta_\mathrm{d}$, which is also the tilt angle of the grating. The lens with an focal length $f$, placed at the distance $s_1$ to the grating, images the grating into the crystal and determines the magnification factor. The lithium niobate crystal is located at a distance $s_2$ with respect to the lens. The depth of the image $s$ inside the crystal is chosen such that the image is not truncated, the fluence at the entrance face is minimized and self-focusing is avoided.

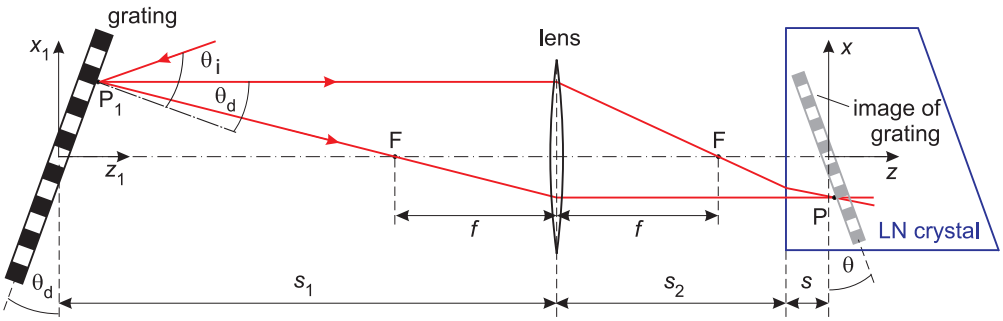


Figure 3.1: Pulse-front tilting scheme. The figure is reproduced from [85]. The pulse-front of an incident optical pulse is tilted due to angular dispersion at the grating. The grating is located in the object plane of a focussing lens, which images the diffracted pulse into the nonlinear crystal.

For a given nonlinear material with refractive index $n(\lambda_c)$, group index $n_g(\lambda_c)$, grating period $p$, focal length $f$, image distance $s$ and auxiliary parameter $a$ the geometry of the setup is determined by the equations 3.3 to 3.7:

$$a = \frac{n^2(\lambda_c)\, n_g(\lambda_c)\, p}{2\lambda_c} \left( \sqrt{\frac{\lambda_c^2}{n_g^2(\lambda_0)\, p^2 \tan^4\gamma} + \frac{4}{n^2(\lambda_0)}} - \frac{n^2(\lambda_c)}{2\tan^2\gamma} \right) \tag{3.3}$$

$$\sin\theta_d = \frac{\lambda_c}{n(\lambda_c)\, n_g(\lambda_c)\, p} a \tag{3.4}$$

$$\sin\theta_i = \frac{\lambda_0}{p} - \sin\theta_d \tag{3.5}$$

$$s_1 = f\left(\sqrt{a} + 1\right) \tag{3.6}$$

$$s_2 = \frac{f s_1}{s_1 - f} - \frac{s}{n(\lambda_c)} \tag{3.7}$$

Setup analysis based on paraxial ray optics, as presented above, does not take into account effects like geometrical and chromatic aberrations. These effects can induce distorted THz beam profile and phase fronts, when used in connection with extended transversal beam profiles and significant angular dispersion. In femtosecond systems the mismatch between grating's surface and object plane of the imaging lens was shown to cause temporal distortions over the pump beam profile [94]. These influences are neglected here, because of narrow bandwidth and long durations of the infrared pump pulses, but needs to be taken into account in next generation setups.

## 3.2 Experimental Setup

### 3.2.1 Geometry

Figure 3.2 illustrates the experimental setup, implemented based on these considerations. About 1 ps, 360 µJ pulses at 50 kHz at a central wavelength of 1030 nm are available for pumping the THz setup (see chapter 2.2). The combination of a half-wave-plate with a 45° thin-film polarizer allows for power adjustment of the p-polarized transmitted beam. The beam is expanded and collimated in a telescope (Edmund Optics, SN: 68481) to about 6 mm (FWHM) to avoid damage on the 400 lines/mm gold grating (Richardson Gratings Inc.). The grating is placed at an angle of 4.6° with respect to the surface normal. After being diffracted, the first-order beam is steered into the crystal by two flat 2"-alluminium mirrors. A plane-convex, 1"-lens with a focal length of 150 mm is used to image the grating into the crystal. The lens is placed at the distance of 1750 mm to the grating. Using a wedge placed behind the imaging lens, a small portion of the beam has been sent onto a beam profiler (DataRay Inc., WinCamD) located at the image plane of the lens and indicating an beam size of $710 \times 670\,\mu m^2$. A half-wave plate, following the lens, aligns the pump beam polarization along the z-axis of the 0.6% MgO-doped stoichiometric lithium niobate ($LiNbO_3$) prism to become

parallel to the axis of pulse-front tilt. The front face of the $LiNbO_3$ crystal is located 166 mm after the imaging lens. THz radiation leaves the crystal at the exit face, cut at 63°. It is collimated by a 2", 90° off-axis aluminium parabola with a focal length of 50 mm. The remaining pump beam is directed to a beam dump.

In total, a rather large demagnification ratio of about 1:10 was realized in the setup. This is necessary to compensate for the significantly different damage thresholds of the gold grating and the lithium niobate crystal. At a laser repetition rate of 300 kHz, damages were found to occur at the peak intensity of about 0.7 $GW/cm^2$ and 110 $GW/cm^2$ for grating and crystal, respectively. Regarding imaging distortions, the optimal demagnification would be about 1:2 [85]. However, the large demagnification factor in this setup is considered to be not critical to imaging distortions, since a relatively small illuminated area at $LiNbO_3$ is pumped with rather long pulses (about 1 ps). Furthermore, small incidence and diffraction angles at the grating approximate the ideal condition for minimized temporal distortions at 0° diffraction angle [94].

### 3.2.2 Optimization of Pulse-Front-Tilt

Careful alignment of the pulse front tilt in the pump beam is a decisive step for efficient THz generation with the presented method. The pulse front tilt within the crystal is experimentally not accessible. Therefore the tilt in the image plane outside the crystal was determined to verify and optimize the setup alignment.

This is accomplished with a Mach-Zehnder interferometer using the beamsplitter BS1 to create a reference beam, marked with a dashed line in figure 3.2. Another beamsplitter BS2 provides spatial recombination. The pulse front tilt differs in both arms: whereas the grating introduces a tilt in the one arm, the pulse front remains not tilted in the other. Introducing a wedge after the imaging lens, the recombined beams were sent onto a beam profiler placed in the image plane of the lens. Temporal overlay was achieved varying the length of the second arm by means of a delay stage.

Figure 3.3 (a) illustrates the transversal profile of the combined beam in the image plane. Clearly visible is a vertically oriented interference strip. Its horizontal position depends on the delay between the pulses in both arms. Figure 3.3(b) reveals a linear dependence between the interference position on the delay within the measurement accuracy. The slope of the inverse function corresponds directly to the pulse front tilt and has been determined to about 77.5°, which is in a good agreement with in section 3.1 calculated value of 77°.

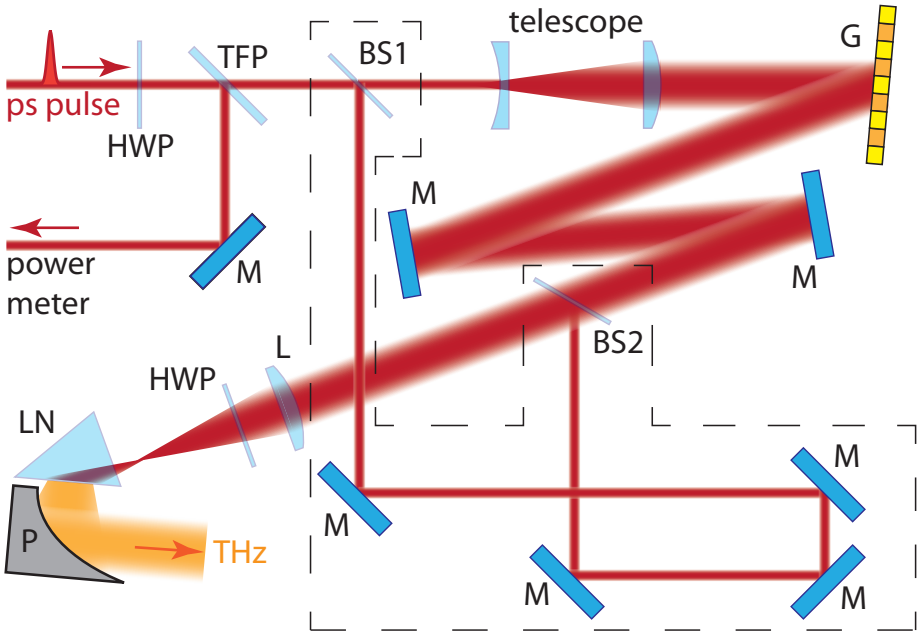


Figure 3.2: Optical layout of the THz setup. HWP, half-wave plate; TFP, thin-film polarizer; BS1 and BS2, beam splitter; G: gold grating; M, plane mirror; L, imaging lens; LN, lithium niobate crystal; P, collimating off-axis parabola. The reference arm for measuring the pulse front tilt is marked with a dashed line.

### 3.2.3 Results

**Power and efficiency:** In a first investigation, the power of the emitted THz radiation as a function of infrared pump power was recorded with a pyroelectric detector (Gentec-EO). Figure 3.4 (a) shows the observed relation, where the input power is understood as the optical power transmitted into the $LiNbO_3$.[2] The indicated THz power is corrected by the transmission of a 4 mm Si-filter (about 54 %), which was used to attenuate the scattered infrared radiation. Each data point represents a mean value over 200 measurements taken within about 20 seconds, the relative standard deviation is below 5 %. The measurement reveals an approximately quadratic output dependence for low input energies, which gradually turns into linear dependence with increasing input powers. This indicates the onset of saturation

[2]The power delivered into the crystal is reduced by the efficiency of the optical system, which amounts to about 0.76 with main loss contributions originating from the grating efficiency (0.86) and the Fresnel reflections (0.14) at the crystal's entrance face.

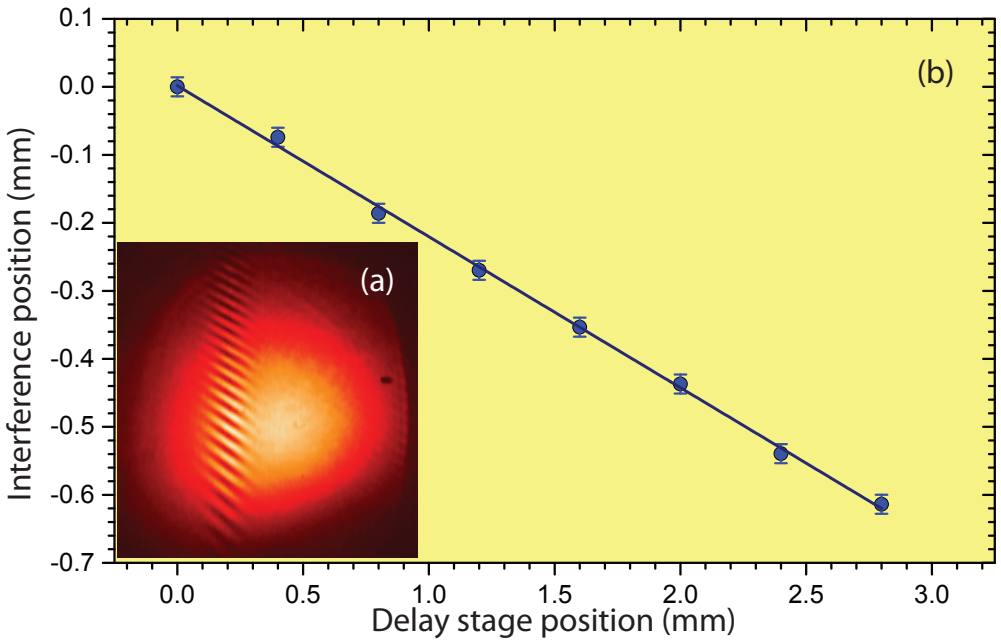


Figure 3.3: Measuring the pulse front tilt. (a) Interference pattern observed by overlapping a tilted and an untilted pulse in space and time. (b) Horizontal displacement of the interference pattern as a function of the delay stage position.

that is probably caused by increased multi-photon absorption. Crystal damage was once found to occur at about 6.5 W of transmitted average power (sending about 8.5 W into the setup), which corresponds to a pulse energy of 130 µJ and a peak intensity of about 22 GW/cm$^2$. The damage occurred in form of breaking off the crystal rearward corner, probably caused by excessive internal tensions due to temperature gradients. Below the threshold, the highest measured THz output power was 1.6 mW corresponding to 30 nJ pulse energy. Figure 3.4 (b) depicts the obtained energy efficiency. It increases linearly with input energy for powers of up to about 2 W with a slope of approximately $3.75 \times 10^{-6}$ µJ$^{-1}$. In the range between 2 W and 4 W the slopes magnitude gradually reduces, thus the conversion efficiency becomes constant for pump powers above 4 W. The maximum reached pump-to-THz conversion efficiency amounts to about $2.8 \times 10^{-4}$ corresponding to 27 % of quantum efficiency. These values come close to state-of-the-art [88] but here were obtained with significantly longer pulses[3].

[3] In [88] 300 fs-pulses at 1035 nm were used to pump the $LiNbO_3$ crystal.

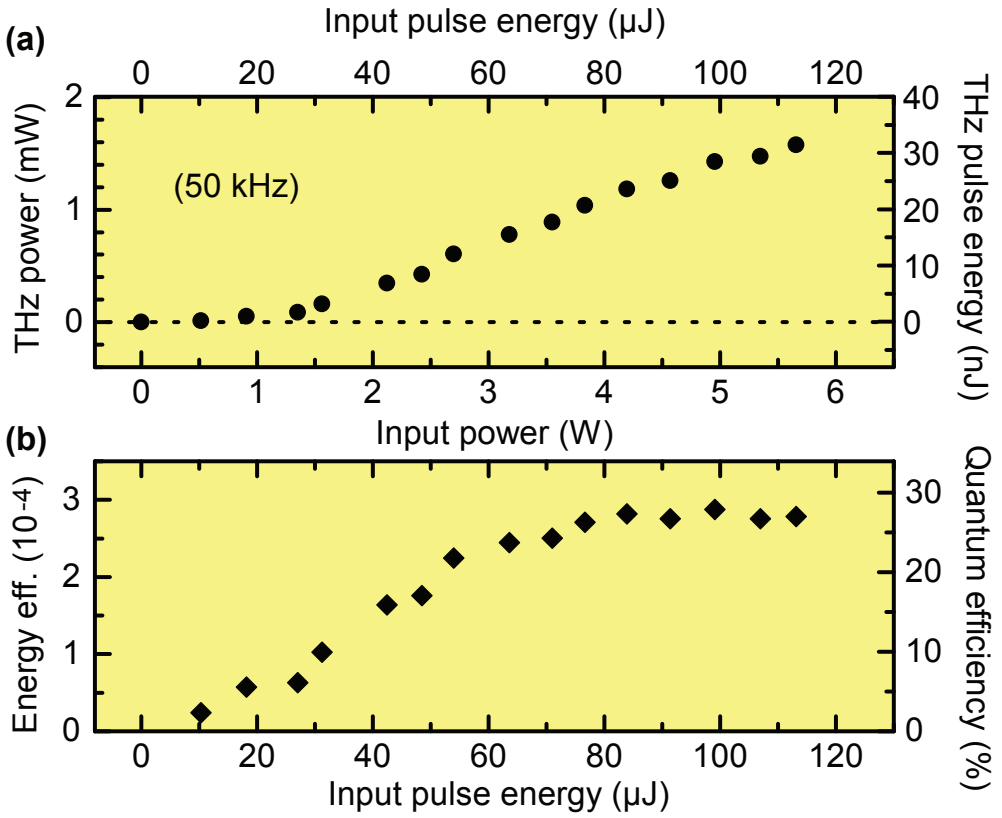


Figure 3.4: Performance of THz generation with tilted pulses in $LiNbO_3$. (a) Output power and THz pulse energy in dependence of the input power and pulse energy. (b) Energy conversion ratio and quantum efficiency.

**THz beam parameters:** The THz beam parameters like beam divergence and spot size at the source have essential influence on further system design. The spot size at the source influences smallest achievable focus when no magnifying telescopes can be used and the beam divergence affects the size of the collimated beam. Therefore both parameters have been experimentally determined.

To estimate the beam divergence the THz output radiation from the prism's exit face was observed with a pyroelectric detector (Gentec-EO). Scanning the beam-profile at different distances from the exit face, the horizontal and vertical THz beam divergence was determined to about 18° and 40° (total angular spread), respectively.

To estimate the source size, the infrared pump spot outside the crystal

and in grating image plane, was measured to $710 \times 670$ $\mu m^2$ (horizontal $\times$ vertical, full-width at half maximum). Taking into account a tilt angle of 63° this results in a THz-emitting area[4] of $1560 \times 670$ $\mu m^2$. Furthermore, the THz radiation was collimated and refocused to a spot size of about $1.4 \times 0.74\,mm^2$, using two 2", 90° off-axis parabolic mirrors with a focal length of 50 mm. The size of the collimated beam was found to be about 2 cm (full-width at half maximum). Thus the generated THz radiation can be collected to the most part and tightly focused with still reasonable efforts, which makes the optical rectification in a tilted pulse-front configuration a valuable method for further applications.

**Electro-optic sampling:** Information about temporal characteristics of the electric field is required to estimate the deflection of electron pulses. Electro-optical sampling (EOS) is a well established method [95, 96] to determine the time-structure of a THz pulse and it was used to analyse the output from our setup. Figure 3.5 (a) shows the time-dependent electric field recorded in an EOS measurement[5] using a 300 µm thick GaP crystal. With electro-optical coefficients of GaP, given in [97], the field amplitude was determined to about 11 kV/cm. The duration of the close to single-cycle field oscillation is around 3.3 ps. The Fourier-transformation of the electric field amplitude reveals the output's spectral amplitude centred at 0.3 THz, as illustrated in figure 3.5 (b). The observed field shape, as well as the values for its amplitude and period are used in section 4.2.6 to predict the dependence of the electron deflection on its relative delay to the THz pulse.

## 3.3 Possibilities for Further Scaling

For the here intended THz-electron control experiments, the achieved nJ-pulses at 50 kHz are well sufficient, see chapter 5.4. Still, further scaling up the THz-pulse energy would result in higher streaking fields and is therefore preferable. There are several options for increasing the THz output power from a lithium niobate crystal.

One approach could be the reduction of thermally induced internal tensions in the $LiNbO_3$ crystal, which depend on the size of the heat source (pumped volume), on crystal's geometry, on cooling scheme and mounting design. Assuming that the internal tensions can be kept below the damage threshold by suitable measures and the regime of constant efficiency extends

[4] If a more symmetrical and uniformly divergent output is required, cylindrical optics could be used to shape pump beam's cross section.

[5] EOS measurements have been carried out together with Andrey Ryabov.

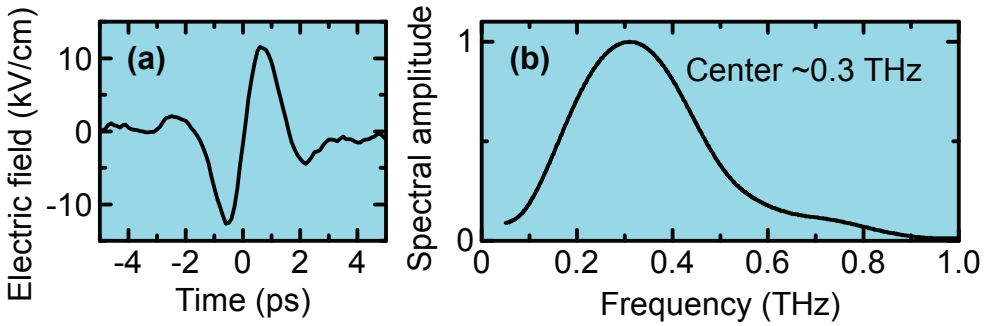


Figure 3.5: Characterization of the THz pulses. (a) Time-dependent electric field of the THz pulses with peak strength of about 11 kV/cm and (b) the normalized THz spectrum at full output power (spectral amplitude).

beyond pump pulse energies of 120 µJ, one could expect a THz output pulse energy of about 90 nJ when pumping the crystal with available 330 µJ-pulse. This would correspond to an average power of about 4.5 mW at the repetition rate of 50 kHz or even 27 mW at 300 kHz.

Another approach could be the cryogenic cooling of the $LiNbO_3$ crystal. This would significantly reduce materials absorption coefficient for THz radiation from 17 $cm^{-1}$ at 300 K to 4.8 $cm^{-1}$ at 100 K [90] and thus result in higher conversion efficiency. Experimentally, an conversion efficiency close to 4 % was reached at about 150 K [98].

Furthermore, the conversion efficiency can be increased using optimized pulse duration [85], which is at room temperature around 500 fs, and by increasing the pumped interaction area [99], where different geometry concepts might be advantageous [100, 101].

# Chapter 4

# Concept for THz-Driven Electron Deflection

## 4.1 Overview and Motivation

The characterization of ultrashort electron pulses for time-resolved diffraction is, besides their generation, a precondition for advancing ultrafast electron imaging towards ever higher resolutions. One possible approach for electron pulse characterization is realized in the so called image-tube streak camera [102, 103]. The device maps the temporal profile of a bunch of photoelectrons into a spatial dimension by deflecting them in a rapidly varying electric field.

The invention of the atomic transient recorder (ATR) allowed to surpass the resolution of a conventional image-tube streak camera by three orders of magnitude and thus to achieve a sub-femtosecond resolution [104, 105]. The concept of ATR consists in mapping the temporal electron structure into the energy domain instead of spatial domain by using the cycles of a laser field. Together with the production of attosecond pulses by means of high-harmonic generation [106, 107], the ATR contributed to open up the field of attosecond physics [32]. The concept was used for characterisation of attosecond light pulses [107], sampling the electric field of light [108], gaining information about the electronic properties of atoms [23] and the photoemission process [25]. At DESY (Deutsches Elektronen-Synchrotron), the method was transferred towards longer wavelengths to realize a terahertz-field-driven X-ray streak camera [109] that was used for single-shot characterisation of 50 fs soft X-ray pulses delivered from FLASH (Freie-Elektronen-Laser in Hamburg).

Recently, an optical-field-driven streak camera for characterisation of ultrashort free electron pulses at 25 keV was demonstrated [47]. The apparatus was used for characterization of a microwave-compressed free electron pulses

[40] and offers field-induced cross-correlation in contrast to ponderomotive approaches [43–46].

Despite of these great achievements however, the latter concept is not directly applicable to the conditions faced in this work, for two reasons. Firstly, its working principle is based on the cross-correlation between an optical pulse and the electron pulse. The method is therefore only practicable for electron pulses with durations clearly different from that of the used optical pulse. Secondly, the concept makes use of a time-of-flight spectrometer for analysis of electron's kinetic energy, which has been scaled up to 90 keV in the present setup. However, a time-of-flight spectrometer in this energy bandwidth is currently not available

Therefore, the new concept here is, first, to move with the optical pulse into a spectral domain where the electron pulse is shorter than half the optical cycle that means into the terahertz (THz) domain and, second, to map the temporal structure of the electron pulse into a spatial domain. Thus the approach combines the concept of the streaking with electric field of light and the simplicity of an image-tube streak camera.

## 4.2 Physical Background

The success of the attosecond streak camera[1] is mainly based on two physical preconditions that the device fulfils in a natural way.

Firstly, the electron wave-packet is released from a bound atomic state at location and instant within an already oscillating streaking field. This way the released electron abruptly enters a region of space with present field, without having to transverse regions of steadily increasing amplitude. This enables an efficient momentum exchange of a free electron with an electromagnetic field of an optical pulse. For low intensity optical pulses, this condition represents a fundamental prerequisite, since the spectrum of an electromagnetic pulse contains no dc-component and therefore an interaction of a charged particle over complete pulse duration results into an absence of net momentum transfer.[2]

Secondly, the release is triggered by a colinearly propagating sub-laser-cycle extreme ultraviolet pulse that was previously generated by the same streaking pulse, thereby avoiding any considerable timing jitter of the release time with respect to the phase of the laser pulse. The consequence is,

[1] The terms "attosecond streak camera" and "atomic transient recorder" are used synonymously in this thesis.

[2] The pondermotive force is neglected here, since the intensity of optical pulses is rather low.

firstly, that the electrons are released at the same phase of the streaking field (in particular independently of the release location), and secondly that the reproducibility of the process from pulse to pulse is ensured.

Thus two conditions need to be met for a successful transfer of the ATR-concept. Section 4.2.1 describes the method to provide an abrupt start or stop of field-electron interaction. Whereas 4.2.2 deals with the spatial phase synchronization of this interaction process.

### 4.2.1 Condition 1 - Abrupt Interaction Stop

Single-electron pulses for ultrafast electron deflection are generated in a photo-emission process at a distant location. To create a condition where the electron wave packet can enter abruptly the streaking field, like it does for the attosecond streak camera, one has to resort to a trick. The concept is to reflect the laser pulse off a mirror in order to, create a situation where space is separated into an area with electromagnetic field and a field-free area. The propagating electron wave packet will abruptly enter or leave the optical field (depending on whether the reflection takes place on the backside or the front side of the mirror).

The mirror itself has to fulfil two contrary, essential requirements. On the one hand it must have a sufficiently high electron transmission, on the other hand it has to provide high reflectivity for the optical pulse. An ultra-thin metal film, ideally of a material with low atomic mass, with a thickness in the range of several tens of nanometers offers transmission values of a few tens of percent for sub-relativistic electrons.[3]

To estimate the field reflectivity of a metal film, one has to take into account that its high conductivity generates high internal absorption, so that a complex refractive index has to be used to describe correctly the optical properties of a real metal at optical frequencies. Thereby the real-valued Fresnel equations, which are often used to describe the reflectance and transmittance of an approximately lossless medium, have to be replaced by its complex valued counterparts. Introducing the complex refractive index as $\hat{n} = n\,(1 + i\kappa)$ with real refractive index $n$ and extinction coefficient $\kappa$, and defining the complex angle $\Theta_\mathrm{t}$ using the incidence angle $\theta_\mathrm{i}$

$$\sin\Theta_\mathrm{t} = \frac{1}{\hat{n}}\sin\theta_\mathrm{i} \tag{4.1}$$

it has been shown [110, 111], that the Fresnel equations describing the field reflectance $r$ as well as the field transmittance $t$ at the interface between

[3] In the present work about 30% of 90 keV electrons were transmitted by aluminium foils of about 70 nm in thickness.

vacuum and an absorbing medium for p-polarization are given by

$$r_{\mathrm{p}} = \frac{E_{\mathrm{p}}^{\mathrm{r}}}{E_{\mathrm{p}}^{\mathrm{i}}} = \frac{\hat{n}\cos\theta_i - \cos\Theta_t}{\hat{n}\cos\theta_i + \cos\Theta_t} \tag{4.2}$$

$$t_{\mathrm{p}} = \frac{E_{\mathrm{p}}^{\mathrm{t}}}{E_{\mathrm{p}}^{\mathrm{i}}} = \frac{2\ \cos\theta_{\mathrm{i}}}{\hat{n}\cos\theta_{\mathrm{i}} + \cos\Theta_{\mathrm{t}}} \tag{4.3}$$

$$\tag{4.4}$$

Similarly, for the incidence of an s-polarized beam it was obtained

$$r_{\mathrm{s}} = \frac{E_{\mathrm{s}}^{\mathrm{r}}}{E_{\mathrm{s}}^{\mathrm{i}}} = \frac{\cos\theta_i - \hat{n}\cos\Theta_t}{\cos\theta_i + \hat{n}\cos\Theta_t} \tag{4.5}$$

$$t_{\mathrm{s}} = \frac{E_{\mathrm{s}}^{\mathrm{t}}}{E_{\mathrm{s}}^{\mathrm{i}}} = \frac{2\ \cos\theta_{\mathrm{i}}}{\cos\theta_{\mathrm{i}} + \hat{n}\cos\Theta_{\mathrm{t}}} \tag{4.6}$$

These complex valued reflectance and transmittance coefficients contain information about the amplitude and the phase of the reflected and transmitted wave. The coordinate systems used with the Fresnel equations given above can be found in [110, 111].

Empirical values for the refractive index in the frequency range from 0.1 THz to 1 THz are hardly available, even if values of $n \approx n\kappa \approx 1000$ for 0.3 THz were reported [112, 113]. Alternatively, the THz spectral range satisfies the limit of low frequencies $\omega\tau \ll 1 \ll \omega_{\mathrm{p}}\tau$ and therefore the optical constants of a metal can be approximated by [114]

$$n = n\kappa = \sqrt{\frac{\omega_{\mathrm{p}}^2\tau}{2\omega}} \tag{4.7}$$

where $\omega_{\mathrm{p}}$ stands for plasma frequency and $\tau$ is the average time between two electron collisions. With a plasma frequency $\omega_{\mathrm{p}} = 1.6 \times 10^{16}\ s^{-1}$ and a relaxation time $\tau \approx 20$ fs the equation 4.7 gives refractive indexes between 1160 and 640 at 0.3 THz and 1 THz, respectively. Using Fresnel equations with these values the field reflectance of an interface between vacuum and a metal can be approximated to be higher than 99.5 % for incidence angles of up to 70°. These high reflectance values ensure an abrupt transition between field free and field oscillating regions over the thickness of the foil.

An upper limit for the transition duration can be given by considering the thickness of the foil and the propagation velocity of the free electrons. An electron propagating at $0.5\,c$ passes the 70 nm thick foil within 470 as, so that the transition duration is about three orders in magnitude shorter than the optical cycle of the THz wave and can therefore be considered as quasi-instantaneous. This confirms that a thin metal foil provides a suitable method for an abrupt start or stop of field-electron interaction.

### 4.2.2 Condition 2 - Velocity Matching

The rather low dependence of the field reflectance on the incidence angle in the THz domain offers in the first instance a large degree of freedom for the experiment, limited only by the divergence of the THz beam. However, one should note that the case of close-to-normal incidence has to be excluded here, since it would require a colinear propagation of the electron beam with the THz beam.

Considering the situation classically, in a colinear configuration at the instant when an electron wave-packet reaches the foil, it would have interacted with the leading edge of the incident pulse and with the reflection of this leading edge, see figure 4.1 (a). Since the reflected field undergoes a phase shift of 180°, the contributions to the momentum transfer from incident field and the reflected field are of same magnitude but of opposite sign. This results in no net momentum transfer. Here one should note that the classical explanation might be insufficient for electrons approaching relativistic kinetic energies.

In opposite to the colinear configuration, for oblique incidence of the THz beam an electron wave packet will interact only partially with the reflected pulse allowing for a more efficient momentum transfer, but requires additional measures to ensure a spatially uniform electron deflection.

In the plane wave approximation an oblique incidence implies that the velocity of the THz phase front at the metal film $v_{\mathrm{THz}}^{\mathrm{foil}}$ is given by the component of the phase velocity along the film and is therefore higher then the vacuum speed of light $c$, see figure 4.1 (b). The electron beam has a typical transverse extent of a few to several hundreds of micrometer, depending on whether it's collimated or focused on the screen. The electron pulse front propagates with the velocity $v_{\mathrm{e}}^{\mathrm{foil}}$ along the film. To ensure the electron gains the same momentum independently of its transversal position in the beam requires that it leaves or enters the interaction area at the same phase of the propagating THz field. This requirement is fulfilled, if the electron pulse front and the THz phase front move with the same velocity along the film. It couples the electron incidence angle $\alpha_{\mathrm{e}}$ to the THz incidence angle $\alpha_{\mathrm{THz}}$ for a given electron velocity $u_{\mathrm{e}}$ according to the following equation

$$v_{\mathrm{e}}^{\mathrm{foil}} = \frac{u_{\mathrm{e}}}{\sin \alpha_{\mathrm{e}}} = \frac{\mathrm{c}}{\sin \alpha_{\mathrm{THz}}} = v_{\mathrm{THz}}^{\mathrm{foil}} \tag{4.8}$$

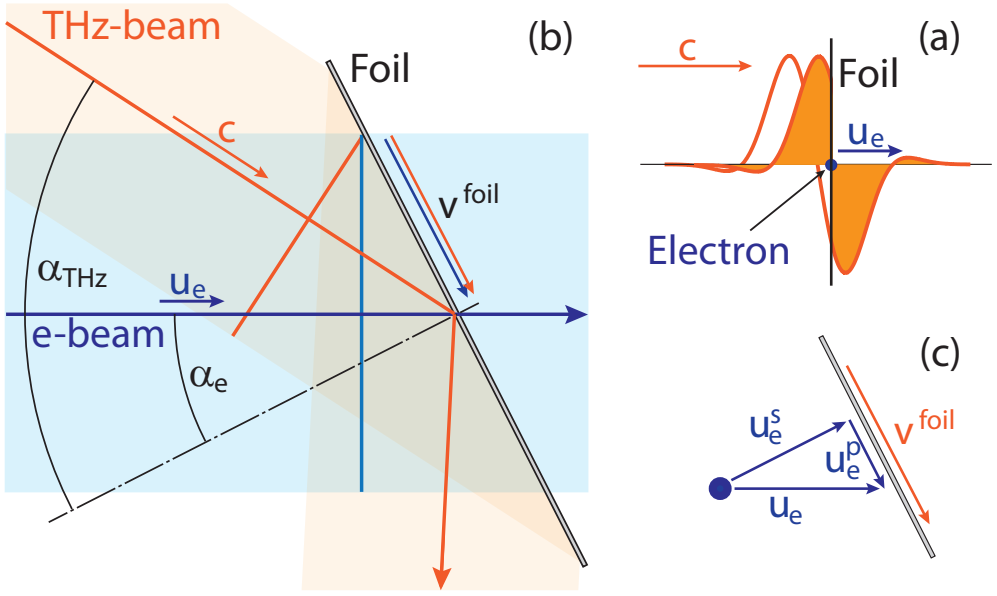


Figure 4.1: Scheme for velocity matching at a metal foil. (a) A configuration with collinear propagation and perpendicular incidence of electrons and THz pulse on the metal foil. The electron interacts with incident part of the THz-pulse twice, first time when the THz wave-packet propagates towards the foil (dashed area behind the foil) and a second time when it is reflected (dashed area in front of the foil). (b) This double interaction is avoided in a configuration with oblique incidence for the THz beam. Velocity matching condition (see text) results in a noncollinear propagation of the THz beam and the electron beam. (c) Velocity difference in components along the foil results in relative motion of the THz phase front with respect to the electron.

### 4.2.3 Effects of Spatiotemporal Trajectories

Matching the velocities of the THz phase-front and the electron pulse-front at the thin foil does not mean that the velocity component of an individual electron along the foil is equal to that of the THz phase-front. According to the equation 4.8, in the velocity-matched case the velocity of the THz pulse-front at the foil can be given in terms of the electron beam parameter as $u_e/\sin\alpha_e$. The velocity component of an individual electron along the foil is given by $u_e^p = u_e \sin\alpha_e$, see figure 4.1 (c). This results in the following

velocity difference

$$v^{\text{foil}} - u_{\text{e}}^{\text{p}} = \frac{u_{\text{e}}}{\sin\alpha_{\text{e}}} - u_{\text{e}}\sin\alpha_{\text{e}} \tag{4.9}$$

$$= \frac{u_{\text{e}}}{\sin\alpha_{\text{e}}}\left(1 - \sin^2\alpha_{\text{e}}\right) \tag{4.10}$$

$$= v^{\text{foil}}\cos^2\alpha_{\text{e}}, \tag{4.11}$$

which creates a relative motion of the THz phase-front with respect to the electron wave-packet as it approaches the foil. This means, even if the electron arrives at the foil at some specific THz phase, it does not interact with the THz field of this phase only, but it interacts over a time-interval of the THz field oscillation. In opposite to the attosecond streak camera, where the interaction takes place from the precise moment of electron release until the very end of the streaking pulse, the interaction period here is determined by the incidence angles $\alpha_{\text{e}}$, $\alpha_{\text{THz}}$, the electron velocity $u_{\text{e}}$ and electron travelling distance in the field, see also 4.2.4.

As a reference value one can estimate the time needed for the interaction with exactly one THz cycle at the foil. Note that one cycle at the foil surface is given by the component of the THz wavelength $\lambda$ along the film: $\lambda^{\text{p}} = \lambda/\sin\alpha_{\text{THz}}$. Assume the electron initially to overlap with the THz phase-front, then the velocity difference 4.11 will cause a spatial separation equal to $\lambda^{\text{p}}$ after the time

$$\delta t = \frac{\lambda^{\text{p}}}{v^{\text{prj}} - v_{\text{e}}^{\text{p}}} = \frac{\lambda\tan\alpha_{\text{e}}}{u_{\text{e}}\sin\alpha_{\text{THz}}\cos\alpha_{\text{e}}} \tag{4.12}$$

For experimentally implemented parameters $\alpha_{\text{THz}} = 60°$, $\alpha_{\text{THz}} = 27°$, $\lambda = 1\,\text{mm}$ and $u_{\text{e}} = 0.52\,c$ one obtains the interaction time of $\delta t = 4.2\,\text{ps}$, which corresponds to a electron propagation distance of about $\delta s = 0.66\,\text{mm} = 0.66\,\lambda$. For propagation times smaller than this reference value the interaction will be of sub-cycle type, whereas for larger times the electron would interact with more than one field oscillation.

### 4.2.4 Field Distribution at Perfect Conductor

In the section 4.2.3 it was implicitly assumed that the reflection of a THz pulse results in a localized electromagnetic field at the foil which propagates along this foil. Here the justification for this assumption is provided.

To estimate the spatial extent of the THz field the formation of the electric field at the thin metal film reflecting an incident few-cycle THz-pulse was investigated in a two-dimensional finite-element simulation. Model geometry was implemented as a half-circle with 10 mm radius which contains a

cutout as shown in the inset of figure 4.2. The geometry is encircled by five boundaries in total. The boundary given by circles diameter (blue in inset of figure 4.2) represents the metal foil, which encloses an angle of 30 ° with the THz propagation direction. It was set to be a perfect conductor fulfilling the equation $\mathbf{n} \times \mathbf{E} = 0$, where $\mathbf{E}$ and $\mathbf{n}$ stand for the electric field vector and boundary normal vector, respectively. Lower circle segment and the boundaries originated from the cutout were defined as perfectly matched layer, which fully absorb incident electromagnetic radiation. Left circle segment (red in inset of figure 4.2) was used to couple in a tightly focussed few-cycle, p-polarized Gaussian pulse by defining the electric field at this boundary as

$$\begin{aligned} E(\zeta, \xi, t) = E_0 \sqrt{\frac{w_0}{w(\zeta)}} \exp\left(-\frac{\xi^2}{w(\zeta)^2}\right) \\ \times \cos\left(\omega_0 t - k_0 \zeta + \eta(\zeta) - \frac{k_0 \xi^2}{2R(\zeta)^2}\right) \\ \times \exp\left(-\frac{(t-t_0)^2}{dt^2}\right) \end{aligned} \tag{4.13}$$

The real-valued equation 4.13 is a product of a Gaussian envelope in time and a two-dimensional Gaussian beam [115]. The latter deviates from the standard, three-dimensional definition in amplitude by the square root of spot-to-radius ratio and in the Gouy-phase defined with a factor 1/2

$$\eta(\zeta) = \frac{1}{2} \arctan\left(\frac{\zeta}{\zeta_0}\right) \tag{4.14}$$

The spot radius $w_0$ and wavelength $\lambda$ were set to 0.85 mm and 1 mm, respectively, which corresponds to 1 mm (FWHM) and a frequency of 0.3 THz.

The geometry was meshed with quadrilateral elements of 0.1 mm maximal edge size to sufficiently resolve the electromagnetic wave. Pulse propagation was simulated by numerically solving the governing wave equation for time-dependent vector potential $\mathbf{A}$

$$\mu_0 \sigma \frac{\partial \mathbf{A}}{\partial t} + \mu_0 \epsilon_0 \frac{\partial}{\partial t}\left(\epsilon_\mathrm{r} \frac{\partial \mathbf{A}}{\partial t}\right) + \nabla \times \left(\frac{1}{\mu_\mathrm{r}} \nabla \times \mathbf{A}\right) = 0, \tag{4.15}$$

with permittivity of free space $\epsilon_0$, relative permittivity $\epsilon_\mathrm{r}$, permeability of free space $\mu_0$, and electrical conductivity $\sigma$.

Figure 4.2 illustrates the simulation result at the time when the THz pulse is reflected off the foil. It shows the field component perpendicular to the electron propagation direction, which is relevant for transversal electron deflection. The simulation indicates a build up of an interference wave

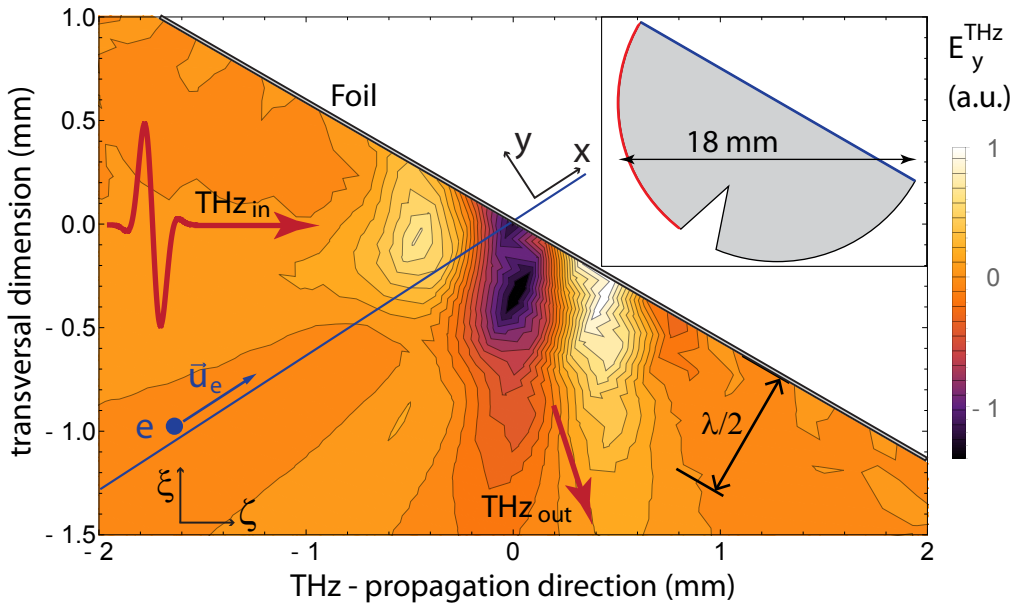


Figure 4.2: Electric field interference pattern at the boundary of a perfect conductor for an instant during the reflection of a few-cycle optical pulse. Here, the field component perpendicular to the electron propagation direction is shown (y-component). Inset shows the complete simulation geometry with the field incoupling boundary (red) and the foil boundary as a perfect electric conductor (blue).

propagating along the film until the pulse is completely reflected. The interference field extends approximately $\lambda/2$ into the free space resulting in a localized, moving interaction region. An electron wave-packet propagates in a non-colinear direction with respect to interference wave. It therefore gradually enters the interference wave at a phase determined by the delay between the THz pulse and the electron pulse and interacts with this wave until it reaches the foil leaving the interaction region. Within the travelling time the interference field passes the electron, so that the interaction takes place over some interval of the wave. As was shown in section 4.2.3, this interval is determined by the velocity difference between the interference wave and the electron velocity parallel to the foil. In the same section a required interaction length of $0.66\,\lambda$ was estimated for the implemented configuration to provide an interaction with one THz cycle. Here, the limitation of the interference wave to $\lambda/2$ in front of the metal foil induces an interaction length of $\lambda/\left(2\cos 27°\right) = 0.56\lambda$ and therefore implicates a sub-cycle type interaction.

The sub-cycle interaction in case of free electron deflection at a foil constitutes a significant difference compared to the attosecond streak camera. As will be shown in chapter 4.2.6, the interaction interval shorter as the cycle of the streaking field results in a different deflection trace than would be expected from a simple consideration of vector potential only.

### 4.2.5 Estimation of Effective Field Amplitude

In case of an attosecond streaking camera, the momentum change is generated by the electric field of a freely propagating light pulse. The contribution from the magnetic field can be neglected to a good approximation, since the electron bunches having kinetic energies of about 100 eV do not reach relativistic velocities. This is not the case for free electron pulses propagating at velocities around $0.5\,c$, where the magnetic fields need to be taken into account. Moreover, the formation of the interference wave considered above results from the superposition of incident and reflected fields. The amplitude of this wave depends on the amplitudes of individual fields as well as on the relative phase-shift between them.

In general, both amplitude and phase of the reflected field is determined by wavelength and angle dependent complex field reflectivity of the metal film. Additionally, the reflected field acquires an phase-shift due to extra propagated path length. In a first approximation, the metal film is considered as a perfect conductor which results in no amplitude change and a phase-shift of exactly $\pi$ for the reflected beam. This is in a good agreement with the results obtained in section 4.2.1. The phase-shift due to path difference is neglected here, thus giving an upper limit for the amplitude of the interference wave.

Generally, the momentum change of a particle carrying the elementary charge $-e$ and moving at velocity $\mathbf{u}$ in an electromagnetic field with electric field $\mathbf{E}(\mathbf{r},t)$ and magnetic field $\mathbf{B}(\mathbf{r},t)$ is described by the Lorentz force:

$$\frac{d}{dt}\mathbf{p}(\mathbf{r},t) = -e\left(\mathbf{E}(\mathbf{r},t) + \mathbf{u}\times\mathbf{B}(\mathbf{r},t)\right) \tag{4.16}$$

In case of a reflection from a metal film, the electric and magnetic field components are a superposition of incident $\mathbf{E}^{\mathrm{in}}(\mathbf{r},t)$, $\mathbf{B}^{\mathrm{in}}(\mathbf{r},t)$ and reflected $\mathbf{E}^{\mathrm{ref}}(\mathbf{r},t)$, $\mathbf{B}^{\mathrm{ref}}(\mathbf{r},t)$ fields, causing an interference field as was shown in figure 4.2. With approximations described above one can estimate the effective field amplitudes contributing to transversal and longitudinal momentum change.

Figure 4.3, (a) illustrates the conditions for oblique incidence of a p-polarized beam. The drawing plane represents the plane of incidence of the THz-wave. The electron propagates within this plane under an angle of

$\delta = \alpha_{\mathrm{THz}} - \alpha_{\mathrm{e}}$ with respect to the wave vector $\mathbf{k}^{\mathrm{in}}$. The amplitude vector of the electric field $\mathbf{E}^{\mathrm{in}}$ lies in the plane of incidence and the amplitude of the magnetic field $\mathbf{B}^{\mathrm{in}}$ points normal out of it. The figure 4.3 (b) shows the conditions for the reflected beam, thereby the wave vector $\mathbf{k}^{\mathrm{ref}}$ encloses an angle of $180° - (\alpha_{\mathrm{THz}} + \alpha_{\mathrm{e}})$ with the electron velocity vector $\mathbf{u}$. The orientation of the electric field vector $\mathbf{E}^{\mathrm{ref}}$ was obtained from Fresnel equations 4.2. The amplitude vector of the magnetic field $\mathbf{B}^{\mathrm{ref}}$ is then defined by the wave vector $\mathbf{k}^{\mathrm{ref}}$ and the electric field vector $\mathbf{E}^{\mathrm{ref}}$.

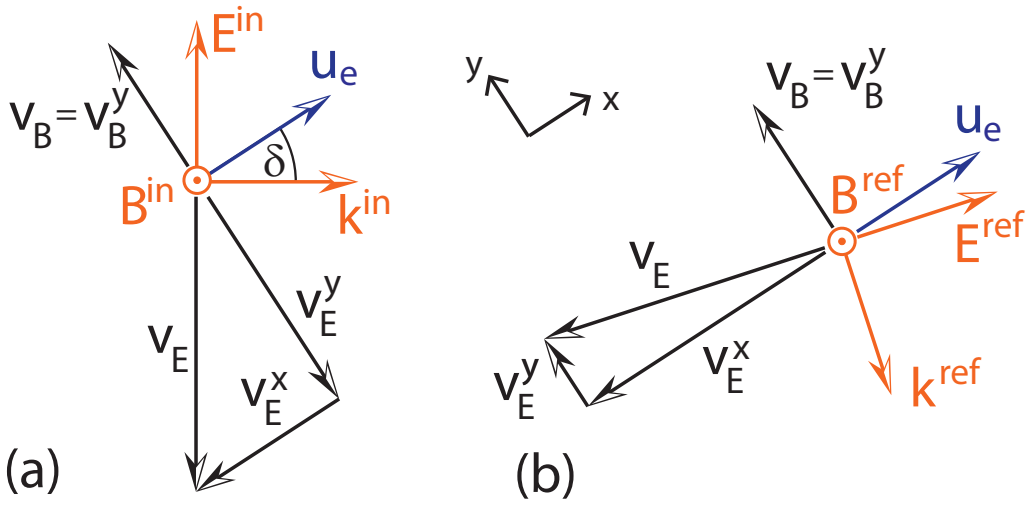


Figure 4.3: Orientations of the electric and magnetic field amplitudes at a foil for (a) the incident beam and (b) the reflected beam. Phase-shift due to reflection at the thin film is taken into account.

As illustrated in figure 4.3 the B-field vector points perpendicular to the electron velocity direction $\mathbf{u}$ for both the incident and reflected beams, so that they both contribute to the transversal momentum change only. Moreover the B-field does not change its direction upon reflection and therefore the contributions from incident and reflected magnetic fields will add up. The E-fields contribute to the transversal and longitudinal momentum change with their respective projections. A contribution to momentum change out of plane of incidence does not exist, since only p-polarized waves are considered. Defining a coordinate system such that the x-axis points along the electron propagation direction and the y-axis shows perpendicular to it, the

components of the momentum change can be written as:

$$\frac{d}{dt}\begin{pmatrix} p_\mathrm{x} \\ p_\mathrm{y} \\ p_\mathrm{z} \end{pmatrix} = -e \begin{pmatrix} E_\mathrm{x}^\mathrm{in} + E_\mathrm{x}^\mathrm{ref} \\ E_\mathrm{y}^\mathrm{in} + E_\mathrm{y}^\mathrm{ref} - u_\mathbf{e}\, B_\mathrm{z}^\mathrm{in} - u_\mathbf{e}\, B_\mathrm{z}^\mathrm{ref} \\ 0 \end{pmatrix} \tag{4.17}$$

The Fresnel equations show that for wavelength used in this work the field reflectance of a metal film is higher than 0.99 for incidence angles of up to about 70°, which justifies the approximation $|\mathbf{E}^\mathrm{in}| \approx |\mathbf{E}^\mathrm{ref}|$. The B-field of an electromagnetic wave in vacuum propagates in phase to the E-field and is proportional to it as $|\mathbf{B}| = c^{-1}|\mathbf{E}|$. With projections given by $E_\mathrm{x}^\mathrm{in} = |\mathbf{E}^\mathrm{in}| \sin(\alpha_\mathrm{THz} - \alpha_\mathrm{e})$, $E_\mathrm{x}^\mathrm{ref} = |\mathbf{E}^\mathrm{ref}| \sin(\alpha_\mathrm{THz} - \alpha_\mathrm{e})$, $E_\mathrm{y}^\mathrm{in} = |\mathbf{E}^\mathrm{in}| \cos(\alpha_\mathrm{THz} - \alpha_\mathrm{e})$ and $E_\mathrm{y}^\mathrm{ref} = -|\mathbf{E}^\mathrm{ref}| \cos(\alpha_\mathrm{THz} + \alpha_\mathrm{e})$ the equation 4.17 becomes

$$\frac{d}{dt}\begin{pmatrix} p_\mathrm{x} \\ p_\mathrm{y} \\ p_\mathrm{z} \end{pmatrix} = -e \begin{pmatrix} \sin(\delta) + \sin(\theta) \\ \cos(\delta) - \cos(\theta) - 2\beta \\ 0 \end{pmatrix} |\mathbf{E}^\mathrm{in}| \tag{4.18}$$

where the abbreviations $\delta = \alpha_\mathrm{THz} - \alpha_\mathrm{e}$, $\theta = \alpha_\mathrm{THz} + \alpha_\mathrm{e}$ and $\beta = u/c$ are used. The equation 4.18 defines an effective field amplitude $\mathbf{E}^\mathrm{eff}$ according to:

$$\mathbf{E}^\mathrm{eff} = \begin{pmatrix} \sin(\delta) + \sin(\theta) \\ \cos(\delta) - \cos(\theta) - 2\beta \\ 0 \end{pmatrix} |\mathbf{E}^\mathrm{in}| \tag{4.19}$$

Equation 4.19 is useful to answer the question about the optimum combination of incidence angles $\alpha_\mathrm{THz}$ and $\alpha_\mathrm{e}$ that maximize the effective field amplitude $\mathbf{E}^\mathrm{eff}$ for transversal deflection or for longitudinal acceleration of an electron. The maximum transversal effective field amplitude is approximately obtained when the magnitude of the expression

$$\frac{E_\mathrm{y}^\mathrm{eff}}{|\mathbf{E}^\mathrm{in}|} = \cos(\alpha_\mathrm{THz} - \alpha_\mathrm{e}) - \cos(\alpha_\mathrm{THz} + \alpha_\mathrm{e}) - 2\beta \tag{4.20}$$

is maximized. In this expression the first and the second cosine term originate from the incident and reflected waves, respectively. The third term, depending on the electron velocity only, originates from the sum of the incident and reflected magnetic fields. The two cosine terms in equation 4.20 compensate each other at normal incidence angle of at least one of the beams. At such a point the electric field contributions from the incident and reflected wave cancel out, which results in a deflection generated purely by the sum of magnetic fields. Furthermore the superposition of electric fields is positive and increases monotonically with increasing incidence angles reaching its maximum value at the virtual value of $\alpha_\mathrm{THz} = \alpha_\mathrm{e} = 90°$.

Figure 4.4 illustrates the expression 4.20 for $\beta = 0.52$ and THz- and electron incidence angles between 0° and 90°. Not all of these angle combinations are of practical interest, but only those that fulfil the velocity matching condition 4.8, shown in the figure as a blue curve. The set of useful angle combinations is further limited by the divergence of the THz-beam that reduces the maximum incidence angle $\alpha_{\mathrm{THz}}$ and by the minimum required angle difference $\delta$ of approximately 30°.[4] In the particular velocity-matched case, where $\delta = 33°$, $\theta = 87°$ and $\beta = 0.52$, the effective field becomes $-0.2\,|E^{\mathrm{in}}|$; because $|\cos(\delta) - cos(\theta)| < |2\beta|$, the contribution from the magnetic field is effectively larger and therefore predominantly responsible for transversal momentum change.

Similarly, maximum longitudinal acceleration is approximately obtained for maximized magnitude of the effective field in electrons propagation direction that is the case when the magnitude of the expression

$$\frac{E_{\mathrm{x}}^{\mathrm{eff}}}{|\mathbf{E}^{\mathrm{in}}|} = \sin(\alpha_{\mathrm{THz}} - \alpha_{\mathrm{e}}) + \sin(\alpha_{\mathrm{THz}} + \alpha_{\mathrm{e}}) \tag{4.21}$$

takes its maximum value. As in the case of transversal deflection, the first and the second sine term originate from the incident and the reflected waves, respectively. They compensate each other for normal incidence of the THz-wave and for grazing incidence of the electron beam. In turn, the maximum value of the equation 4.21 is reached when the THz beam falls at 90° onto the foil and simultaneously the electron beam propagates at 0° towards the foil. In opposite to transversal deflection there is no magnetic field contribution. The contour plot in figure 4.4 (b) shows the value of expression 4.21 at incidence angles of up to 90°. As before, the set of useful angle combinations is reduced by velocity matching condition 4.8, indicated by the blue line in figure 4.4 (b), as well as by the finite size of the focusing mirror and the divergence of the THz beam.

### 4.2.6 Estimation of Electron Deflection

In section 4.2.3 it was pointed out that electron velocity component along the foil differs from the phase-velocity of the THz field at the foil. Further, it was shown in section 4.2.4 that the electron interacts with a propagating streaking wave formed by the superposition of incident and reflected THz-fields at the foil. With these results it was found that due to the non-collinear motion of the resulting interference wave with respect to the electron pulse, the interaction process can start at any phase of the streaking field and the

[4] A minimum angle difference is required to allow the electron beam to pass the mirror.

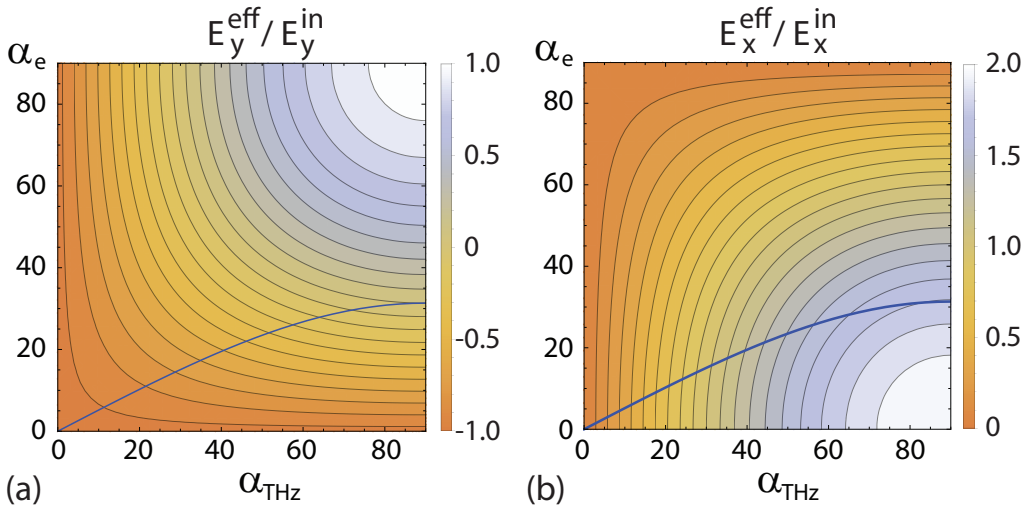


Figure 4.4: The approximated electric and magnetic field amplitudes are combined in an effective field amplitude $E^{\text{eff}}$. The contour plots show its transversally deflecting (a) and longitudinally accelerating (b) components, both normalized to the incident electric field, as a function of the THz and electron incidence angle $\alpha_{\text{THz}}$ and $\alpha_{\text{e}}$. The electrons kinetic energy was set to 90 keV. The meaningful angle combinations are restricted by velocity matching condition 4.8, here represented by the blue curve.

interaction duration is shorter than one cycle of the streaking field. In section 4.2.5 the deflecting field amplitude was found to reduce significantly, mainly due to the non-negligible contribution of the magnetic field. These special conditions, compared with the attosecond streaking technique, need to be taken into account when predicting the deflection of an electron pulse at a thin metal-film.

According to figure 3.5 (a), the incident THz-field is a sine-shaped, close-to single cycle oscillation, therefore the time-dependency of the interference wave at the foil is approximated as a sine carrier-wave with the period $T$ modulated by a Gaussian pulse envelope with an amplitude $A$ and a pulse duration $\tau_{\text{G}}$:

$$E_{\text{y}}^{\text{in}} = A \, \exp\left(-\frac{t}{\tau_{\text{G}}}\right)^2 \sin\left(\frac{2\pi}{T}\, t\right) \tag{4.22}$$

The period $T$ and the pulse duration $\tau_{\text{G}}$ are chosen such that the function 4.22 approximates the electric field obtained by electro-optical sampling. The amplitude $A$ in 4.22 is reduced firstly by the losses at the silicon window and secondly by a factor estimated with 4.20 for the effective field amplitude in

case of transversal deflection. Figure 4.5 (a) illustrates the obtained function.

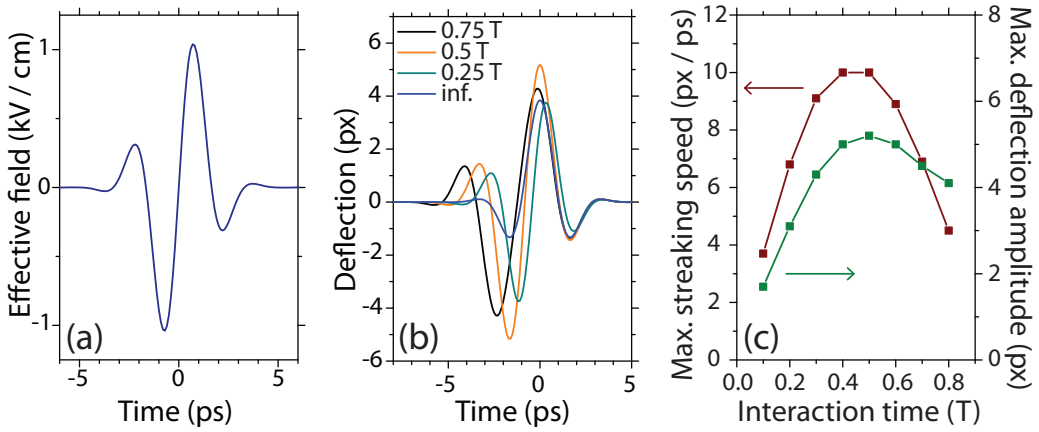


Figure 4.5: The interference wave at the foil was approximated by an effective field, which was modelled as a sine-wave with period $T$ modulated by a Gaussian envelope, to obtain a few-cycle pulse (a). The deflection amplitude and shape at the screen depend on the interaction time-interval, here in units of $T$ (b). Deflection amplitude and streaking speed attain maximum values for time-intervals close to half the oscillation cycle $0.5\,T$ (c).

The transversal momentum change $\Delta p_\mathrm{y}$ is then obtained from 4.18 as

$$\Delta p_\mathrm{y}(t) = -e \int_\mathrm{t}^{\mathrm{t}+\tau} E_\mathrm{y}^\mathrm{eff}(t)\, dt, \tag{4.23}$$

where the integral is taken starting from the time $t$ (when the electron enters the streaking field) over a finite time-interval $\tau$ (interaction period until it reaches the foil).

After the propagation of 680 mm long distance between foil and screen at the velocity $0.52\ c$ the finite transversal momentum results in a deflection shown in figure 4.5 (b). Note, that the deflection trace shows similar shapes as the effective field for interactions shorter than the streaking cycle. Only for intervals several times longer then the field-cycle the trace turns towards a shape shifted by $\pi/2$ as expected from attosecond streaking camera. The deflection amplitude reaches its maximum peak-to-peak value of 10 pixels (corresponding to $156\,\mu\mathrm{m}$) for an interaction interval of half the streaking cycle and drops for both longer and shorter intervals, see figure 4.5 (c). Accordingly, the maximum streaking speed given by the gradient of

the deflection is reached for an interaction interval around half the streaking cycle.

In the previous chapter an interaction interval larger than half the streaking cycle was estimated, so that a peak-to-peak deflection of about 8 pixel (around 125 µm) would be expected. As will be shown in the next chapter, a peak-to-peak deflection of 6 pixel has been experimentally demonstrated, which is only 20 % smaller than the predicted value. Here one should note that the predicted value represents an upper limit for the maximum deflection signal, since the phase shift due to path difference between incident and reflected beam was neglected and therefore the amplitude of the streaking field was overestimated. Furthermore, dependence of the streaking field formation on the spatial coordinate has been not included, so that areas with steadily increasing fields where approximated by the time-dependent maximum effective field.

It is illustrative to compare the deflection amplitude estimated above to that obtained by estimating the deflection according to the attosecond streaking theory. Here the magnetic field would be negligible and the electric field of the THz pulse would contribute to the electrons momentum change. The integration would be taken from the time $t$ over an infinite time-interval as

$$\Delta p_{\mathrm{y}}(t) = -e \int_{\mathrm{t}}^{\infty} E_{\mathrm{y}}(t)\, dt \tag{4.24}$$

$$= -e \cos(\alpha_{\mathrm{THz}} - \alpha_{\mathrm{e}}) \int_{\mathrm{t}}^{\infty} E(t)\, dt \tag{4.25}$$

With otherwise same parameters one obtains an approximately four times larger deflection of 30 pixels (or around 470 µm). Furthermore, from a sine-shaped streaking field one would expect a cosine-shaped deflection.

## 4.3 Summary

In this chapter the concept of an attosecond streak camera was transferred to the freely propagating sub-relativistic electron pulses. The novel technique exploits the reflection of an obliquely incident THz pulse from a thin metal-film that is transparent to the electrons. The angle of incidence for streaking beam and electron beam are chosen to fulfil the velocity matching condition, by which the electron pulse front and the streaking field phase front propagate with the same velocity along the film. The optical reflection causes an interference between incident and reflected parts, forming an interference

pattern close to the foil that moves along it. The momentum transfers to the freely propagating electron by interaction with this wave.

In contrast to the attosecond streak camera, several effects have to be taken into account. Firstly, the electron-field-interaction interval is typically shorter than the period of the streaking interference wave. Secondly, the amplitude of the streaking wave is a superposition of incident and reflected fields. Thirdly, magnetic fields have significant contributions in the interaction process. These effects have been implemented in a simple analytical model that predicts the shape and the strength of the deflection signal. Comparing the calculated values with experimental results show a good agreement.

# Chapter 5

# Experiments on Electron Deflection by THz Fields

Considerations discussed in the previous chapter 5 indicate the feasibility of deflection of sub-relativistic electron pulses by THz fields at a thin metal foil. The present chapter describes the implementation of this concept and demonstrates the transversal electron deflection experimentally.

Starting with a general discussion of possible realizations, one certain implementation is motivated in section 5.1 and described in section 5.2. The essential alignment steps are then outlined in section 5.3. Section 5.4 demonstrates the deflection of free electron pulses by THz fields and contains the discussion of obtained results. Based on these results the duration of free electron pulses at the thin metal foil is determined. This is considered as the first realization of a THz driven streak camera. From this point of view, section 5.4.7 provides the conclusion of this chapter by firstly comparing the temporal resolution of the set-up in detail with the state of the art image-tube camera and secondly giving an outlook for further development.

## 5.1 Preliminary Remarks

The uniform deflection of free electrons at a thin metal foil requires an oblique incidence of both the THz beam and the electron beam. In the process, the incidence angles are not equal but coupled by equation 4.8, satisfying the velocity matching condition. The resulting non-collinear propagation of both beams can be practically implemented in a configuration horizontal or vertical to the optical table. In this work the rather unconventional vertical configuration has been realized which is illustrated in figure 5.1 and is explained in the following paragraphs.

The conventional way of an horizontal alignment would have the advantage of the full 360 deg range available for foil rotation around the z-axis with the existing 6-axis goniometer. In contrast, this option has also several disadvantages. Firstly, the focussing parabola would be placed above the goniometer sample plate that would limit the positioning range of the foil in its height. Secondly, a precise angle alignment usually requires long beam propagation distances for reference, which are not available within a vacuum chamber. Thirdly, the rotary positioner located on the top of the available goniometer would partially clip the incident THz-beam because of its large divergence.

The disadvantages listed above can be circumvented when implementing a vertical configuration, see figure 5.1. Here the THz beam propagates directly above the horizontally travelling electron beam. The angle between the beams is determined by the rotation of the focussing parabolic mirror around its optical axis and is conveniently adjusted by positioning the focal spot height relative to the height of the parabolic mirror. The foil positioning range along the z-axis is not limited by the focussing mirror, since it is placed even above the electron beam. Also the THz beam is not clipped by the rotary positioner, since it falls from above onto the foil.

Achieving the smallest possible spot size requires additional measures when parabolic mirrors are used for beam collimation and focusing. The transversal mode of a beam collimated by a parabolic mirror is not rotation-symmetric. For optimal focussing the orientation of the focussing parabolic mirror has to match the orientation of the transversal mode. Rotating the parabolic mirror around its optical axis requires a corresponding rotation of the transversal mode of the collimated beam. This is accomplished by oblique incidence of the collimated THz beam on the two flat steering mirrors. The corresponding incidence angles are conveniently determined with the help of an algebra system (Mathematica 10.0) using reflection matrices.

An oblique incidence onto a mirror would generally result in an elliptical polarization, since the field reflectance and phase shift are generally different for s- and p-polarized beams. This effect is negligible for reflections from aluminium mirrors and the spectral range used in this work, since the Fresnel equations 4.2 and 4.5 show that the field reflectance coefficients as well as the phase shifts for p- and s-polarization are in a good approximation equal as expected for a perfect metal. This ensures the incidence of an approximately linearly, p-polarized beam on the foil.

## 5.2 Setup

The collimated vertically polarized THz pulse, centered at 0.3 THz, is coupled into the chamber through a 6 mm thick silicon window of 60 mm in diameter at an angle of about 7.2° to the horizontal plane. Two planar three-inch mirrors steer the THz beam onto the off-axis parabolic mirror, such that the projection of the THz beam onto the horizontal plane describes a 45° reflection on both steering mirrors. The normal of the first and the second steering mirror enclose an angle of 13.8° and 8.8° with the horizontal plane, respectively. After the second steering mirror the THz beam propagates in a horizontal plane and falls under 45° onto the parabolic mirror. The 90° off-axis parabolic mirror (EdmundOptics, 47-107) with an diameter of two inch has a focal length $f$ of about 50 mm and focuses the THz beam to an estimated spot size of $2.3 \times 1.1$mm (FWHM) and simultaneously reflects it downwards to overlap with the electron beam propagating in the horizontal plane an angle of 33°. All reflective components are coated with an aluminium layer and have a protective coating.

The electron pulses, accelerated to approximately $0.52\,c$ and thus gaining a kinetic energy of about 90 keV, propagate in a horizontal plane across the experimental chamber towards the CMOS camera (Tietz Video and Image Processing Systems GmbH, TemCam-F416) with a pixel size of 15.6 µm. At the distance of about 680 mm in front of the camera the electron pulses hit the thin metal film and are attenuated to approximately 30 % of its original intensity by scattering and absorption in the metal foil.

A 70 nm thick aluminium film with a free aperture of approximately 10 mm is supported by a $(25 \times 12 \times 0.2)$ mm aluminium frame. It is mounted on an aluminium holder having a tilt angle of about 27° with respect to horizontal plane (electron beam incidence angle), resulting in an incidence angle close to 60° for the THz beam. The mount is placed on a non-magnetic six-axis goniometer (SmarAct GmbH, SmarPod 110.45) equipped with an additional rotary positioner (SmarAct GmbH, SR-5714-S-UHVT-NM), thus all six degrees of freedom in space are available for positioning and orientating the foil in the focus of the THz beam.

## 5.3 Alignment Procedure

The alignment procedure consists essentially of in total five steps. Firstly, the focussing parabolic mirror has to be aligned. Secondly, the electron beam needs to be focused on the camera. In the third step the spatial overlap between the THz and electron beam is established at the foil. The fourth

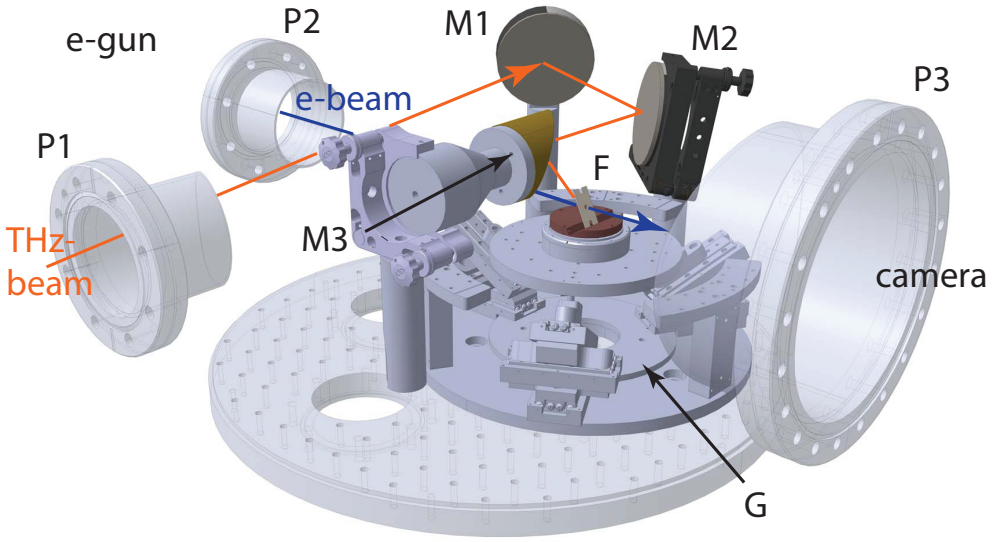


Figure 5.1: 3D-CAD-Model of the experimental chamber configuration for electron deflection. The THz beam is coupled through a Si-window (at entrace port P1) into the vacuum chamber and is steered by two flat 3in-Al-mirrors (M1 and M2) onto the off-axis parabolic mirror M3. The parabolic mirror focusses the THz beam at the thin aluminium foil F. Electron pulses enter the chamber through the port P2 and propagate towards the camera at port P3. The goniometer G allows to displace the foil in all six degrees of freedom.

step deals with the temporal overlap between the THz- and electron pulses. The last, fifth step consists of fine adjustment for velocity matching. In the following these steps are explained in more detail.

**Step 1: Alignment of the focussing parabolic mirror** To reach maximum field strength with a given pulse energy and pulse duration requires the tightest possible focus. Using an off-axis parabolic mirror avoids the problem of spherical aberration but demands precise alignment to prevent aberrations. Unfortunately, at present, suitable 2D imaging devices in the THz domain are still under development or are just in the beginning of their introduction on the market. Therefore the focusing parabolic mirror was aligned indirectly by means of a green alignment laser (Thorlabs GmbH, CPS532). The procedure consists of two tasks, collinear orientation of the parabolic

mirror with respect to the THz optical axis and mirror rotation around the optical axis to adjust the angle between THz- and electron beams. For this purpose, the alignment laser was placed into the THz beam path after the collimating parabolic mirror and oriented along the THz propagation direction. This defines the optical axis of the focusing parabolic mirror after the reflection at the second steering mirror, allowing for direction adjustment of the focusing mirror. Periodic shifting of the alignment laser along the transversal direction of the THz beam in the horizontal plane results in a displacement of the laser spot at the focusing mirror, indicating the required major axis orientation. This allows for rotation adjustment of the parabolic mirror, thereby determining the relative angle of the THz beam with respect to the electron beam. The same shifting of the alignment laser also causes a laser spot displacement in the focal plane, which stops when the optical axis of the parabolic mirror and its azimuthal angle are properly adjusted. The optimum angle of $\delta = 33°$ between the THz beam and the horizontally propagating electron beam is reached, if the focal spot is by $h = f \sin \delta$ lower than the optical axis of the parabolic mirror.

**Step 2: Electron beam focusing onto the camera** The previous step had ensured the maximum deflection of free electron pulses, resulting in a maximized displacement of the electron spot at the camera. Optimal detection of this displacement is achieved, if the ratio between displacement and spot size is maximized, which implies the smallest possible electron spot at the camera. Generally, this can be realized by introducing an aperture into the electron beam to clip it to the desired spot size or by focusing the whole electron beam onto the camera with a magnetic lens. The first option reduces the number of electron counts, thus deteriorating the signal-to-noise ratio. Therefore, the second approach was pursued in this work. The alignment procedure of the magnetic solenoid lens that is used to focus the electron beam is described in [50]. A current of 5.713 A was applied to reach the minimum spot size of about 125 µm (corresponding to 8 pixel) at the camera.

**Step 3: Spatial overlap of THz beam and electron beam at the foil** To achieve this task, a distinctive structure (e.g. the corner of thin-film frame) is first moved into the focus of THz beam to mark its position. Subsequently, the electron beam is steered to this corner by means of magnetic deflection coils. In the present work, currents of 0.238 A and −0.527 A were applied to shift the electron beam in horizontal and vertical direction respectively.

**Step 4: Temporal overlap of THz and electron pulses** To obtain the temporal overlap between the pulses the optical path lengths in the THz and the electron arm were matched with sub-centimeter precision, thereby taking into account the slower electron propagation velocity and the reduced speed of light in transmitting components. The remaining mismatch is then fine-adjusted by a delay line (LS110, PI miCos GmbH) implemented into the second harmonic path of the electron beam arm. To find the deflection signal, this delay line is scanned in 200-fs steps while recording images with an integration time of one second. Subsequently, the obtained electron beam profile was fitted with a Gaussian, providing position and size (FWHM) of the electron spot.

Figure 5.2 shows the obtained vertical displacement component of the electron spot within a delay range from −45 ps to 170 ps. Increasing delay times correspond to a shorter electron arm and therefore earlier electron generation. Thus the deflection at about 126 ps represents the first occurence of electron deflection[1]. This signal is followed by a second one with a relative delay of about 40 ps, originating from the electron interaction with the back-reflected pulse at the metallic sample mount[2]. A third signal is identified at the relative delay of 115 ps, caused by a copy of the first THz pulse that is generated at the double reflection in the silicon window. A fourth signal at −25 ps corresponds again to the pulse reflected from the sample mount.

Figure 5.2 indicates a stronger deflection for the second, back reflected pulse than for the original counterpart. This is the consequence of an insufficient velocity matching between the electron pulse and the THz streaking pulse at the foil. The resulting non-uniform deflection leads to spot distortions during the deflection process that produce incorrect, overestimating fitting parameters.

**Step 5: Velocity matching** A matched electron pulse front propagation to the propagation of the THz phase front along the foil requires the matching of the corresponding velocities. It ensures an electron-field interaction that is independent of transversal electron position in the beam, and thus a synchronous deflection of the entire electron beam.

Based on this insight, the following approach for experimental velocity matching has been realized. A collimated electron beam was partitioned into several individual electron beams. These beams were imaged on the camera and their displacements were traced for varying delays. The relative delay between individual deflections was used as a measure for velocity matching

[1] Scanning larger delays, from 175 ps to 500 ps, did not reveal another deflection signal.
[2] This signal is suppressed for a wedged mount surface.

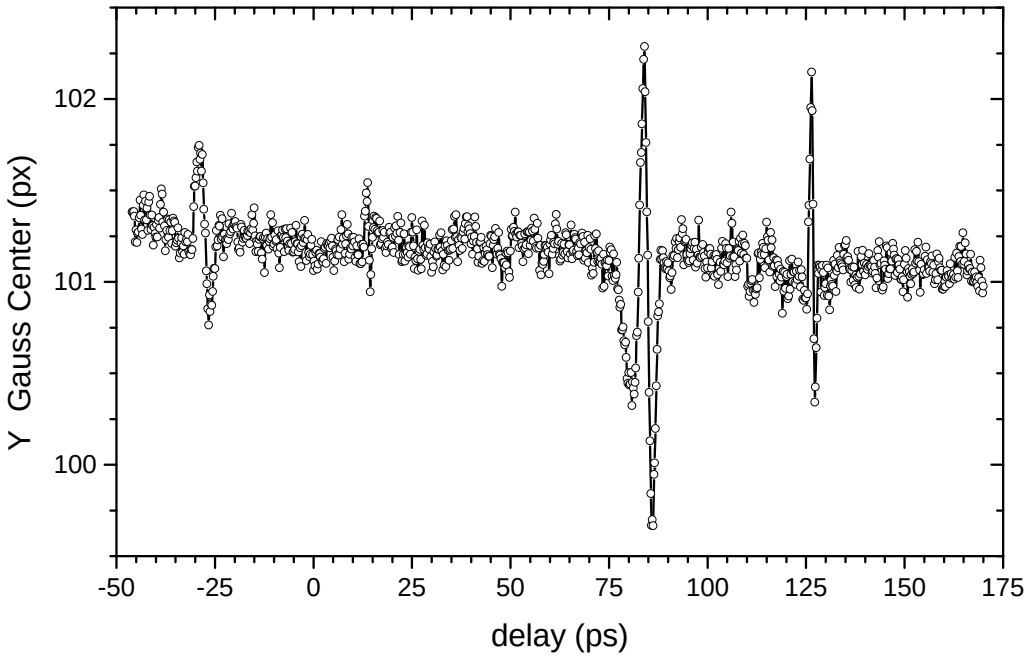


Figure 5.2: Delay scan over 225 ps showing four vertical deflection signals. Only the signal at 127 ps arises from the interaction with the original THz pulse, other signals are spurious interactions with reflections.

and was minimized to a sufficiently low magnitude by tuning the foils tilt angles.

To generate these parallel-propagating electron beams a home-made mask was placed into the expanded, collimated electron beam before the foil. The electron beam's full-width-of-half-maximum was about 600 µm. The mask was produced by drilling an array of holes with diameter and separation of 200µm into a 25 µm-thick foil using laser machining. Thereby a pulse energy of 100µJ at 1030 nm was required, which was provided by the regenerative amplifier described in chapter 2. Figure 5.3 (a) shows an image of the mask, taken with a reflected-light microscope. Figure 5.3 (b) shows the corresponding image of electron beams detected at the screen.

The vertical displacement of individual spots was sampled with a step size of 50 fs as a function of the delay between the electron pulse and the THz pulse. Figure 5.4 shows several time-traces taken at velocity-matched condition.

Figure 5.4 (a) depicts vertical displacement traces of two spots separated by 44 pixel or 686 µm in vertical direction. The delay between those traces

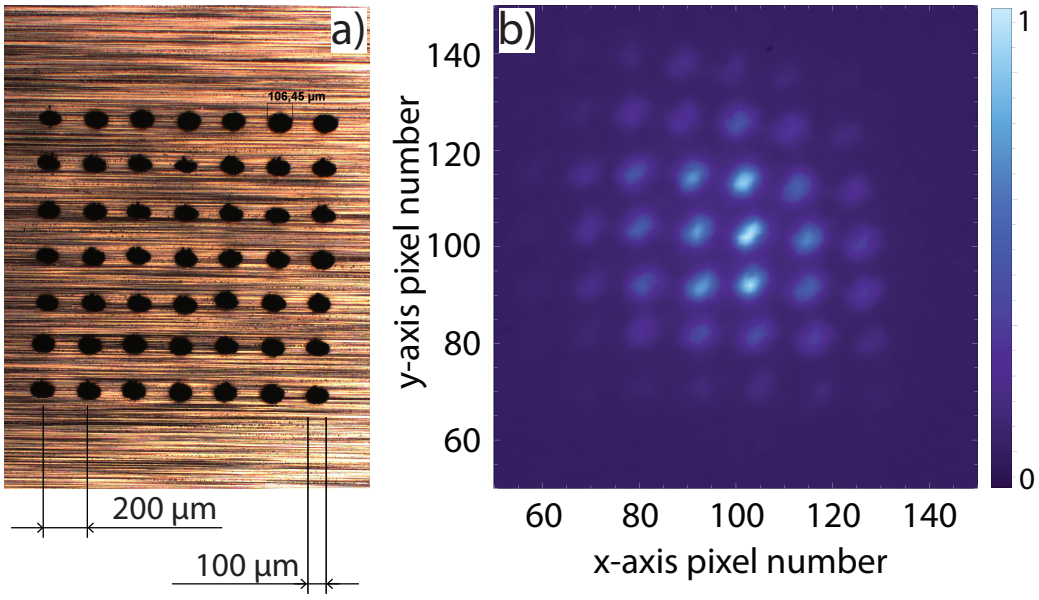


Figure 5.3: Experimental equipment for verification of velocity matching. A home-made mask (a) was placed into the collimated electron beam to obtain an array of individual electron beams (b). The relative deflection timing of individual beams allowed to verify the velocity matching.

amounts to about 600 fs. The comparatively large delay is a consequence of residual mismatch and the rather large beam size at the foil when the beam is collimated. In all relevant measurements the electron beam was focused onto the camera, which results in a smaller electron beam size at the foil by a factor of two. In this case the delay is estimated to reduce by the same factor to around 300 fs corresponding to a tenth part of the period of the THz streaking field.

Figure 5.4 (b) illustrates the relative delay in vertical displacement, but between spots separated in horizontal direction. Thereby a separation distance of about 450 µm revealed a relative delay of about 200 fs, in analogy to the upper case this results in a delay of less then 100 fs when the beam is focused onto the screen.

Effectively, this procedure represents an experimental method for a quantitative analysis of the residual velocity mismatch in both directions and thus provides reliable feedback for alignment.

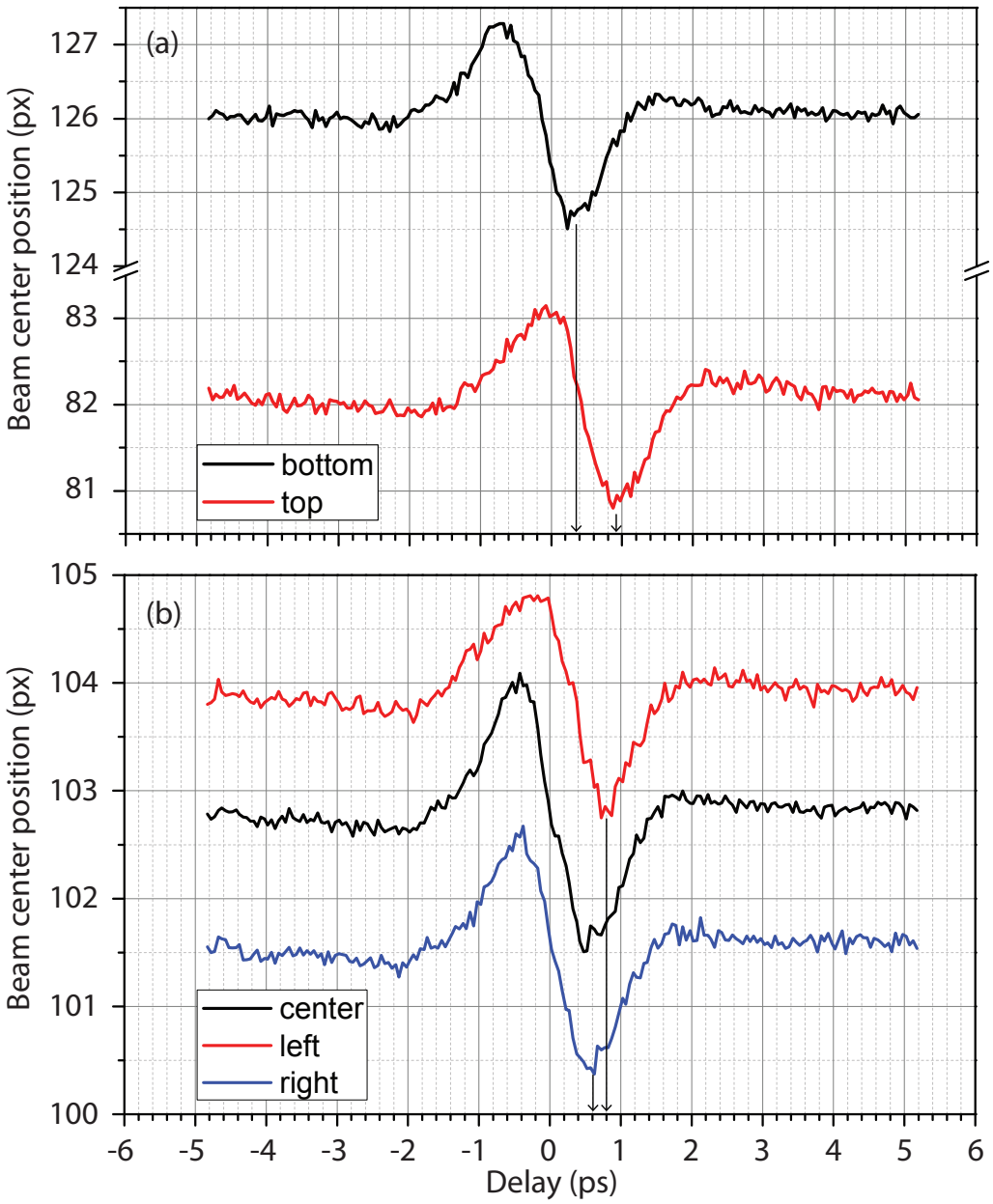


Figure 5.4: Verification of velocity matching. Tracing vertically (a) and horizontally (b) separated beam parts provides an indication about synchronism of the deflection process.

## 5.4 Experimental Results on Electron Deflection

After the alignment process described in the previous section, the setup was prepared for streaking deflection, in order to retrieve the duration of the electron pulses.

### 5.4.1 Displacement on Camera

Figure 5.5 illustrates the displacement of the electron spot at the camera due to THz-induced transversal momentum transfer at the foil. The upper row shows normalized images taken with an integration time of 1 s. The lower row pictures difference images obtained by subtracting an average image of a non-displaced beam. It is useful for identification of areas with surplus and deficit of electrons counts due to the deflection process. Bright and dark areas indicate increased and reduced count rates, respectively.

The THz-electron delay was scanned in 50-fs steps over a total range of about 13 ps. To combine an overall view with meaningful step size, the figure shows a scan interval of 7.2 ps containing the complete displacement signal. Delay-zero was set to the point, where the displacement crosses the zero line defined by the position of the unaffected electron beam. In the interval from −400 fs to +400 fs, the spot position underwent most significant change, therefore this interval is illustrated with a reduced step size of 200 fs.

The scan revealed a sine-shaped single-cycle displacement signal, see also figure 5.6. The non-displaced electron spot at −3.6 ps started gradually to shift from its original position, indicated by a dashed white line, into the upper half of the image and towards its maximum displacement of approximately 5 pixel (78 µm) at about −400 fs, while showing only moderate distortion of its shape. This distortion arose from the relatively long electron pulse duration with respect to the period of the THz streaking field. In the delay range from −400 fs to +400 fs, the spot underwent its maximum shift from its most upper position towards its lowest position in the lower half of the image, thereby showing strongest profile distortion at zero delay. The significant shape distortion originated from the sign change of the displacement signal at zero delay, so that the leading and trailing parts of the electron pulse were deflected in opposite directions. Within the interval from 0.9 ps to 3.6 ps the displacement reduced and the electron spot returns to its original position.

Considering the difference images in the second row of figure 5.5 one can clearly notice a surplus of electron counts at the delay of −400 fs in the upper

half of the image and simultaneously deficit of electron counts at the original, non-displaced beam position. Especially, no deflection into the lower part of the image is registered here. The situation changes into the opposite for the delay of +400 fs, showing no surplus of electron counts in the upper half of the image. At zero delay an surplus is detected in both the upper and the lower part of the image. This behaviour indicates that the complete electron pulse crosses over the displacement zero transition within the delay of 800 fs, estimating an electron pulse duration of approximately 800 fs.

### 5.4.2 Vertical Deflection Trace

For a more quantitative analysis, each image of the measurement series was integrated in rows or columns of the image array to obtain vertical or horizontal electron beam profiles, which were afterwards fitted with a Gaussian function. This way obtained fit parameters, center position and full-width-of-half-maximum diameter, were plotted versus the delay. Figure 5.6 and figure 5.7 display these traces in vertical and horizontal direction, respectively.

Figure 5.6 shows a sine-shaped displacement trace in vertical direction. The peak-to-peak amplitude of about 6 pixel (93.6 µm) is only two pixels smaller then the calculated value in section 4.2.6. Main deflection is accompanied with two minor lobes with significantly reduced amplitude of about 0.5 pixel (7.8 µm) in front and on the back of the signal. The deflection extrema are separated by approximately 1 ps in time. At the delay of zero picoseconds, the displacement signal attains its maximal slope of about −10.6 pixel/ps, which represents the maximum achieved streaking speed. Within a delay range of ±500 fs its deviation from linear relation is only about $2.3 \times 10^{-2}$. The beam width doubles from the original value of about 8 pixel (125 µm) to approximately 16 pixel (250 µm) when the electron pulse is maximally streaked at zero delay.

The propagation distance of 680 mm between the thin film and the detector is passed within about 4.4 ns. Within this time, the 90-keV electrons cover a distance of about 47 µm in transversal direction, thereby propagating at a velocity of 11 km/s, which corresponds to a transversal momentum of $9.8\,10^{-27}\,\mathrm{N \cdot s}$.

### 5.4.3 Horizontal Deflection Trace

Figure 5.7 illustrates the displacement signal in horizontal direction. It shows approximately two oscillations with a peak-to-peak deflection of about one pixel (corresponding to 15.6 µm) and a transversal mode growth of about 1.2 pixel from 6.8 pixel to 8 pixel. The comparison with the vertical deflection

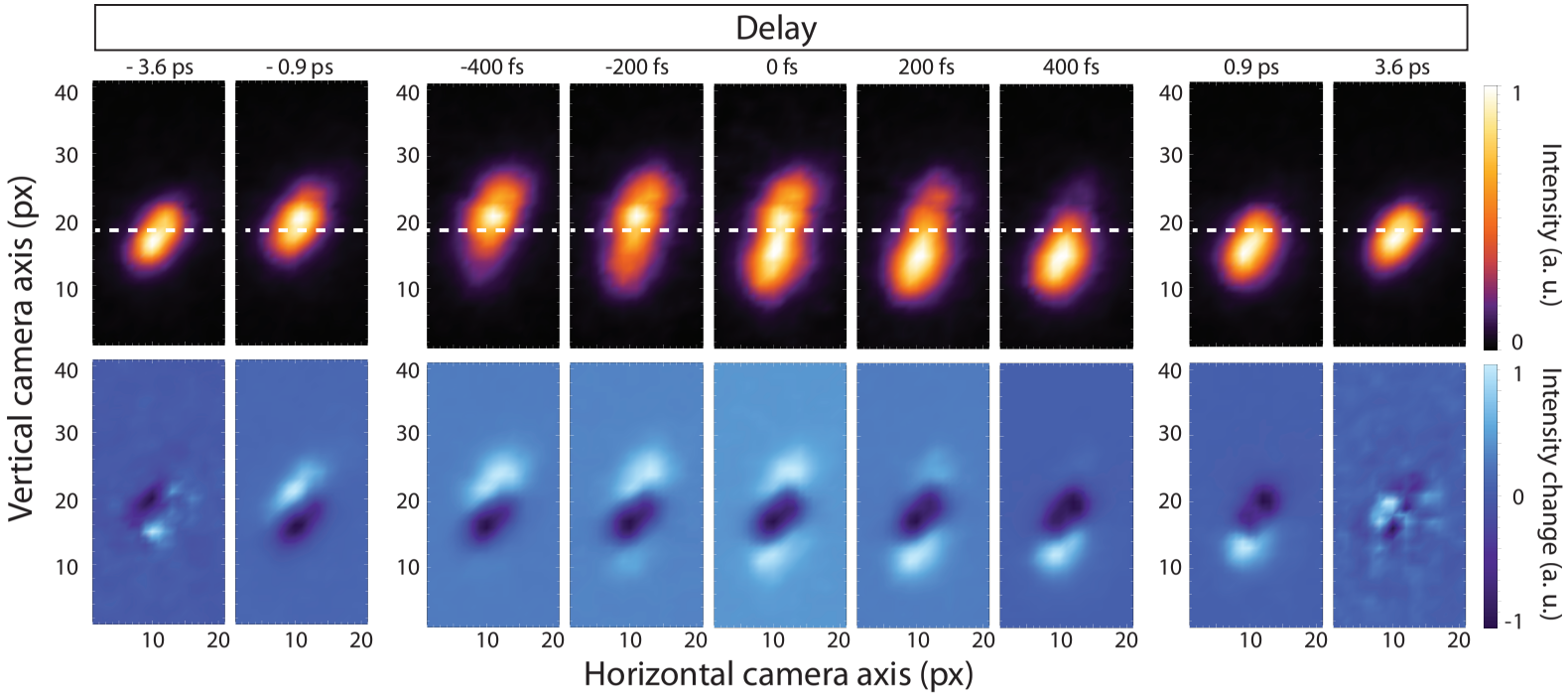


Figure 5.5: Electron beam displacement caused by THz-field. Deflection of the electron beam detected on the camera (upper row) and the corresponding difference image (lower row). Bright and dark areas indicate increased and reduced count rates, respectively. From -400 fs to +400 fs the deflection changes its sign, indicating an electron pulse duration of approximately 800 fs.

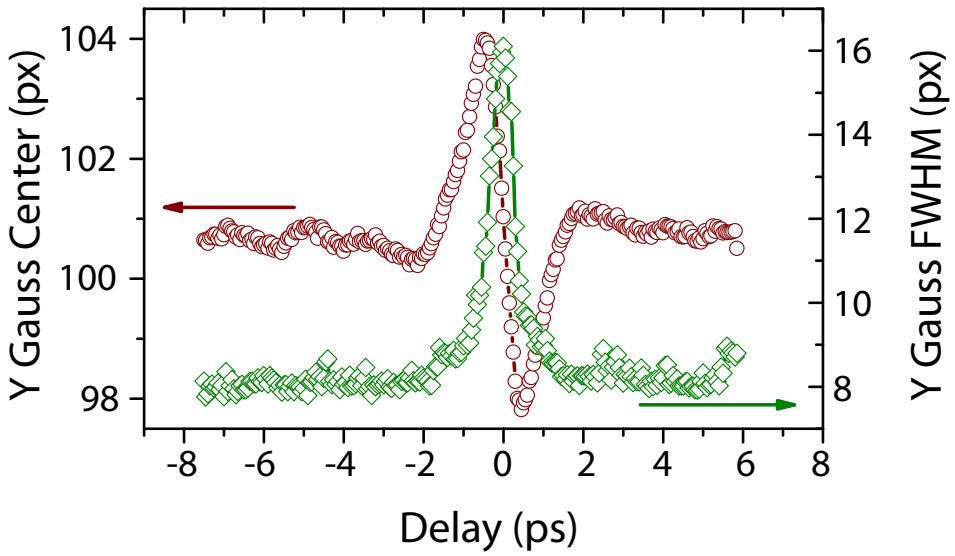


Figure 5.6: Sampled vertical deflection trace (center of a Gaussian fit) and the vertical width (FWHM) of an electron beam focused at the screen. A peak-to-peak deflection of about 6 pixels (94 µm) was obtained, the beam width was stretched from about 8 pixels (125 µm) to 16 pixels (250 µm).

amplitude shows that the signal is only 0.17 times as large as the vertical deflection.

This displacement is not expected, since the deflection set-up was designed to provide a p-polarized THz streaking field at the thin-film, which would contribute to vertical deflection only. The horizontal deflection can originate from: slight misalignment of the THz beam leading to a small s-component at the foil; slightly elliptical THz pulse already generated in the $LiNbO_3$ crystal or due to oblique reflections.

Vertical and horizontal deflection components are decoupled from each other and can therefore be analysed independently. Furthermore, the horizontal component is considerably smaller in amplitude than the vertical component, so that it is negligible in following discussions.

### 5.4.4 Deflection Amplitude vs. THz Pulse Energy

The sideways momentum transferred to the electron depends linear on amplitude of the streaking field. The THz pulse energy depends quadratically

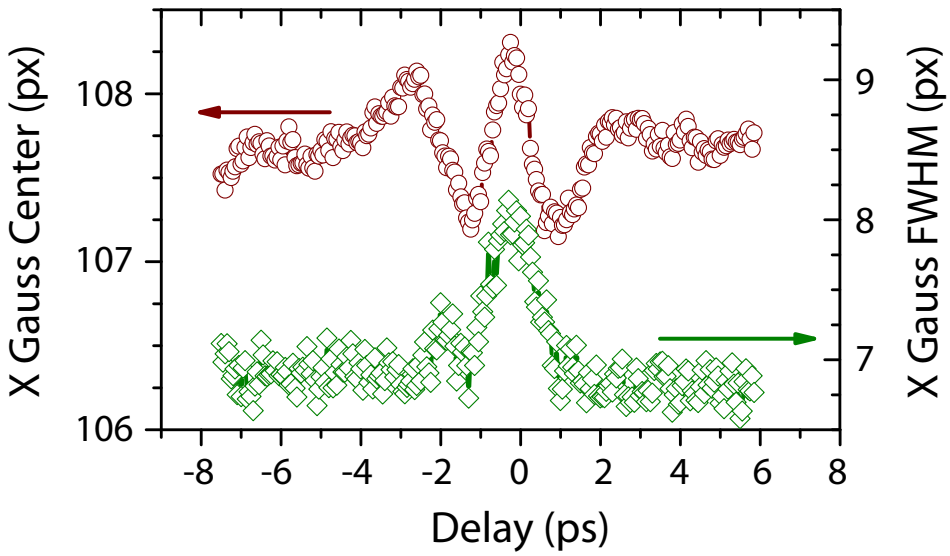


Figure 5.7: Sampled horizontal deflection trace (center of a Gaussian fit) and the horizontal width (FWHM) of an electron beam focused at the screen. A peak-to-peak deflection of about 1 pixel (15.6 µm) was observed, the beam width was stretched from 6.8 pixels (106 µm) to 8 pixels (125 µm).

on electric field amplitude. Therefore, the displacement amplitude should follow a square root function when increasing the THz pulse energy.

To proof this relation the deflection amplitude was recorded while the power of the infrared beam driving the THz generation process was varied. The energy of the generated THz pulses was then determined from the characteristic curve for THz generation, shown in figure 3.4.

Figure 5.8 illustrates the relation between measured peak-to-peak electron deflection and the applied THz pulse energy. The data was fitted with a square-root function, where the offset and shift were set to zero. It reveals the expected relation between the two quantities and thus confirms that the deflection purely originates from the THz field (and not from ponderomotive force or other envelope effects).

### 5.4.5 Experimental Stability of the Deflection Signal

The position of an electron beam spot is affected by a diversity of potential disturbances.

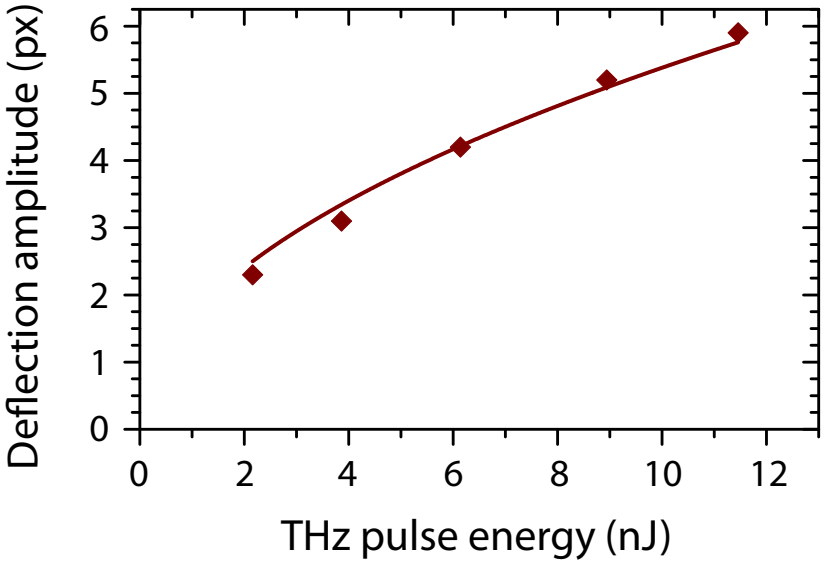


Figure 5.8: Peak-to-peak vertical deflection amplitude is plotted for different THz pulse energies. The continuous line is a least-square fit to the data with the function $f(x) = a\,x^b$. The obtained value $b = 0.57$ confirms the deflection to originate from the electromagnetic field.

**Timing jitter** On a short time scale, vibrations of optical components at acoustic frequencies can lead to a relative timing jitter between the streaking THz pulse and the electron pulse, which transfers into a deflection jitter. In the presented setup, both the THz pulse and the electron pulse are generated by the same source and are therefore optically synchronized. The relative timing jitter between them is estimated to be below 10 fs and thus significantly smaller than the period of the streaking pulse. Its influence is therefore negligible here.

**Amplitude jitter** Another source for jitter on a short time scale is the energy fluctuation of the laser pulses, which drive the optical rectification process for THz pulse generation. The relative peak-to-peak energy fluctuations of the laser pulses are below 5 %[3]. Since the optical rectification is a nonlinear process of second order, the THz field amplitude depends linearly on laser intensity or pulse energy. The maximum relative fluctuation

[3]This corresponds to fluctuations in field amplitude of less than 2.5%.

of the THz streaking field is therefore estimated to about 5 %, which could be transferred into fluctuation of the deflection amplitude.

Figure 5.9 addresses the question about the jitter of the displacement signal occurring in the measurement. Several deflection traces were taken subsequently with identical conditions. The traces were sampled with a resolution of 50 fs over a total delay range of about 15 ps, so that each trace consists of in total 300 points. The peak-to-peak deflection amplitude was here reduced to 4 pixel as a consequence of reduced infrared pump power used for THz generation in this experiment. The integration time of one second led to a recording time of about five seconds, so that approximately 25 minutes were required to record one trace.

The deflection signal of individual scans jittered in amplitude by less than 0.5 pixel, corresponding to a relative deviation of about 12 %. The beam width showed a jitter of about 0.5 pixel, corresponding to a relative deviation of about 6 %. The jitter was observed for the non-displaced electron beam as well, indicating a predominant contribution from the electron beam. The signal jitter can be improved by increasing statistics on the measurement. However, for the here intended electron pulse characterization the jitter amplitude is negligible.

On a longer time scale temperature drifts, accumulating electrostatic charges or fluctuations in external electric and magnetic fields can also cause some beam displacements. These effects are not considered here, because they take place on a longer time scale compared to the experiment (temperature drifts, electrostatic charges) or can be actively compensated for (external fields).

### 5.4.6 Deflectogram and Electron Pulse Characterization

Andrey Ryabov and Peter Baum implemented a procedure intended for the temporal and spatial analysis of electromagnetic fields enhanced in microstructures. It is based on comparison of experimentally obtained and calculated deflectograms. This code is used here to analyse the deflection at a thin metal film.

A deflectogram is a time-resolved plot of the normalized vertical electron beam profile (total counts registered in each row of the cameras pixel array) versus THz-electron delay time. An experimental deflectogram is shown in the upper plot of figure 5.10.

The deflectogram simulation takes place in several steps. The starting point is a guess of a time-dependent momentum-change function, resembling

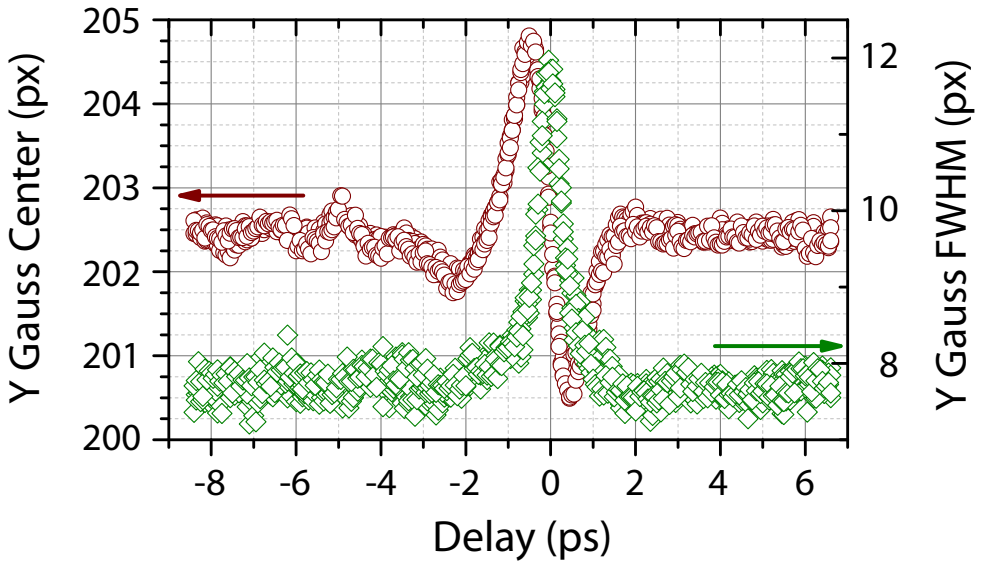


Figure 5.9: Stability of the deflection signal. Vertical deflection signal taken in three subsequent scans under the same conditions. An amplitude fluctuation of less than 0.5 pixel (7.8 µm) was observed. The fluctuation in beam width was below 1 pixel (15.6 µm)

the THz field shape. For that purpose, the experimentally sampled beam position (defined by the center of mass or the center of a Gaussian fit) is interpolated by a B-spline function. For each delay step, the resulting displacement function is convoluted with a Gaussian function, which describes the electron pulse in time. The result can be interpreted as a displacement weighted with temporal electron probability. This weighted displacement is then convoluted with the unaffected measured, vertical electron beam profile over the full duration of the electron pulse and is subsequently normalized. The result is a predicted position and shape of the vertical beam profile for each delay step. The deflectogram is then constructed by plotting this transversal mode over the delay. The last step is a numerical optimazation with respect to the experimentally obtained deflectogram solving the nonlinear least- squares problem with a Levenberg-Marquardt algorithm, by using the spline points and the electron pulse duration as parameters . The simulated deflectogram is shown in the lower plot of figure 5.10.

By comparison of experimental and simulated deflectrograms an electron pulse duration of about 800 fs was obtained. Visible differences between the

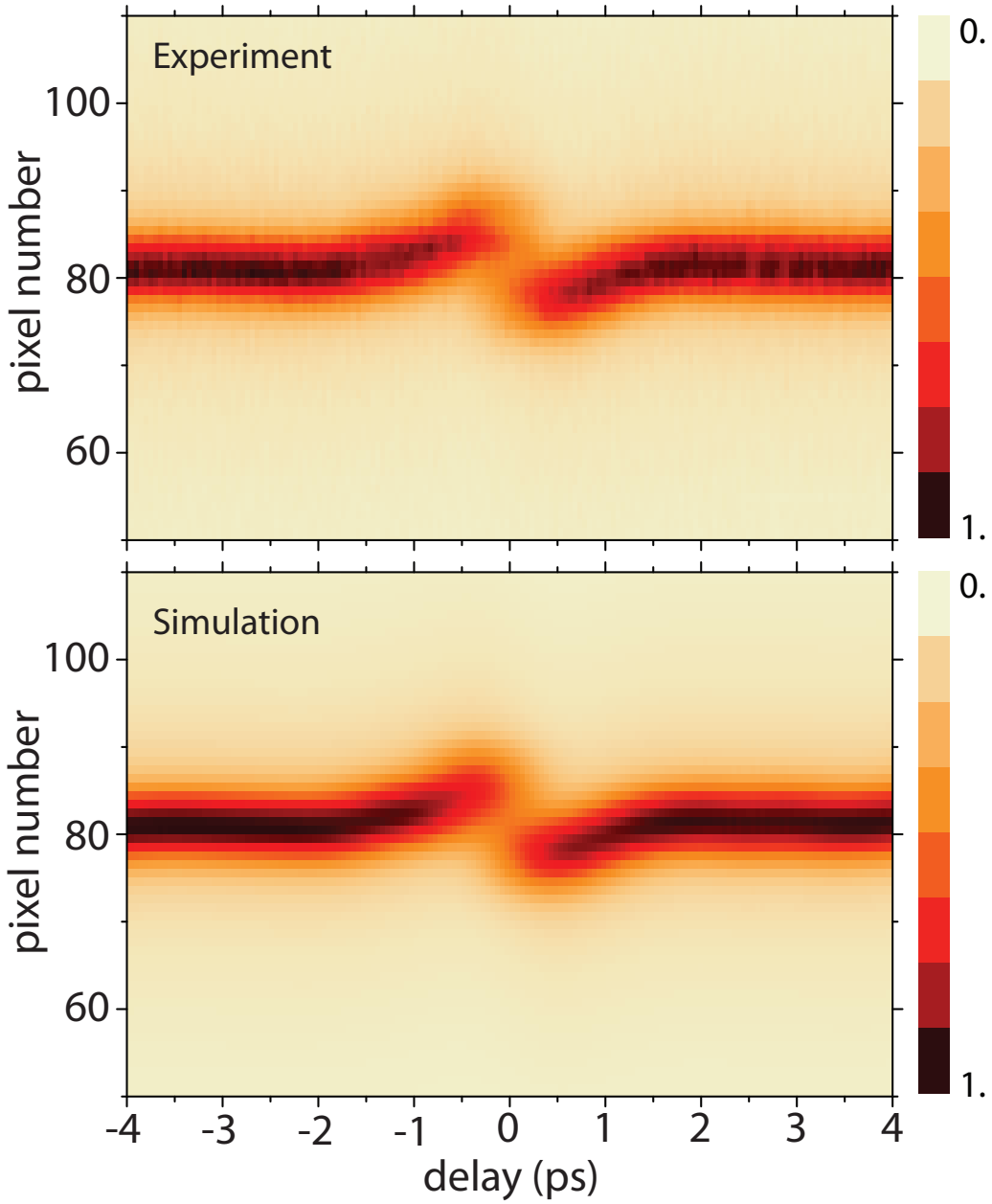


Figure 5.10: Deflectograms for electron pulse characterization. The comparison of experimental (a) and simulated (b) deflectogram allowed to estimate the electron pulse duration, which was determined to 800 fs ($\pm$ 200 fs).

deflectograms were observed for simulated 600-fs and 1000-fs pulses. Repeat-

ing the analysis with five different data sets showed comparable results, so that it is experimentally proven the electron pulse duration to be certainly within this interval. This result is also in agreement with the estimated value of 830 fs, see chapter A.

### 5.4.7 Temporal Resolution of the THz Streak Camera

This measurement represents, to our best knowledge, the first THz-driven streak camera. Having successfully determined the electron pulse duration, the question arises about the factors, which influence the temporal resolution. This section points out the relevant parameters and compares their values to those of conventional streak cameras.

Usually, the resolution of a conventional streak camera is analysed with respect to the measured optical pulse. In this point of view, several factors influence the temporal resolution of the device. In general, they can be assigned to the ability of the system to replicate and maintain the temporal structure of the measured pulse (i.e. how well matches the photo-electron pulse shape that of the original optical pulse) and the spatial resolution of the imaging system. The former is determined by the transit time dispersion $\tau_\mathrm{a}$ and the deflection dispersion $\tau_\mathrm{d}$, whereas the latter are influenced by the timing jitter $\tau_\mathrm{j}$ and the technical resolution $\tau_\mathrm{t}$.

**Transit time dispersion:** Originating from the initial energy spread of released electrons at the cathode, the transit time dispersion broadens the pulse during the propagation towards the interaction region, especially at the acceleration section between the cathode and the anode. It thus determines the smallest time-separation of two electron pulses which still can be resolved. However, it has no influence on the measurement of the electron pulse duration itself. The transit time dispersion is estimated to reach about 136 fs in a conventional streak camera [116].

As specified in subsection 5.4.6, the electron pulse duration at the foil is around 800 fs. The comparatively long duration is caused by rather long optical pulse duration of about 700 fs with not optimized spectral bandwidth and the currently limited acceleration field. Both parameter can be improved by appropriate technical measures. Using optimized optical excitation pulses at the cathode [117] current energy spread of about 0.3 eV (full width at half maximum) would reduce to approximately 0.1 eV. And scaling up the acceleration field, currently limited by occurrence of breakthroughs to 4 kV/mm, towards the achievable 13 kV/mm [116] would further reduce the dispersion. With these improvements the transit time dispersion is estimated to reach

140 fs being well comparable to the value achieved in the conventional streak camera.

**Deflection dispersion:** Deflection dispersion $\tau_d$ originates from finite transverse size of the electron beam and the transverse variation of the streaking field. The field inhomogeneity at the ends of the deflection plates produces transversally varying field components in propagation direction. The resulting longitudinal electron acceleration causes tilted electron pulses, and thus effectively a longer pulse duration. The deflection dispersion of a conventional streak camera amounts to about 50 fs [116]. In case of the THz-streak camera, the velocity matching condition ensures in a good approximation a transversally independent electron-field-interaction. The effective deflection length is about half THz-wavelength ($\lambda_{\mathrm{THz}} = 1\,\mathrm{mm}$) in contrast to the deflection length of about 5 cm in conventional streak cameras. The deflection dispersion is therefore negligible in the THz driven setup.

**Timing jitter:** The timing jitter $\tau_j$ between the electron pulse and the streaking field transfers into a jittering of the electron spot on the camera. At signal accumulation over many pulses, the timing jitter effectively blurs the electron image. To our best knowledge, the smallest timing jitter specified in the literature for a conventional streak camera is about 50 fs [118]. The timing jitter of the THz streak camera is estimated to be at least one order of magnitude smaller, thanks to the all-optical synchronization of the THz and electron generation processes.

**Technical resolution:** The entrance-slit limited resolution $\tau_t$, also called the technical resolution, is determined by the streaking speed $V$ and the static image width $\Delta X$ as $\tau_{\mathrm{t}} = \Delta X/V$, where the image width usually is specified as full-width-of-half-maximum. To resolve two electron pulses at the imaging detector they need to be separated by a distance of at least one beam width on the screen. Technical resolution can therefore be interpreted as the shortest temporal separation of two pulses that still can be resolved on the imaging detector. For a given streaking speed, this value can be improved by minimizing the image width on the detector, ideally until it matches the resolution of the camera. Conventional streak cameras incorporate an entrance slit in front of the focusing lens to minimize aberrations in the beam and to reduce the image size on the camera. With a slit width of 5 µm a static image width of 77 µm was achieved [116]. Thus providing a streaking speed of about 0.84 µm/fs, the technical resolution of a conventional streak camera was estimated to be close to 92 fs [116].

Currently, the THz-driven streak camera has a streaking speed of approximately 0.16 µm/fs and a beam width of around 120 µm, resulting in a technical resolution of about 750 fs. With an entrance slit a beam width of about 15 µm is feasible, which would directly improve the technical resolution to about 94 fs, a value well comparable to that of a state-of-the-art streak camera.

Summarizing the analysis one can state, that the THz-driven streak camera represents a qualitative advancement of the streaking technique by significantly reducing the timing jitter and virtually eliminating the deflection dispersion. However, the genuine advantage of the THz streak camera over conventional streak cameras lies in its huge potential for further scalability. The incident THz field can be enhanced by micro-structures, resulting in a two orders of magnitude larger deflection. Additionally, THz incident fields can be increased by three orders of magnitude [119] and electron beams at 90 keV can have diameters of a few micrometers [50]. Provided shorter electron pulses, the concept could be directly transferred towards higher frequencies where more powerful laser sources are available. With this multitude of options, it is reasonable to expect an increase of the streaking speed by orders-of-magnitude in the near future.

## 5.5 Perspectives

The present work has demonstrated the feasibility of electron deflection by optically generated THz fields. The effect is based on momentum exchange between the electromagnetic field and the electron pulse at a thin metal film. Further investigations revealed a direct electron-field interaction, in opposite to the interaction based on the ponderomotive force. Simulations showed the interaction to be dominated by a propagating interference wave which is created at the film due to superposition of incident and reflected parts of the single-cycle THz pulse. The magnetic field components were found to have significant contributions in the interaction process. The relative motion of the interference wave with respect to the propagating electron pulse leads to a sub-cycle interaction.

The investigated effect has allowed for characterization of currently available electron pulses ($\approx$ 800 fs) and is suitable for few-femtosecond pulses as well, which could so far not be easily measured. Its application in an electron compression setup will therefore enable the realization of few-femtosecond single electron pulses and thus pave the way for the implementation of an ultrafast electron diffraction experiment with few-femtosecond temporal and atomic-scale spatial resolution at the same time. Ultrafast electron diffrac-

tion will thus provide a four-dimensional visualization of the fastest possible atomic motion in space and time, in order to illuminate fundamental physics of light-matter interaction.

# Appendix A

# Dispersion of Single-Electron Pulses

Electron pulses analyzed in this work are generated with an electron gun [117] designed by Peter Baum and Daniel Kreier. A detailed description of this apparatus is given in the thesis [50]. A simplified scheme of the electron gun is depicted in figure A.1. Frequency doubled laser pulses hit the 20-nm thin gold layer deposited on the back side of a transparent substrate (fused silica or sapphire) and release free electrons by photo-electric effect. A static electric field $E_{\mathrm{acc}}$ applied between the cathode (gold layer) and an anode accelerates the electrons to a kinetic energy of 90 keV, which corresponds to approximately half the vacuum speed of light. This chapter gives a brief overview and presents important results needed to estimate the duration of free electron pulses.

The intensity of the laser beam is adjusted to generate approximately one electron each time an optical pulse hits the cathode and thus to avoid Coulomb repulsion between electrons within a pulse. The time when an electron is generated is not exactly determined but has a certain statistical distribution around the arriving time of the exciting laser pulse. This statistical distribution is termed electron pulse duration. It is determined by two effects [120]. Firstly, the electron generation takes place within the duration of the exciting laser pulse envelope $\tau_{\mathrm{laser}}$. Secondly, the initial kinetic energy of the electrons exhibits a statistical distribution $\Delta E$ originating from the mismatch between the cathode's work function and the energy of exciting photons. This energy distribution is causing beam divergence and temporal pulse broadening during the acceleration process $\tau_{\mathrm{acc}}$. Quantitatively, the final electron pulse duration $\tau_{\mathrm{electron}}$ is considered as a convolution of these

two parameters [120]

$$\tau_{\text{electron}} \approx \sqrt{\tau_{\text{laser}}^2 + \tau_{\text{acc}}^2} \tag{A.1}$$

where the duration of the (Gaussian-shaped) laser pulse and the temporal pulse broadening during acceleration are given by:

$$\tau_{\text{laser}} \approx 0.44 \frac{2\pi\hbar}{\Delta E} \quad \text{and} \tag{A.2}$$

$$\tau_{\text{acc}} \approx \frac{\left(\sqrt{2}m\right)^{1/2}}{eE_{\text{acc}}} \sqrt{\Delta E}, \tag{A.3}$$

with $e$ and $m$ representing elementary charge and electron mass, respectively.

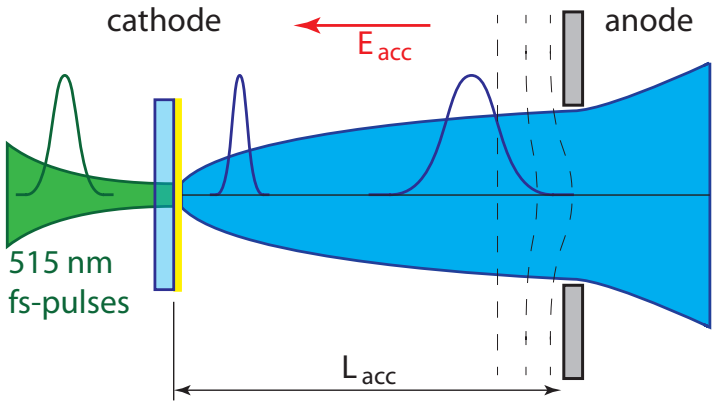


Figure A.1: Schematic representation of an electron gun. Optical pulses centred at 515 nm release electron pulses from a gold cathode by the photoelectric effect. Electron pulses are subsequently accelerated towards the anode in the constant electric field. Initial energy spread causes spatial divergence and temporal dispersion of the propagating electrons.

In the experiment, the full-width-of-half-maximum spread in kinetic energy amounts to 0.3 eV [1]. The free electron excitation duration reduces due to two subsequent two-photon processes (second-harmonic generation and two-photon photo-emission) approximately to the half of the fundamental laser pulse duration and is therefore approximately 500 fs. Using these values the final electron pulse duration after the acceleration process is approximated by equations A.1 - A.3 to about 830 fs. In the absence of space-charge, this pulse duration is preserved for the rest of the beam propagation.

[1] by private communications with Katherine Kealhofer

The duration of free single-electron pulses can be significantly shortened by reducing the energy mismatch between the exciting photons and the cathode's work function, by using shorter excitation pulses and by increasing the acceleration field strength. The latter is technologically challenging, but the remaining two options can be implemented using a broadband, tunable laser source like the noncolinear optical parametric amplifier [117]. Here, however, for the sake of simplicity the electron generation process has been restricted to the 1030-nm four-photon process.

# Appendix B

# Optics Letters, 39(23), p. 6604, (reprint)

# 800-fs, 330-μJ pulses from a 100-W regenerative Yb:YAG thin-disk amplifier at 300 kHz and THz generation in $LiNbO_3$

**W. Schneider,[1,2] A. Ryabov,[1,2] Cs. Lombosi,[3] T. Metzger,[4] Zs. Major,[1,2] J. A. Fülöp,[5,6] and P. Baum[1,2,*]**

[1]*Ludwig-Maximilians-Universität München, Am Coulombwall 1, 85748 Garching, Germany*

[2]*Max-Planck-Institute of Quantum Optics, Hans-Kopfermann-Str. 1, 85748 Garching, Germany*

[3]*Institute of Physics and Szentágothai Research Centre, University of Pécs, Ifjúság ú. 6 and 20, 7624 Pécs, Hungary*

[4]*TRUMPF Scientific Lasers GmbH + Co. KG, Feringastr. 10a, 85774 Unterföhring, Germany*

[5]*MTA-PTE High-Field Terahertz Research Group, Ifjúság ú. 6, 7624 Pécs, Hungary*

[6]*ELI-ALPS, ELI-Hu Nkft., Dugonics tér 13, 6720 Szeged, Hungary*

**Corresponding author: peter.baum@lmu.de*

Received September 5, 2014; revised October 15, 2014; accepted October 17, 2014;
posted October 20, 2014 (Doc. ID 222516); published November 18, 2014

Yb:YAG thin-disk lasers offer extraordinary output power, but systems delivering femtosecond pulses at a repetition rate of hundreds of kilohertz are scarce, even though this regime is ideal for ultrafast electron diffraction, coincidence imaging, attosecond science, and terahertz (THz) spectroscopy. Here we describe a regenerative Yb:YAG amplifier based on thin-disk technology, producing 800-fs pulses at a repetition rate adjustable between 50 and 400 kHz. The key design elements are a short regenerative cavity and fast-switching Pockels cell. The average output power is 130 W before the compressor and 100 W after compression, which at 300 kHz corresponds to pulse energies of 430 and 330 μJ, respectively. This is sufficient for a wide range of nonlinear conversions and broadening/compression schemes. As a first application, we use optical rectification in $LiNbO_3$ to produce 30-nJ single-cycle THz pulses with 6 W pump power. The electric field exceeds 10 kV/cm at a central frequency of 0.3 THz, suitable for driving structural dynamics or controlling electron beams. 

*OCIS codes:* (140.7090) Ultrafast lasers; (160.3730) Lithium niobate; (190.7110) Ultrafast nonlinear optics.
http://dx.doi.org/10.1364/OL.39.006604

Femtosecond lasers are indispensable in many fields of science and technology. While Ti:sapphire-based sources typically produce the shortest pulses, there is a recent paradigm shift to Yb:YAG technology [1], offering significantly higher output power and scalability, especially in geometries with thin disks, slabs, or fibers. Reported Yb:YAG-based lasers producing femtosecond pulses (<1 ps) can be sorted into mode-locked oscillators [2,3], fiber lasers [4,5], long-cavity oscillators [6–8], slab amplifiers [9,10], disk amplifiers [11,12], or cascaded laser chains for pulses in the multi-mJ regime [13–18].

Many applications require repetition rates between 100 kHz and 1 MHz. This intermediate regime between oscillators and conventional amplifiers is unusual, but beneficial in pump-probe spectroscopy, material processing, attosecond science, or coincidence imaging, for improving the signal-to-noise ratio, enhancing the total flux or reducing acquisition times. Our particular case is ultrafast electron diffraction with single-electron pulses [19,20] for probing structural dynamics with atomic resolution in space and time [21]. An optimum repetition rate is 200–300 kHz [22]; yet the laser pulses should be powerful enough (hundreds of μJ) for effective nonlinear optical frequency conversions to the ultraviolet/visible/infrared [23,24] and THz domains [25,26], in order to initiate and control atomic-scale dynamics.

None of the Yb:YAG-based laser systems demonstrated so far (fiber, slab, crystal, disk) [1], provide sufficiently intense and stable femtosecond pulses at hundreds of kHz for these diffraction applications, which require maximum simplicity of the laser system. Hence, we describe here the design and operation of a regenerative Yb:YAG amplifier based on thin-disk technology, producing 800-fs pulses at an adjustable repetition rate between 50 and 400 kHz.

Figure 1 depicts the experiment, based on a preliminary attempt [27]. The seed (t-Pulse 50, Amplitude Systèmes) is a mode-locked Yb:YAG oscillator with a repetition rate of 50 MHz at a central wavelength of 1030 nm, delivering fs pulses with an energy of ~40 nJ and a spectral bandwidth of 2.7 nm. These pulses propagate through transmission gratings with 1,400 lines per mm and $f = 1\,\mathrm{m}$ lenses, producing a group-velocity dispersion of 27 $\mathrm{ps}^2$ and ~160-ps pulses for chirped-pulse amplification.

The desired high repetition rate in the multi-hundred-kHz regime together with the thin-disk's limited gain per reflection of ~10% puts some significant constraints on

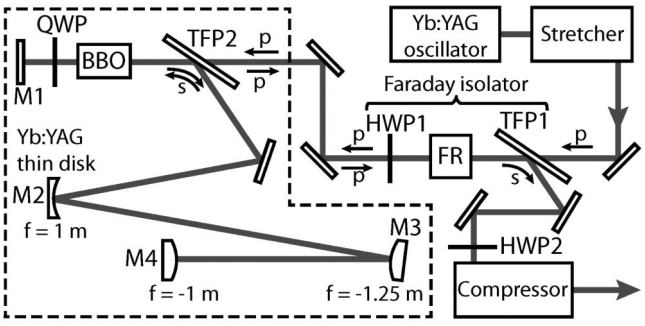


Fig. 1. Experimental setup and optical layout of the regenerative amplifier. TFP, thin-film polarizer; FR, Faraday rotator; HWP, half-wave plate; BBO, Pockels cell, QWP, quarter-wave plate; M1–M4, mirrors. The regenerative amplifier cavity is marked with a dashed line. Arrows denote the polarization state.

 

the regenerative cavity. Each amplified pulse must leave the cavity before the next seed pulse can enter. For a design at $\nu_{rep} = 400$ kHz and 10% gain, we estimate that $N_{gain} \approx 200$ round trips are required. Hence the maximum cavity length is $c/(2\nu_{rep}N_{gain}) \approx 1.9$ m and the switching time for coupling the pulses in and out must be shorter than $1/(\nu_{rep}N_{gain}) \approx 12$ ns. This necessitates a small Pockels cell crystal to minimize the high voltage required for switching. In turn, the cavity mode must be designed small enough to avoid clipping and damage, but also large enough to minimize B-integral accumulation.

Our design is depicted in Fig. 1 within the dashed outline. The disk module (TRUMPF) employs a ~1/10-mm-thick, ~10%-doped Yb:YAG thin-disk on a water-cooled heat sink, pumped by laser diodes at ~940 nm (LDM 500, Laserline GmbH). The disk has a radius of curvature of $r \approx 2$ m (M2). In order to comply with the considerations above, we use two convex mirrors (M3, M4) and a total cavity length of 1670 mm. The cavity's stability is calculated using ray transfer matrices (see Fig. 2). The beam diameter in the Pockels cell is <1.5 mm (full width at half-maximum), and the accumulated B-integral is ~0.05. The Pockels cell is an anti-reflection-coated BBO crystal with a size of 6 mm × 6 mm × 25 mm, driven with a rise time of ~6 ns by a pulsed high-voltage supply (Bergmann KG). Hence we conform to all considerations outlined above.

A mode-matching telescope is used to couple in the seed pulses with a typical switching sequence [28]: a thin-film polarizer (TFP-1), Faraday rotator (FR), and half-wave plate (HWP) form an isolator. P-polarized incoming pulses enter the amplifier cavity through a thin-film polarizer (TFP-2). The Pockels cell (BBO) is in its "off" switching state, and a double-pass through a quarter-wave plate (QWP) produces back-propagating pulses with s-polarization, which are reflected by TPF-2. Before their return from mirror M4, the Pockels cell is switched "on", rotating polarization by 45° and rendering the QWP ineffective. S-polarized pulses are therefore captured in the amplifier cavity until the Pockels cell is switched "off" again. The QWP produces p-polarization, and the pulses leave the cavity through TFP-2. The Faraday isolator directs them toward compression and applications.

In the following, we applied 120 round trips at 300 kHz before coupling the final pulse out of the amplifier cavity. More round trips could destroy the Pockels cell, as described in more detail below. Figure 3(a) shows the increase of output power with increasing pump power. Ellipticity, observed after the end mirror M1, increases

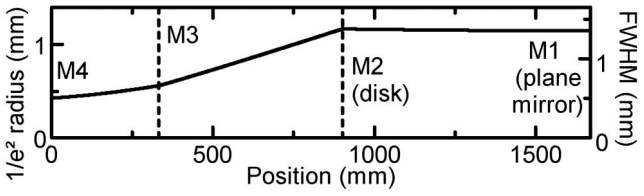


Fig. 2. Design of the length-limited amplifier cavity (dashed area in Fig. 1) for operation at high repetition rates up to 400 kHz. Solid, beam diameter along the cavity mode; dashed, position of mirrors M2 and M3. FWHM, full width at half-maximum.

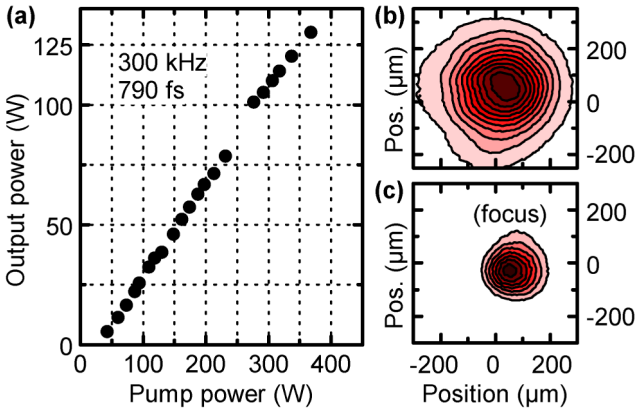


Fig. 3. Output performance. (a) Output power in dependence of the pump power. (b) Beam profile after a focus. (c) Shape of a focused spot. Intensity of the beam profiles is normalized.

slightly from 0.95 at low power up to 0.8 at above 100 W of output. Nevertheless, the cavity is always stable. At 370 W of pump power, we achieve an output power of 130 W before the compressor. This corresponds to a pulse energy of 430 μJ. Figures 3(b) and 3(c) show the beam profiles at 130 W measured after the focus and in the focus of an $f = 450$ mm lens, respectively. The measured $M^2$ value at an output of 130 W is 1.30 and 1.35 for the horizontal and the vertical directions, respectively.

Compression of the 130-W output pulses is achieved using two reflective gratings with 1400 lines per mm at a separation of 1.76 m; the angle of incidence is 47°. The throughput of this compressor amounts to 77%; ~100 W are emitted for applications. Figure 4 shows the spectrum and autocorrelation trace (pulseCheck, APE GmbH). With respect to the seed spectrum with a width of 2.7 nm, the amplified spectrum shows signs of gain narrowing and a width of 2.3 nm. Still, the Fourier limit calculated from the measured spectrum is 740 fs. There is no evidence for self-phase modulation or any other nonlinear processes; the slight wiggles are interferences at the spectrometer's fiber entrance. The autocorrelation trace indicates compressed pulses of 790 fs duration, assuming a $\mathrm{sech}^2$ shape. This is within 7% of the Fourier limit and indicates a good match between stretcher, intra-cavity dispersion, and compressor in our system. Higher order chirp, as can occur from self-phase modulation, is negligible.

The output power is stable to about 1% rms on the subminute time scale. On longer time scales, there are some systematic oscillations of ±2% (peak-to-peak) caused by

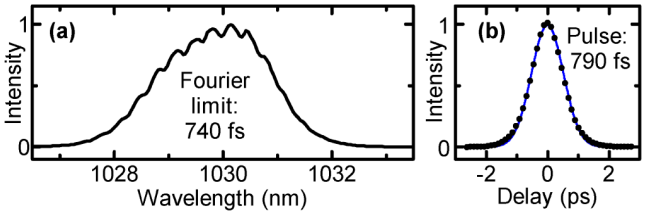


Fig. 4. Regenerative amplifier performance in the frequency and time domains. (a) Output spectrum. (b) Autocorrelation trace (black dots), fitted assuming a $\mathrm{sech}^2$-shaped temporal pulse profile (blue line). The pulse duration (790 fs) is close to the measured spectrum's Fourier limit (740 fs).

the disk's chiller system, which is currently only stable to ±1 K. The laser reliably runs over several days without alignment; no significant drifts of output power are observable (<0.8% over a day, <0.05% per hour).

We note in Fig. 3(a) the almost linear relation; we do not reach saturation. This suggests that we could further increase the pump power or the number of round trips and achieve even higher output and stability. In practice, however, this is limited by Pockels cell damage, occurring either at the front or back surface as an extended dark region around the center, where the beam passes through. We attribute this damage to the effects of average intra-cavity power in conjunction with coating imperfections. One solution would be to obtain better-coated crystals, which is technologically challenging. An alternative would be to redesign the cavity for a slightly larger mode at the Pockels cell crystal, accepting some minor clipping. There is also room for moderate lengthening of the cavity, especially if more intense seed pulses are applied at a reduced number of round trips. In view of these options, and potentially others, it might be possible to further scale our 300-kHz regenerative disk amplifier concept toward higher output powers, in case this should be desirable.

As a first application, we produced THz radiation by optical rectification in 0.6% MgO-doped stoichiometric lithium niobate ($LiNbO_3$) using tilted-pulse-front pumping [29]. For safety, in order to avoid excessive average powers, we reduced the laser's repetition rate to 50 kHz for these experiments. Tilted pulses were generated with a 400-lines-per-mm gold grating and an imaging lens with $f \approx 150$ mm placed at a distance of 1750 mm after the grating. The front surface of the $LiNbO_3$ crystal was placed 166 mm after the imaging lens. This produced a large demagnification ratio of about 1:10, which was necessary to compensate for the significantly different damage thresholds of the grating and the $LiNbO_3$ crystal, measured with our system at 300 kHz as ~0.7 GW/cm$^2$ and ~110 GW/cm$^2$ peak intensity, respectively. Crystal damage was probably due to heating and the related thermo-optic effect. We note that a demagnification of about 1:2 would have been ideal to minimize the imaging distortions [30], but this was not critical for our small excited area at the $LiNbO_3$ crystal (see below). Incidence and exit angles at the grating approximated the ideal case, minimizing temporal distortions [31].

The pump spot size at the position of the $LiNbO_3$ prism was 710 μm × 670 μm (horizontal × vertical, full width at half-maximum). Laser polarization was set with a half-wave plate along $LiNbO_3$'s $z$-axis, parallel to the axis of pulse-front tilt. The THz radiation from the prism's exit face, cut at 63°, was observed with a pyroelectric detector (Gentec-EO). With knife-edge scans, we determined the effective size of the THz-emitting area as 1560 μm × 670 μm (horizontal × vertical, full width at half-maximum). This is close to the expected value, considering the 63° emission angle. Using beam-profile scans at different distances, we determined the divergence of the THz radiation to 18° horizontally and 40° vertically (full width at half-maximum). This asymmetry and magnitude are expected from the elongated emission area with dimensions close to the THz wavelength. The input beam's cross-section could be shaped with cylindrical optics if a more round and uniformly divergent THz beam is required.

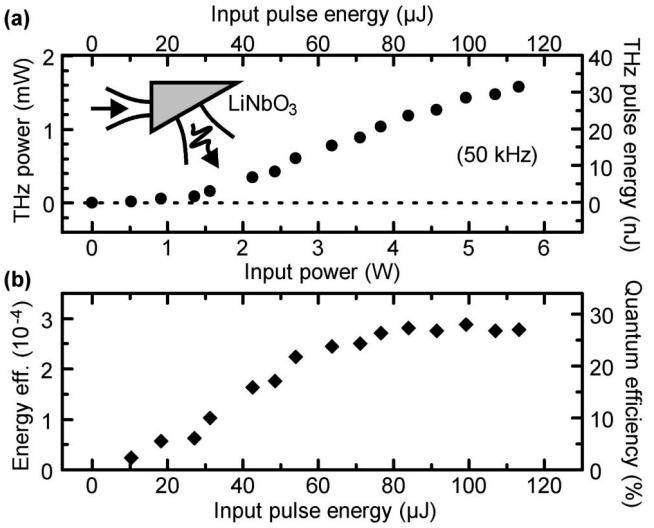


Fig. 5. Performance of the THz generation with tilted pulses in $LiNbO_3$. (a) Output power and THz pulse energy in dependence of the input power and pulse energy. (b) Quantum efficiency and energy-conversion efficiency.

The power of the emitted THz radiation (outside of $LiNbO_3$) versus the laser power (transmitted into $LiNbO_3$) is depicted in Fig. 5(a). At low energy, there is an almost quadratic dependence; at higher energy a more linear relation indicates the onset of saturation. We stopped this study at ~6 W pump power or 120 μJ pulse energy, in order not to risk damage of the $LiNbO_3$ prism, which was not cooled or specially mounted. Nevertheless, the measured THz output power was 1.6 mW. This corresponds to 30 nJ pulse energy, $2.8 \times 10^{-4}$ pump-to-THz conversion efficiency and close to 30% quantum efficiency. This efficiency, similar to earlier results [32], can be increased further by increasing the beam diameter in the horizontal direction to enable larger interaction length or by using shorter pump pulses [30,33], but pump-THz walk-off must be considered.

Electro-optical sampling in a 300-μm-thick GaP crystal revealed the time-dependent electric field of the THz pulses; see Fig. 6(a). The single-cycle pulse had a peak field strength of about 11 kV/cm, determined from the electro-optical coefficients of GaP [34]. The corresponding spectral amplitude is depicted in Fig. 6(b), revealing a center at 0.3 THz. These pulses have an attractive combination of repetition rate, field strengths and central

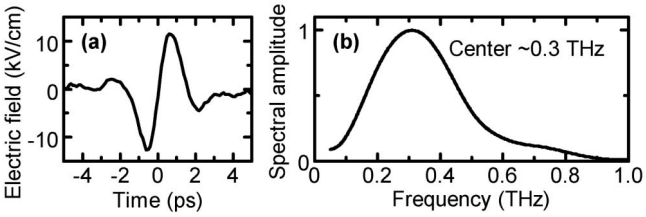


Fig. 6. Characterization of the THz pulses. (a) Time-dependent electric field of the THz pulses with peak strength of ~11 kV/cm. (b) THz spectrum at full output power (spectral amplitude).

frequency for driving structural motion in materials or for accelerating/controlling electron beams.

Assuming that the thermal load on the $LiNbO_3$ prism can be handled by appropriate cooling and mounting, which remains to be proven in the experiment, we can extrapolate our results to a scenario where our laser's full output power at 300 kHz is applied for THz generation. Referring to Fig. 5(b), we assume that the regime of constant quantum efficiency, i.e., linear energy scaling, continues beyond the 120 μJ applied so far. Using the full 330 μJ available at 300 kHz and 100 W, we would then obtain a THz output power of about 25 mW and about 85 nJ per pulse. Electric fields could be increased by tighter focusing or field enhancement at microstructures.

In conclusion, the here reported high-power Yb:YAG laser source produces femtosecond pulses with hundreds-of-μJ energy at an adjustable repetition rate of 50–300 kHz, probably up to 400 kHz if desirable. The peak power of the cycle-averaged intensity distribution of the 800-fs pulses is 400 MW. The pulses could be further shortened by driving the amplifier in the regime of self-phase modulation [11], by shaping the seed spectrum [15], by controlling the gain spectrum [28], or by nonlinear broadening/compression [35–37]. The ability to efficiently produce intense THz radiation at 50 kHz demonstrates the suitability of our thin-disk laser for advanced nonlinear frequency conversions at optimum repetition rates for ultrafast electron diffraction, attosecond/femtosecond spectroscopy, or coincidence imaging of molecular dynamics.

We acknowledge funding from ERC ("4D imaging"), from Munich-Centre of Advanced Photonics, from IMPRS of Advanced Photon Science, and from BMBF contract 13N12082. J. A. F. acknowledges support from János Bolyai Research Scholarship (Hungarian Academy of Sciences) and OTKA grants 101846 and 113083. We thank Roswitha Graf for her contributions at the initial stage of this project and J. Hebling for helpful discussion.

## References

1. H. Fattahi, H. G. Barros, M. Gorjan, T. Nubbemeyer, B. Alsaif, C. Y. Teisset, M. Schultze, S. Prinz, M. Haefner, M. Ueffing, A. Alismail, L. Vámos, A. Schwarz, O. Pronin, J. Brons, X. T. Geng, G. Arisholm, M. Ciappina, V. S. Yakovlev, D.-E. Kim, A. M. Azzeer, N. Karpowicz, D. Sutter, Z. Major, T. Metzger, and F. Krausz, Optica **1**, 45 (2014).
2. O. Pronin, J. Brons, C. Grasse, V. Pervak, G. Boehm, M.-C. Amann, V. L. Kalashnikov, A. Apolonski, and F. Krausz, Opt. Lett. **36**, 4746 (2011).
3. C. J. Saraceno, F. Emaury, O. H. Heckl, C. R. E. Baer, M. Hoffmann, C. Schriber, M. Golling, T. Suedmeyer, and U. Keller, Opt. Express **20**, 23535 (2012).
4. T. Eidam, S. Hanf, E. Seise, T. V. Andersen, T. Gabler, C. Wirth, T. Schreiber, J. Limpert, and A. Tünnermann, Opt. Lett. **35**, 94 (2010).
5. A. Klenke, S. Breitkopf, M. Kienel, T. Gottschall, T. Eidam, S. Haedrich, J. Rothhardt, J. Limpert, and A. Tuennermann, Opt. Lett. **38**, 2283 (2013).
6. S. V. Marchese, C. R. E. Baer, A. G. Engqvist, S. Hashimoto, D. J. H. C. Maas, M. Golling, T. Suedmeyer, and U. Keller, Opt. Express **16**, 6397 (2008).
7. D. Bauer, I. Zawischa, D. Sutter, A. Killi, and T. Dekorsy, Opt. Express **20**, 9698 (2012).
8. C. J. Saraceno, F. Emaury, C. Schriber, M. Hoffmann, M. Golling, T. Südmeyer, and U. Keller, Opt. Lett. **39**, 9 (2014).
9. P. Russbueldt, T. Mans, G. Rotarius, J. Weitenberg, H. D. Hoffmann, and R. Poprawe, Opt. Express **17**, 12230 (2009).
10. P. Russbueldt, T. Mans, J. Weitenberg, H. D. Hoffmann, and R. Poprawe, Opt. Lett. **35**, 4169 (2010).
11. R. Fleischhaker, R. Gebs, A. Budnicki, M. Wolf, J. Kleinbauer, and D. Sutter, in *Conference on Lasers and Electro-Optics Europe (CLEO)* (IEEE, 2013), p. 1.
12. C. Teisset, M. Schultze, R. Bessing, M. Haefner, S. Prinz, D. Sutter, and T. Metzger, in *Advanced Solid-State Lasers Congress Postdeadline* (Optical Society of America, 2013), paper JTh5A.1.
13. K.-H. Hong, J. T. Gopinath, D. Rand, A. M. Siddiqui, S.-W. Huang, E. Li, B. J. Eggleton, J. D. Hybl, T. Y. Fan, and F. X. Kärtner, Opt. Lett. **35**, 1752 (2010).
14. M. Schulz, R. Riedel, A. Willner, T. Mans, C. Schnitzler, P. Russbueldt, J. Dolkemeyer, E. Seise, T. Gottschall, S. Hadrich, S. Duesterer, H. Schlarb, J. Feldhaus, J. Limpert, B. Faatz, A. Tunnermann, J. Rossbach, M. Drescher, and F. Tavella, Opt. Lett. **36**, 2456 (2011).
15. S. Klingebiel, C. Wandt, C. Skrobol, I. Ahmad, S. A. Trushin, Z. Major, F. Krausz, and S. Karsch, Opt. Express **19**, 5357 (2011).
16. M. Schulz, R. Riedel, A. Willner, S. Düsterer, M. J. Prandolini, J. Feldhaus, B. Faatz, J. Rossbach, M. Drescher, and F. Tavella, Opt. Express **20**, 5038 (2012).
17. J.-P. Negel, A. Voss, M. A. Ahmed, D. Bauer, D. Sutter, A. Killi, and T. Graf, Opt. Lett. **38**, 5442 (2013).
18. J. Tuemmler, R. Jung, H. Stiel, P. V. Nickles, and W. Sandner, Opt. Lett. **34**, 1378 (2009).
19. A. H. Zewail, Science **328**, 187 (2010).
20. P. Baum, Chem. Phys. **423**, 55 (2013).
21. P. Baum, J. Phys. B **47**, 124005 (2014).
22. S. Lahme, C. Kealhofer, F. Krausz, and P. Baum, Struct. Dyn. **1**, 034303 (2014).
23. C. Homann, C. Schriever, P. Baum, and E. Riedle, Opt. Express **16**, 5746 (2008).
24. M. Bradler, C. Homann, and E. Riedle, Appl. Phys. B **113**, 19 (2013).
25. J. Hebling, K.-L. Yeh, M. C. Hoffmann, and K. A. Nelson, IEEE J. Sel. Topics Quantum Electron. **14**, 345 (2008).
26. H. Hirori and K. Tanaka, IEEE J. Sel. Topics Quantum Electron **19**, 8401110 (2013).
27. R. Graf, T. Metzger, M. Chyla, D. Sutter, Z. Major, A. Apolonski, and F. Krausz, *Europhoton Conference* (2012), paper POSD.2.
28. W. Koechner, *Solid-State Laser Engineering* (Springer, 2006).
29. J. Hebling, G. Almasi, I. Z. Kozma, and J. Kuhl, Opt. Express **10**, 1161 (2002).
30. J. A. Fülöp, L. Palfalvi, G. Almasi, and J. Hebling, Opt. Express **18**, 12311 (2010).
31. D. Kreier and P. Baum, Opt. Lett. **37**, 2373 (2012).
32. M. C. Hoffmann, K.-L. Yeh, J. Hebling, and K. A. Nelson, Opt. Express **15**, 11706 (2007).
33. J. A. Fülöp, L. Palfalvi, M. C. Hoffmann, and J. Hebling, Opt. Express **19**, 15090 (2011).
34. X. C. Zhang and J. Xu, *Introduction to THz Wave Photonics* (Springer, 2010).
35. S. Haedrich, A. Klenke, A. Hoffmann, T. Eidam, T. Gottschall, J. Rothhardt, J. Limpert, and A. Tuennermann, Opt. Lett. **38**, 3866 (2013).
36. F. Emaury, C. F. Dutin, C. J. Saraceno, M. Trant, O. H. Heckl, Y. Y. Wang, C. Schriber, F. Gerome, T. Sudmeyer, F. Benabid, and U. Keller, Opt. Lett. **21**, 4986 (2013).
37. Y. Y. Wang, X. Peng, M. Alharbi, C. F. Dutin, T. D. Bradley, F. Gerome, M. Mielke, T. Booth, and F. Benabid, Opt. Lett. **37**, 3111 (2012).

# Appendix C

# Data Archiving

The experimental raw data, evaluation files, and original figures can be found on the Data Archive Server of the Laboratory for Attosecond Physics at the Max Planck Institute of Quantum Optics:
`/afs/rzg/mpq/lap/publication_archive`

The data is organized with respect to the chapters and sub-chapters in the thesis. All original figures are named `fig_xx-xx-text` where `xx-xx` corresponds to the figure number in the thesis and `-text` gives a short figure description. The editable figures and the corresponding evaluations or simulations are also provided. The file names or folders have the same number `xx-xx` as the figure. Supplementary information about data aquisition, processing, evaluation or simulation can be found in added text files.

# Bibliography


[1] W. Hittorf. "Ueber die Elektrizitätsleitung der Gase." *Erste Mitteilung. Ann. Phys. und Chemie*, vol. 136, pp. 1–31, 1869.

[2] J. J. Thomson. "Cathode Rays." *Philosophical Magazine*, vol. 44 (293), 1897.

[3] F. Braun. "Ueber ein Verfahren zur Demonstration und zum Studium des zeitlichen Verlaufes variabler Ströme." *Annalen der Physik*, vol. 296 (3), pp. 552–559, 1897.

[4] L. De Forest. "The Audion; A New Receiver for Wireless Telegraphy." *Transactions of the AIEE*, vol. 25, pp. 735–763, Jan. 1906.

[5] W. C. Röntgen. "Ueber eine neue Art von Strahlen." *Aus den Sitzungensberichten der Würzburger Physik.-medic. Gesellschaft*, vol., 1895.

[6] R. Burger. "Vorrichtung zur Erzeugung von Roentgenstrahlen." DE129974. Apr. 1902.

[7] T. Ishikawa et al. "A compact X-ray free-electron laser emitting in the sub-ångström region." *Nature Photonics*, vol. 6 (8), pp. 540–544, June 2012.

[8] J. Ullrich, A. Rudenko, and R. Moshammer. "Free-Electron Lasers: New Avenues in Molecular Physics and Photochemistry." *Annual Review of Physical Chemistry*, vol. 63 (1), pp. 635–660, May 2012.

[9] G. R. Neil. "Accelerator Sources for THz Science: A Review." *Journal of Infrared, Millimeter, and Terahertz Waves*, vol. 35 (1), pp. 5–16, Jan. 2014.

[10] S. J. Singer. "The Fluid Mosaic Model of the Structure of Cell Membranes." *Science*, vol. 175 (4023), pp. 720–731, 1972.

[11] R. Henderson, J. M. Baldwin, T. A. Ceska, F. Zemlin, E. Beckmann, and K. H. Downing. "Model for the structure of bacteriorhodopsin based on high-resolution electron cryo-microscopy." *Journal of molecular biology*, vol. 213 (4), pp. 899–929, 1990.

[12] S. Iijima. "Helical microtubules of graphitic carbon." *Nature*, vol. 354, pp. 56–58, 1991.

[13] C. B. Murray, D. J. Norris, and M. G. Bawendi. "Synthesis and characterization of nearly monodisperse CdE (E= S, Se, Te) semiconductor nanocrystallites." *Journal of the American Chemical Society*, vol. 115 (19), pp. 8706–8715, 1993.

[14] S. Klinge, F. Voigts-Hoffmann, M. Leibundgut, S. Arpagaus, and N. Ban. "Crystal structure of the eukaryotic 60S ribosomal subunit in complex with initiation factor 6." *Science*, vol. 334 (6058), pp. 941–948, 2011.

[15] A. H. Zewail. "Femtochemistry: Atomic-Scale Dynamics of the Chemical Bond †." *The Journal of Physical Chemistry A*, vol. 104 (24), pp. 5660–5694, June 2000.

[16] D. J. Flannigan and A. H. Zewail. "4D Electron Microscopy: Principles and Applications." *Accounts of Chemical Research*, vol. 45 (10), pp. 1828–1839, Oct. 2012.

[17] R. J. D. Miller. "Mapping Atomic Motions with Ultrabright Electrons: The Chemists' Gedanken Experiment Enters the Lab Frame." *Annual Review of Physical Chemistry*, vol. 65 (1), pp. 583–604, Apr. 2014.

[18] P. Baum. "On the physics of ultrashort single-electron pulses for time-resolved microscopy and diffraction." *Chemical Physics*, vol. 423, pp. 55–61, Sept. 2013.

[19] P. Baum. "Towards ultimate temporal and spatial resolutions with ultrafast single-electron diffraction." *Journal of Physics B: Atomic, Molecular and Optical Physics*, vol. 47 (12), p. 124005, June 2014.

[20] J. A. Valdmanis, R. L. Fork, and J. P. Gordon. "Generation of optical pulses as short as 27 femtoseconds directly from a laser balancing self-phase modulation, group-velocity dispersion, saturable absorption, and saturable gain." *Optics Letters*, vol. 10 (3), pp. 131–133, 1985.

[21] D. E. Spence, P. N. Kean, and W. Sibbett. "60-fsec pulse generation from a self-mode-locked Ti: sapphire laser." *Optics Letters*, vol. 16 (1), pp. 42–44, 1991.

[22] T. Brabec and F. Krausz. "Intense few-cycle laser fields: Frontiers of nonlinear optics." *Reviews of Modern Physics*, vol. 72 (2), p. 545, 2000.

[23] M. Drescher et al. "Time-resolved atomic inner-shell spectroscopy." *Nature*, vol. 419 (6909), pp. 803–807, 2002.

[24] M. F. Kling et al. "Control of electron localization in molecular dissociation." *Science*, vol. 312 (5771), pp. 246–248, 2006.

[25] A. L. Cavalieri et al. "Attosecond spectroscopy in condensed matter." *Nature*, vol. 449 (7165), pp. 1029–1032, Oct. 2007.

[26] M. Uiberacker et al. "Attosecond real-time observation of electron tunnelling in atoms." *Nature*, vol. 446 (7136), pp. 627–632, Apr. 2007.

[27] Ma. Schultze et al. "Delay in photoemission." *Science*, vol. 328 (5986), pp. 1658–1662, 2010.

[28] S. Zherebtsov et al. "Controlled near-field enhanced electron acceleration from dielectric nanospheres with intense few-cycle laser fields." *Nature Physics*, vol. 7 (8), pp. 656–662, Apr. 2011.

[29] M. Krüger, M. Schenk, and P. Hommelhoff. "Attosecond control of electrons emitted from a nanoscale metal tip." *Nature*, vol. 475 (7354), pp. 78–81, July 2011.

[30] A. Wirth, R. Santra, and E. Goulielmakis. "Real time tracing of valence-shell electronic coherences with attosecond transient absorption spectroscopy." *Chemical Physics*, vol. 414, pp. 149–159, Mar. 2013.

[31] P. B. Corkum and F. Krausz. "Attosecond science." *Nature Physics*, vol. 3 (6), pp. 381–387, 2007.

[32] F. Krausz and M. Ivanov. "Attosecond physics." *Reviews of Modern Physics*, vol. 81 (1), pp. 163–234, Feb. 2009.

[33] M. Chini, K. Zhao, and Z. Chang. "The generation, characterization and applications of broadband isolated attosecond pulses." *Nature Photonics*, vol. 8 (3), pp. 178–186, Feb. 2014.

[34] F. Krausz and M. I. Stockman. "Attosecond metrology: from electron capture to future signal processing." *Nature Photonics*, vol. 8 (3), pp. 205–213, Feb. 2014.

[35] P. Baum and A. H. Zewail. "4D attosecond imaging with free electrons: Diffraction methods and potential applications." *Chemical Physics*, vol. 366 (1-3), pp. 2–8, Dec. 2009.

[36] A. H. Zewail. "Four-dimensional electron microscopy." *Science*, vol. 328 (5975), pp. 187–193, 2010.

[37] X. Wang, S. Nie, H. Park, J. Li, R. Clinite, R. Li, X. Wang, and J. Cao. "Measurement of femtosecond electron pulse length and the temporal broadening due to space charge." *Review of Scientific Instruments*, vol. 80 (1), p. 013902, 2009.

[38] T. van Oudheusden, P. L. E. M. Pasmans, S. B. van der Geer, M. J. de Loos, M. J. van der Wiel, and O. J. Luiten. "Compression of Subrelativistic Space-Charge-Dominated Electron Bunches for Single-Shot Femtosecond Electron Diffraction." *Physical Review Letters*, vol. 105 (26), Dec. 2010.

[39] A. Gliserin, A. Apolonski, F. Krausz, and P. Baum. "Compression of single-electron pulses with a microwave cavity." *New Journal of Physics*, vol. 14 (7), p. 073055, July 2012.

[40] A. Gliserin. "Towards attosecond 4D imaging of atomic-scale dynamics by single-electron diffraction." PhD thesis. LMU, Feb. 2014.

[41] L. Wimmer, G. Herink, D. R. Solli, S. V. Yalunin, K. E. Echternkamp, and C. Ropers. "Terahertz control of nanotip photoemission." *Nature Physics*, vol. 10 (6), pp. 432–436, May 2014.

[42] J. Fabiańska, G. Kassier, and Th. Feurer. "Split ring resonator based THz-driven electron streak camera featuring femtosecond resolution." *Scientific Reports*, vol. 4, July 2014.

[43] B. J. Siwick, A. A. Green, C. T. Hebeisen, and R. J. Miller. "Characterization of ultrashort electron pulses by electron-laser pulse cross correlation." *Optics Letters*, vol. 30 (9), pp. 1057–1059, 2005.

[44] C. T. Hebeisen, R. Ernstorfer, M. Harb, T. Dartigalongue, R. E. Jordan, and R. J. D. Miller. "Femtosecond electron pulse characterization using laser ponderomotive scattering." *Optics Letters*, vol. 31 (23), pp. 3517–3519, 2006.

[45] C. T. Hebeisen, G. Sciaini, M. Harb, R. Ernstorfer, Th. Dartigalongue, S. G. Kruglik, and R. J. D. Miller. "Grating enhanced ponderomotive scattering for visualization and full characterization of femtosecond electron pulses." *Optics Express*, vol. 16 (5), pp. 3334–3341, 2008.

[46] M. Gao, H. Jean-Ruel, R. R. Cooney, J. Stampe, M. de Jong, M. Harb, G. Sciaini, G. Moriena, and R. J. D. Miller. "Full characterization of RF compressed femtosecond electron pulses using ponderomotive scattering." *Optics Express*, vol. 20 (11), pp. 12048–12058, 2012.

[47] F. O. Kirchner, A. Gliserin, F. Krausz, and P. Baum. "Laser streaking of free electrons at 25 keV." *Nature Photonics*, vol. 8 (1), pp. 52–57, Dec. 2013.

[48] B. Barwick, D. J. Flannigan, and A. H. Zewail. "Photon-induced near-field electron microscopy." *Nature*, vol. 462 (7275), pp. 902–906, Dec. 2009.

[49] S. T. Park, M. Lin, and A. H. Zewail. "Photon-induced near-field electron microscopy (PINEM): theoretical and experimental." *New Journal of Physics*, vol. 12 (12), p. 123028, Dec. 2010.

[50] D. Kreier. "Ultrafast single-electron diffraction at 100 keV and investigation of carbon-nanotube dynamics." PhD thesis. Ludwig Maximilians Universität München, 2015.

[51] W. Schneider, A. Ryabov, Cs. Lombosi, T. Metzger, Zs. Major, J. A. Fülöp, and P. Baum. "800-fs, 330-$\mu$J pulses from a 100-W regenerative Yb:YAG thin-disk amplifier at 300 kHz and THz generation in $LiNbO_3$." *Optics Letters*, vol. 39 (23), p. 6604, Dec. 2014.

[52] R. Graf, Th. Metzger, M. Chyla, D. Sutter, Z. Major, A. Apolonski, and F. Krausz. "High average power Yb:YAG thin disk regenerative amplifier at up to 1 MHz repetition rate." Sweden, 2012.

[53] H. Fattahi et al. "Third-generation femtosecond technology." *Optica*, vol. 1 (1), p. 45, July 2014.

[54] O. Pronin, J. Brons, C. Grasse, V. Pervak, G. Boehm, M.-C. Amann, V. L. Kalashnikov, A. Apolonski, and F. Krausz. "High-power 200 fs Kerr-lens mode-locked Yb:YAG thin-disk oscillator." *Optics Letters*, vol. 36 (24), pp. 4746–4748, 2011.

[55] C. J. Saraceno et al. "275 W average output power from a femtosecond thin disk oscillator operated in a vacuum environment." *Optics Express*, vol. 19 (21), pp. 20288–20300, 2011.

[56] T. Eidam, S. Hanf, E. Seise, Th. V. Andersen, Th. Gabler, C. Wirth, Th. Schreiber, J. Limpert, and A. Tünnermann. "Femtosecond fiber CPA system emitting 830 W average output power." *Optics Letters*, vol. 35 (2), pp. 94–96, 2010.

[57] A. Klenke, S. Breitkopf, M. Kienel, Th. Gottschall, T. Eidam, S. Hädrich, J. Rothhardt, J. Limpert, and A. Tünnermann. "530 W, 13 mJ, four-channel coherently combined femtosecond fiber chirped-pulse amplification system." *Optics Letters*, vol. 38 (13), p. 2283, July 2013.

[58] S. V. Marchese, C. R. Baer, A. G. Engqvist, S. Hashimoto, D. J. Maas, M. Golling, T. Südmeyer, and U. Keller. "Femtosecond thin disk laser oscillator with pulse energy beyond the 10-microjoule level." *Optics Express*, vol. 16 (9), pp. 6397–6407, 2008.

[59] D. Bauer, I. Zawischa, D. Sutter, A. Killi, and T. Dekorsy. "Mode-locked Yb:YAG thin-disk oscillator with 41 $\mu$J pulse energy at 145 W average infrared power and high power frequency conversion." *Applied Physics B*, vol. 106 (3), pp. 559–562, Mar. 2012.

[60] C. J. Saraceno, F. Emaury, C. Schriber, M. Hoffmann, M. Golling, Th. Südmeyer, and U. Keller. "Ultrafast thin-disk laser with 80 $\mu$J pulse energy and 242 W of average power." *Optics Letters*, vol. 39 (1), p. 9, Dec. 2013.

[61] P. Russbueldt, T. Mans, G. Rotarius, J. Weitenberg, H. D. Hoffmann, and R. Poprawe. "400W Yb:YAG Innoslab fs-amplifier." *Optics Express*, vol. 17 (15), pp. 12230–12245, 2009.

[62] P. Russbueldt, T. Mans, J. Weitenberg, H. D. Hoffmann, and R. Poprawe. "Compact diode-pumped 1.1 kW Yb:YAG Innoslab femtosecond amplifier." *Optics Letters*, vol. 35 (24), pp. 4169–4171, 2010.

[63] R. Fleischhaker, R. Gebs, A. Budnicki, M. Wolf, J. Kleinbauer, and D. Sutter. "Compact gigawatt-class sub-picosecond Yb:YAG thin-disk regenerative chirped-pulse amplifier with high average power at up to 800 kHz." Conference on Lasers and Electro-Optics Europe, 2013.

[64] C. Teisset, M. Schultze, R. Bessing, M. Haefner, S. Prinz, D. Sutter, and Th. Metzger. "300 W Picosecond Thin-Disk Regenerative Amplifier at 10 kHz Repetition Rate." *Mid-Infrared Coherent Sources*. Optical Society of America, 2013, JTh5A–1.

[65] K.-H. Hong et al. "High-energy, kHz-repetition-rate, ps cryogenic Yb:YAG chirped-pulse amplifier." *Optics Letters*, vol. 35 (11), pp. 1752–1754, 2010.

[66] M. Schulz et al. "Yb:YAG Innoslab amplifier: efficient high repetition rate subpicosecond pumping system for optical parametric chirped pulse amplification." *Optics Letters*, vol. 36 (13), pp. 2456–2458, 2011.

[67] S. Klingebiel, C. Wandt, C. Skrobol., I. Ahmad, S. A. Trushin, Z. Major, F. Krausz, and S. Karsch. "High energy picosecond Yb:YAG CPA system at 10 Hz repetition rate for pumping optical parametric amplifiers." *Optics Express*, vol. 19 (6), pp. 5357–5363, 2011.

[68] M. Schulz et al. "Pulsed operation of a high average power Yb:YAG thin-disk multipass amplifier." *Optics Express*, vol. 20 (5), pp. 5038–5043, 2012.

[69] J.-P. Negel, A. Voss, M. A. Ahmed, D. Bauer, D. Sutter, A. Killi, and Th. Graf. "1.1 kW average output power from a thin-disk multipass amplifier for ultrashort laser pulses." *Optics Letters*, vol. 38 (24), p. 5442, Dec. 2013.

[70] J. Tümmler, R. Jung, H. Stiel, P. V. Nickles, and W. Sandner. "High-repetition-rate chirped-pulse-amplification thin-disk laser system with joule-level pulse energy." *Optics Letters*, vol. 34 (9), pp. 1378–1380, 2009.

[71] S. Lahme, C. Kealhofer, F. Krausz, and P. Baum. "Femtosecond single-electron diffraction." *Structural Dynamics*, vol. 1 (3), p. 034303, May 2014.

[72] C. Homann, C. Schriever, P. Baum, and E. Riedle. "Octave wide tunable UV-pumped NOPA: pulses down to 20 fs at 0.5 MHz repetition rate." *Optics Express*, vol. 16 (8), pp. 5746–5756, 2008.

[73] M. Bradler, C. Homann, and E. Riedle. "Broadband difference frequency mixing between visible and near-infrared pulses for few-cycle pulse generation with stable carrier-envelope phase." *Applied Physics B*, vol. 113 (1), pp. 19–25, Oct. 2013.

[74] J. Hebling, K. L. Yeh, M. C. Hoffmann, and K. A. Nelson. "High-power THz generaton, THz nonlinear optics, and THz nonlinear spectroscopy." *IEEE Journal of Selected Topics In Quantum Electronics*, vol. 14, pp. 345–353, 2008.

[75] H. Hirori and K. Tanaka. "Nonlinear optical phenomena induced by intense single-cycle terahertz pulses." *IEEE Journal of Selected Topics In Quantum Electronics*, vol. 19 (8401110), 2013.

[76] W. Köchner. *Solid State Laser Engineerng*. 6th. Springer, 2006.

[77] R. A. Lewis. "A review of terahertz sources." *Journal of Physics D: Applied Physics*, vol. 47 (37), p. 374001, Sept. 2014.

[78] H. Ito. "Breakthroughs in Photonics 2013: Terahertz Wave Photonics." *IEEE Photonics Journal*, vol. 6 (2), pp. 1–5, Apr. 2014.

[79] D. M. Mittleman. "Frontiers in terahertz sources and plasmonics." *Nature Photonics*, vol. 7 (9), pp. 666–669, 2013.

[80] M. C. Hoffmann and J. A. Fülöp. "Intense ultrashort terahertz pulses: generation and applications." *Journal of Physics D: Applied Physics*, vol. 44 (8), p. 083001, Mar. 2011.

[81] M. Tonouchi. "Cutting-edge terahertz technology." *Nature Photonics*, vol. 1 (2), pp. 97–105, 2007.

[82] B. Ferguson and X.-C. Zhang. "Materials for terahertz science and technology." *Nature Materials*, vol. 1 (1), pp. 26–33, 2002.

[83] J. A. Fülöp, L. Pálfalvi, S. Klingebiel, G. Almási, F. Krausz, S. Karsch, and J. Hebling. "Generation of sub-mJ terahertz pulses by optical rectification." *Optics Letters*, vol. 37 (4), pp. 557–559, 2012.

[84] J. A. Fülöp, Z. Ollmann, Cs. Lombosi, C. Skrobol, S. Klingebiel, L. Pálfalvi, F. Krausz, S. Karsch, and J. Hebling. "Efficient generation of THz pulses with 0.4 mJ energy." *Optics Express*, vol. 22 (17), p. 20155, Aug. 2014.

[85] J. A. Fülöp, L. Pálfalvi, G. Almási, and J. Hebling. "Design of high-energy terahertz sources based on optical rectification." *Optics Express*, vol. 18 (12), pp. 12311–12327, 2010.

[86] J. Hebling, K. L. Yeh, M. C. Hoffmann, B. Bartal, and K. A. Nelson. "Generation of high-power terahertz pulses by tilted-pulse-front excitation and their application possibilities." *JOSA B*, vol. 25 (7), B6–B19, 2008.

[87] J. Hebling, A. G. Stepanov, G. Almasi, B. Bartal, and J. Kuhl. "Tunable THz pulse generation by optical rectification of ultrashort laser pulses with tilted pulse fronts." *Applied Physics B: Lasers and Optics*, vol. 78 (5), pp. 593–599, Mar. 2004.

[88] M. C. Hoffmann, K.-L. Yeh, J. Hebling, and K. A. Nelson. "Efficient terahertz generation by optical rectification at 1035 nm." *Optics Express*, vol. 15 (18), pp. 11706–11713, 2007.

[89] G. G. Gurzadyan, V. G. Dmitriev, and D. N. Nikogosyan. *Handbook of nonlinear optical crystals*. eng. 3rd, rev. ed. Springer series in optical sciences v. 64. Berlin ; New York: Springer, 1999.

[90] L. Pálfalvi, J. Hebling, J. Kuhl, Á. Péter, and K. Polgár. "Temperature dependence of the absorption and refraction of Mg-doped congruent and stoichiometric $LiNbO_3$ in the THz range." *Journal of Applied Physics*, vol. 97 (12), p. 123505, 2005.

[91] J. Hebling, G. Almasi, I. Z. Kozma, J. Kuhl, et al. "Velocity matching by pulse front tilting for large area THz-pulse generation." *Opt. Express*, vol. 10 (21), pp. 1161–1166, 2002.

[92] M. I. Bakunov, S. B. Bodrov, and M. V. Tsarev. "Terahertz emission from a laser pulse with tilted front: Phase-matching versus Cherenkov effect." *Journal of Applied Physics*, vol. 104 (7), p. 073105, 2008.

[93] M. I. Bakunov, S. B. Bodrov, and E. A. Mashkovich. "Terahertz generation with tilted-front laser pulses: dynamic theory for low-absorbing crystals." *JOSA B*, vol. 28 (7), pp. 1724–1734, 2011.

[94] D. Kreier and P. Baum. "Avoiding temporal distortions in tilted pulses." *Optics Letters*, vol. 37 (12), pp. 2373–2375, 2012.

[95] A. Tomasino, A. Parisi, S. Stivala, P. Livreri, A. C. Cino, A. C. Busacca, M. Peccianti, and R. Morandotti. "Wideband THz Time Domain Spectroscopy based on Optical Rectification and Electro-Optic Sampling." *Scientific Reports*, vol. 3, Oct. 2013.

[96] T. Kampfrath, J. Nötzold, and M. Wolf. "Sampling of broadband terahertz pulses with thick electro-optic crystals." *Applied Physics Letters*, vol. 90 (23), p. 231113, 2007.

[97] X.-C. Zhang and J. Xu. *Introduction to THz Wave Photonics*. en. Boston, MA: Springer US, 2010.

[98] S.-W. Huang, E. Granados, W. R. Huang, K.-H. Hong, L. E. Zapata, and F. X. Kärtner. "High conversion efficiency, high energy terahertz pulses by optical rectification in cryogenically cooled lithium niobate." *Optics Letters*, vol. 38 (5), pp. 796–798, 2013.

[99] J. A. Fülöp, L. Pálfalvi, M. C. Hoffmann, and J. Hebling. "Towards generation of mJ-level ultrashort THz pulses by optical rectification." *Optics Express*, vol. 19 (16), pp. 15090–15097, 2011.

[100] L. Pálfalvi, J. A. Fülöp, G. Almási, and J. Hebling. "Novel setups for extremely high power single-cycle terahertz pulse generation by optical rectification." *Applied Physics Letters*, vol. 92 (17), p. 171107, 2008.

[101] M. Kunitski et al. "Optimization of single-cycle terahertz generation in $LiNbO_3$ for sub-50 femtosecond pump pulses." *Optics Express*, vol. 21 (6), pp. 6826–6836, 2013.

[102] D. J. Bradley, B. Liddy, and W. E. Sleat. "Direct linear measurement of ultrashort light pulses with a picosecond streak camera." *Optics Communications*, vol. 2 (8), pp. 391–395, 1971.

[103] M. Y. Schelev, M. C. Richardson, and A. J. Alcock. "Image-converter streak camera with picosecond resolution." *Applied Physics Letters*, vol. 18 (8), pp. 354–357, 1971.

[104] J. Itatani, F. Quéré, G. Yudin, M. Ivanov, F. Krausz, and P. Corkum. "Attosecond Streak Camera." *Physical Review Letters*, vol. 88 (17), Apr. 2002.

[105] R. Kienberger. "Atomic transient recorder." *Nature*, vol. 427 (6977), pp. 817–821, Feb. 2004.

[106] M. Drescher, M. Hentschel, R. Kienberger, G. Tempea, C. Spielmann, G. A. Reider, P. B. Corkum, and F. Krausz. "X-ray pulses approaching the attosecond frontier." *Science*, vol. 291 (5510), pp. 1923–1927, 2001.

[107] M. Hentschel et al. "Attosecond metrology." *Nature*, vol. 414 (6863), pp. 509–513, 2001.

[108] E. Goulielmakis et al. "Direct measurement of light waves." *Science*, vol. 305 (5688), pp. 1267–1269, 2004.

[109] U. Frühling et al. "Single-shot terahertz-field-driven X-ray streak camera." *Nature Photonics*, vol. 3 (9), pp. 523–528, Aug. 2009.

[110] M. Born and E. Wolf. *Principles of optics*. 7th. Cambridge University Press, 1999.

[111] F. Kirchner. "Ultrashort and coherent single-electron pulses for diffraction at ultimate resolutions." PhD thesis. LMU, Sept. 2013.

[112] H.-J. Hagemann, W. Gudat, and C. Kunz. *Optical constants from the far infrared to the x-ray region: Mg, Al, Cu, Ag, Au, Bi, C, and $Al_2O_3$*. Tech. rep. DESY SR-74/7. DESY, May 1974.

[113] H.-J. Hagemann, W. Gudat, and C. Kunz. "Optical constants from the far infrared to the x-ray region: Mg, Al, Cu, Ag, Au, Bi, C, and $Al_2O_3$." *JOSA*, vol. 65 (6), pp. 742–744, 1975.

[114] W. Demtröder. *Experimentalphysik 2*. Berlin: Springer Verlag, 2013.

[115] A. Yariv. *Quantum Electronics*. 3rd. John Wiley & Sons, 1989.

[116] M. M. Shakya and Z. Chang. "Achieving 280 fs resolution with a streak camera by reducing the deflection dispersion." *Applied Physics Letters*, vol. 87 (4), p. 041103, 2005.

[117] L. Kasmi, D. Kreier, M. Bradler, E. Riedle, and P. Baum. "Femtosecond single-electron pulses generated by two-photon photoemission close to the work function." *New Journal of Physics*, vol. 17 (3), p. 033008, Mar. 2015.

[118] G. H. Kassier, K. Haupt, N. Erasmus, E. G. Rohwer, H. M. von Bergmann, H. Schwoerer, S. M. M. Coelho, and F. D. Auret. "A compact streak camera for 150 fs time resolved measurement of bright pulses in ultrafast electron diffraction." *Review of Scientific Instruments*, vol. 81 (10), p. 105103, 2010.

[119] M. Shalaby and C. P. Hauri. "Demonstration of a low-frequency three-dimensional terahertz bullet with extreme brightness." *Nature Communications*, vol. 6, p. 5976, Jan. 2015.

[120] M. Aidelsburger, F. O. Kirchner, F. Krausz, and P. Baum. "Single-electron pulses for ultrafast diffraction." *Proceedings of the National Academy of Sciences*, vol. 107 (46), pp. 19714–19719, Nov. 2010.

# Acknowledgements

At this point I would like to thank all the people who made this work possible with their numerous and manifold contributions.

First of all, I'm very grateful to Prof. Ferenc Krausz for my admission in his interdisciplinary working research group of international reputation. The given chance to work with so many excellent scientists in an international atmosphere was an unique opportunity which cannot be overestimated. In the past I've enormously profited from the remarkable base of knowledge provided by Prof. Krausz and his team. I also would like to thank Prof. Roland Kersting for kindly offering to review my thesis.

I cordially thank Peter Baum, my supervisor and leader of the ultrafast electron diffraction group, for almost three and a half years of continuously targeted and pleasant collaboration. During many discussions in this time I received valuable advice and could benefit from his broad scientific knowledge. I also thank him for thorough proof-reading of this manuscript and his precious suggestions for improvements.

I'm grateful to the other members of the ultrafast electron diffraction group as well. Especially, I would like to thank Andrey Ryabov for his reliable and unlimited support in the laboratory. Many thanks go also to both Andrey and Peter for providing the code which was used to simulate the deflectograms. I thank Daniel Kreier for the development of the electron source and the design of the vacuum system and Roswitha Graf for her valuable help during the installation of the laser system and her short but extensive introduction into the technology of regenerative laser amplifiers. I'm also grateful to Catherine Kealhofer and Dominik Ehberger for valuable discussions about the electron deflection experiment. Many thanks go to Alexander Gliserin for his competent advice in arising LaTeX issues.

I thank József Fülöp for helpful conversations about the THz setup.

Many thanks to Dagmar Frischke for preparing thin free standing metal films as well as to Rolf Oehm and his team for competent realization of custom parts and especially for numerous infrastructure installations in the laboratory.

I thank all mentioned and unmentioned colleagues for a pleasant working atmosphere, especially my office mates Florian Habel, Matthias Kübel and Ernst Fill. In particular I would like to thank Olga Razskazovskaya, Kellie Pearce, Elena Fedulova and Matthew Walbran for organizing entertaining social events aside from the laboratory as well as Oleg Pronin and Vladimir Pervak for numerous mountain excursions.

Last but not least, I'm grateful to my parents and the family Dankesreiter for their continuous understanding of my frequent absence in their lives over the past years.